Universitat de València
DEPARTAMENT DE FÍSICA ATÒMICA
MOLECULAR I NUCLEAR

Development of Stripline Kickers for Low Emittance Rings: Application to the Beam Extraction Kicker for CLIC Damping Rings

TESI DOCTORAL EN FÍSICA

Carolina Belver Aguilar

Abril de 2015

Supervisors:

Ángeles Faus-Golfe
Fernando Toral Fernández

Dra. ÁNGELES FAUS GOLFE, Científic Titular del Consejo Superior de Investigaciones Científicas (CSIC),
Dr. FERNANDO TORAL FERNÁNDEZ, Responsable de la Unidad de Aceleradores del Centro de Investigaciones Energéticas, Medioambientales y Tecnológicas (CIEMAT),

CERTIFIQUEM:

Que la present memòria *Development of Stripline Kickers for Low Emittance Rings: Application to the Beam Extraction Kicker for CLIC Damping Rings* ha estat realitzada baix la nostra direcció en el Departament de Física Atòmica Molecular i Nuclear de la Universitat de València per Carolina Belver Aguilar i constitueix la seua Tesi Doctoral.

I per a que així conste, firmem el present Certificat.

Firmat: Ángeles Faus Golfe

Firmat: Fernando Toral Fernández

A la memoria de
Montserrat Garrigós Jordana

Resumen

El descubrimiento del bosón de Higgs ha iniciado una nueva era en el LHC cuyo objetivo será medir las propiedades de dicho bosón con la mayor precisión posible. Sin embargo, dada la complejidad de los protones, compuestos por quarks y gluones, existe el consenso en la Física de Altas Energías de que el próximo colisionador será un colisionador electrón-positrón. Desde un punto de vista simplista, para que electrones y positrones colisionen a muy altas energías en un colisionador circular, la energía perdida por radiación sincrotrón debe reponerse mediante estructuras aceleradoras de radiofrecuencia. Una alternativa para evitar este problema, es construir un colisionador lineal donde dos aceleradores lineales (linacs) opuestos aceleran las partículas hasta alcanzar su energía final en un solo paso antes de hacerlas colisionar en un punto de interacción central. Dos colisionadores lineales de electrones y positrones han sido propuestos: ILC (International Linear Collider) en el rango de energías de 1 TeV, y CLIC (Compact Linear Collider) en el rango de energías de 10 TeV. ILC ha sido diseñado para operar a una energía de 0.5 TeV y con una luminosidad de $2\times10^{34}\text{cm}^{-2}\text{s}^{-1}$, utilizando cavidades aceleradoras superconductoras con un gradiente de aceleración de 31.5 MV/m. En cambio, CLIC está siendo diseñado para tener una energía de 3 TeV, y una luminosidad máxima de $10^{35}\text{cm}^{-2}\text{s}^{-1}$, con un gradiente de aceleración de 100 MV/m.

Para alcanzar dichas luminosidades se necesitan anillos de amortiguamiento (Damping Rings, DRs) que reduzcan la emitancia de los haces creados por las fuentes de electrones y positrones varios órdenes de magnitud, produciendo además haces muy estables. El diseño de los DRs es diferente en el caso de ILC y CLIC. En CLIC, el tren de paquetes de partículas es relativamente corto con muy poco espacio entre paquetes y una alta frecuencia de repetición, mientras que el tren de paquetes de ILC es más largo, lo que hace que los DRs deban tener un radio mayor. Además, la alta luminosidad necesaria en ILC se consigue aumentando la carga del paquete de partículas, mientras que en CLIC se consigue reduciendo la emitancia del haz hasta valores sin precedentes, especialmente en el plano vertical: 5 nm en el caso de CLIC a una energía de 2.86 GeV, mientras que para ILC es 20 nm a una energía de 5 GeV. Esta emitancia vertical en CLIC se podría conseguir mediante dos pre-damping rings (PDRs) y dos DRs. Para transferir el haz de un anillo a otro, así como desde la fuente de electrones y positrones a los PDRs y desde los DRs a los linacs, se necesita un sistema de inyección y un sistema de extracción del haz en cada uno de los cuatro anillos. Estos sistemas

de inyección o extracción (kickers) deben inyectar o extraer el haz de manera muy estable y afectar mínimamente al haz que circula. Estudios anteriores de los kickers de inyección y extracción para el desarrollo del ILC y del CLIC Test Facility 3 (CTF3), demostraron que el kicker electromagnético, conocido como stripline kicker, es el más adecuado para este tipo de operación.

Este proyecto de tesis doctoral tiene como objetivo el desarrollo de la metodología necesaria para diseñar stripline kickers para aceleradores circulares de baja emitancia. En particular esta tesis se basa en el diseño, construcción y tests de laboratorio del stripline kicker para la extracción de haz de los DRs de CLIC, pero los estudios realizados pueden extenderse a los DRs de ILC o a cualquier otro anillo de baja emitancia.

La primera parte de este trabajo de investigación se centra en el estudio y diseño del stripline kicker, consistente en dos electrodos dentro de un tubo cilíndrico de vacío. Con el fin de conseguir las especificaciones requeridas, para el diseño de este prototipo la autora propone un nuevo enfoque que no había sido utilizado hasta ahora en el estudio de Futuros Colisionadores Lineales (FLCs). Éste consiste en el estudio de los dos modos de operación que presentan dos líneas de transmisión acopladas, como es el caso del stripline kicker, analizando cómo varían diferentes parámetros en ambos modos de operación con la geometría de los electrodos, para las dos geometrías más ampliamentes usadas, electrodos planos y electrodos curvos. Estos primeros estudios se han realizado analíticamente y numéricamente usando el código de simulación de campos electromagnéticos en el dominio de la frecuencia HFSS. Estos estudios han sido: impedancia característica de las líneas de transmisión acopladas y homogeneidad del campo electromagnético. De este estudio se concluyó que sólo con los electrodos planos se cumplen las especificaciones de homogeneidad de campo, mientras que la adaptación de impedancias en ambos modos de operación no fueron del todo óptimas. Por este motivo, la autora ha propuesto una nueva geometría, llamada media luna, con la que se mejoró la adaptación de impedancias. Estas dos geometrías, electrodos planos y electrodos media luna, se estudiaron más en profundidad y se confrontaron los resultados para elegir la geometría más óptima. Los estudios realizados fueron los siguientes: la aparición de arcos eléctricos (rigidez dieléctrica) entre los electrodos y el tubo de vacío, la transmisión de potencia a través de los electrodos y la impedancia longitudinal y transversal que ve el haz de partículas al pasar a través del stripline kicker. Estos últimos estudios se realizaron con el programa de simulación de campos electromagnéticos en el dominio del tiempo CST, que permite simular el paso de un haz a través de una estructura. Al final de este estudio, se eligieron los electrodos media luna como la geometría más óptima para el kicker de extracción del haz de los DRs de CLIC.

La segunda parte de este trabajo de tesis consiste en el estudio del resto de componentes, aparte de los electrodos y la cámara de vacío, que conforman un stripline kicker: los soportes de los electrodos y los pasamuros, así como los materiales y el estudio de las tolerancias. Los soportes convencionales no se han utilizado, y un nuevo diseño, consistente en cuatro anillos cerámicos, ha sido propuesto. Estos soportes permiten el ensamblaje de los electrodos fuera de la cámara de vacío, lo que asegura su

paralelismo y posición angular antes de introducirlos en la cámara: ésta es la única manera de garantizar la uniformidad de campo. Además, debido al poco espacio entre los electrodos y la cámara de vacío los soportes convencionales no hubiesen podido utilizarse. El programa de simulación CST se ha utilizado para estudiar cómo estos anillos cerámicos, así como los pasamuros comerciales escogidos, afectan a la transmisión de potencia y a la impedancia de acoplamiento del haz.

La tercera parte de la tesis comprende las medidas en laboratorio que han permitido corroborar los estudios analíticos y numéricos realizados previamente a bajas frecuencias. Las medidas realizadas han sido: parámetros de reflexión, impedancia longitudinal del haz, impedancia transversal del haz y fenómenos de arcos eléctricos para alto voltaje. Los resultados para los parámetros de reflexión y para la impedancia longitudinal del haz están de acuerdo con las simulaciones realizadas en la fase del diseño, mientras que para la impedancia transversal, sobre todo en el caso vertical, se necesitarán más estudios. Por otro lado, la aparición de arcos eléctricos a voltajes de unos ±10 kV en DC, hace que sean necesarias medidas con voltajes pulsados para garantizar la correcta operación del kicker una vez instalado en un acelerador. Gracias al profundo conocimiento adquirido durante todo este trabajo, también se presentan diferentes propuestas para kickers de nueva generación.

Para finalizar la caracterización de este primer prototipo, en el futuro se realizarán medidas con haz en un acelerador, que ayudarán a estudiar la impedancia longitudinal y transversal del haz, tanto a bajas como a altas frecuencias.

La construcción de sistemas de inyección y extracción más estables y con baja impedancia de haz, permitirá que haces de muy baja emitancia sean inyectados en los FLCs, aumentando así la probabilidad de colisión en el punto de interacción. Además, todos estos desarrollos serán de gran utilidad en otros aceleradores como por ejemplo futuras fuentes de luz sincrotrón y los Futuros Colisionadores Circulares (FCCs).

Abstract

In the framework of the design study of Future Linear Colliders, the Compact Linear Collider (CLIC) aims for electron-positron collisions with high luminosity at a nominal centre-of-mass energy of 3 TeV. To achieve the luminosity requirements, Pre-Damping Rings (PDRs) and Damping Rings (DRs) are required: they reduce the beam emittance before the beam is accelerated in the main linac. Several injection and extraction systems are needed to inject and extract the beam from the PDRs and DRs. The work of this Thesis consists of the design, fabrication and laboratory tests of the first stripline kicker prototype for beam extraction from the CLIC DRs, although the methodology proposed can be extended to stripline kickers for any low emittance ring. The excellent field homogeneity required, as well as a good transmission of the high voltage pulse through the electrodes, has been achieved by choosing a novel electrode shape. With this new geometry, it has been possible to benefit from all the advantages that the most common shapes introduce separately. Furthermore, a detailed study of the different operating modes of a stripline kicker allowed the beam coupling impedance to be fully characterized at low frequencies. The optimum design of the striplines and their components has been based on studies of impedance matching, field homogeneity, power transmission, beam coupling impedance and manufacturing tolerances. Other studies concerning higher order modes and electrodes heating have been done. The striplines have been manufactured by the spanish company Trinos Vacuum Projects, and laboratory tests without beam have been carried out in order to characterize the striplines. The following tests have been done: power reflection, longitudinal and transverse beam coupling impedance and RF breakdown. Finally, new ideas for further improvement of the performance of future striplines are reported.

Contents

Chapter 1

Introduction

Particle Physics field has made impressive progress in the pursuit of its core mission, elucidating the laws of nature at the most fundamental level. A giant leap, the discovery of the Higgs boson, has been accompanied by many experimental results confirming the Standard Model beyond the previously explored energy scales. These results raise further questions on the origin of elementary particle masses and on the role of the Higgs boson in the more fundamental theory underlying the Standard Model, which may involve additional particles to be discovered around the TeV scale.

The discovery of the Higgs boson, announced in July 2012, is the start of a major programme of work to measure particle's properties with the highest possible precision for testing the validity of the Standard Model and to search for further new physics at the energy frontier. The Large Hadron Collider (LHC), the highest energy hadron accelerator ever built, is in a unique position to pursue these objectives, and its full exploitation is one of the highest priorities in Particle Physics. The LHC was built in the existing 27 km circumference of the Large Electron Positron (LEP) tunnel, and first operated in 2008. In 2012, the LHC achieved a center-of-mass energy of 8 TeV and a peak luminosity of $7.7\times10^{33}\text{cm}^{-2}\text{s}^{-1}$. In 2015, after a long shutdown, it is planned that the LHC run at a center-of-mass energy of 13-14 TeV and its design peak luminosity of $10^{34}\text{cm}^{-2}\text{s}^{-1}$. To extend its discovery potential, the LHC will need a major upgrade, the High Luminosity LHC (HL-LHC), to increase its luminosity by a factor of ten beyond its design value [1].

Due to the large background present at hadron collisions, which impairs the detection of numerous events, a consensus has been reached in the particle physics community, supported by the International Committe for Future Accelerators (ICFA), that the results of the LHC will need to be complemented by experiments at a lepton collider in the TeV energy range.

Historically the last discoveries made by an hadron collider have been followed by accurate measurements with a light lepton collider. In fact after the $W^{\pm}$and Z^0 bosons discovery in the Super Proton Synchrotron (SPS) the LEP was used to make precise measurements of their properties. Protons are composed by quarks and gluons, then the center-of-mass energy of the single elementary particle involved in the collision

in the LHC cannot be precisely determined. The absence of precise knowledge of the collision's initial conditions makes the analysis of the data very challenging. By contrast, electrons and positrons are elementary, so e^+e^- colliders can be used to determine parameters with a much higher precision than proton ones, with very well defined initial states and lower background in the detectors because of the fact that no strong interactions are present but only electroweak.

In a simplistic point of view, the technical problem of colliding electrons against positrons at very high energies in a ring is the loss of energy due to synchrotron radiation (SR). It is well known that a charged particle emits radiation when it is accelerated. This radiation can be negligible when it comes from longitudinal acceleration, but when the trajectory is bent the energy loss per revolution comes to be:

$$\Delta E \approx \frac{\beta^3\gamma^4}{\rho^2} \approx \frac{E^4}{\rho^2 m^4} \tag{1.1}$$

where β is the particle's relative velocity, γ is the relativistic factor, ρ is the bending radius, E is the particle's energy and m is the particle's mass. Eq. (1.1) shows that the energy loss per revolution depends on the inverse of the fourth power of the particle mass. It is therefore much more higher for light electrons than for protons or heavy particles. This lost energy per SR has to be restored by the RF accelerating structures in order to be able to have the beam circulating and this turns to be one of the major restrictions to the circular e^+e^- collider. The highest energy lepton collisions so far, 209 GeV, have been achieved with e^+e^- colliding beams in the LEP at CERN. At this energy, the SR losses were already significant, amounting to 3% of the beam energy for a 27 km-long circumference, compensable by a powerful superconducting radio-frequency (SCRF) system providing up to 3640 MV per turn.

An alternative in order to build a Terascale lepton collider would be to avoid the bending of particle trajectories by using e^+e^- linear colliders where two opposing linear accelerators (linacs) accelerate the particles to their final energy in one pass before focusing and colliding them in a central Interaction Point (IP). There is a strong scientific case for a e^+e^- linear collider, complementary to the LHC, that can study the properties of the Higgs boson and other particles with unprecedented precision and whose energy can be upgraded. The Technical Design Report (TDR) [2] of the International Linear Collider (ILC) has been completed, with large European participation. The initiative from the Japanese particle physics community to host the ILC in Japan is most welcome, and European groups are eager to participate. Europe looks forward to a proposal from Japan to discuss a possible participation [3].

1.1 The Future Linear Colliders

There are two figures of merit for a collider: the centre-of-mass energy and the luminosity. The instantenous luminosity, at the Interaction Point (IP) is defined as:

$$\mathcal{L} = \frac{n_b N^2 f_{rep}}{4\pi\sigma_x\sigma_y}\mathcal{H}_D \tag{1.2}$$

where n_b is the number of bunches in a bunch train, N is the number of particles in a single bunch, f_{rep} is the machine pulse repetition rate, σ_x and σ_y are the RMS horizontal and vertical beam sizes at the IP, and $\mathcal{H}_D$ is the luminosity enhancement factor. The luminosity enhancement factor is defined as the ratio of the effective luminosity, resulting from the beam-beam interaction, to the geometrical luminosity. This factor is not calculable analytically, because the dynamics of the beam-beam interaction is non-linear. It is however a function of the so-called disruption parameter:

$$D_{x,y} \equiv \frac{\sigma_z}{f_{x,y}} = \frac{2r_e N\sigma_z}{\gamma\sigma_{x,y}(\sigma_x + \sigma_y)} \tag{1.3}$$

where σ_z is the RMS bunch length, r_e is the classical electron radius, and $f_{x,y}$ is the effective focal length of the beam in the transverse coordinates, as the mutual beam-beam focusing can be assimilated to a very thin quadrupole. This parameter quantifies the beam-beam effects and represents the relative change in the impact parameter while crossing the opposite bunch.

In a circular collider a large luminosity can be easily obtained because of the high collision rate (f_{rep}) achieved after many cycles. The linear collider is a single-pass machine where the electron and positron bunches are accelerated and collided only once and therefore the collision rate is lower than for circular colliders. Having a large number of bunches per train partially compensates this loss; however, if one wants to have comparable luminosities to the rings it is then necessary to reduce drastically the transverse beam sizes at the IP. The required tiny beam sizes demand for a very strong focusing quadrupoles close to the IP, and lead to strong beam-beam effects. In addition, tight tolerances on the vibration of the accelerator components are needed.

The luminosity can also be expressed in terms of the fundamental linear collider parameters which enter into the luminosity scaling:

$$\mathcal{L} \propto \frac{\eta P_{beam}}{E_{cm}}\sqrt{\frac{\delta_{BS}}{\gamma\epsilon_y}\mathcal{H}_D} \tag{1.4}$$

where η is the RF to beam power conversion efficiency, P_{beam} is the average beam power, E_{cm} is the center-of-mass energy, δ_{BS} is the beamstrahlung energy loss, and $\gamma\epsilon_y$ is the normalized vertical emittance.

From Eq. (1.4), it is shown that a higher luminosity can always be achieved by increasing the beam power. However, higher beam powers are generally constrained by both the available electrical power and the need to deal with the high beam powers within the machine. In addition, this power has to be supplied continuosly in order to accelerate each bunch train. The RF power required is generally much higher than the beam power due to the low beam power conversion efficiency η, which is typically in the range of 6-24%, depending on the choice of linac technology [4]. In addition

to the high beam power and the high RF to beam power transfer efficiency, a small normalized vertical emittance is required. Furthermore, a small bunch length is better to achieve high luminosity, although a shorter bunch length is generally accompanied by higher beamstrahlung energy loss.

The principle of a linear accelerator based on alternating fields was proposed by Ising and Wideroe in the first quarter of the last century. In this method, particles are accelerated by repeated application of RF fields [5]. Nowadays we use accelerating structures composed of a set of discs located normal to the axis of a waveguide tube, with an iris in the center to let the beam pass through. The size and shape of these RF cavities are carefully chosen, so that electromagnetic waves become resonant and build up inside the cavity. Charged particles passing through the cavity feel the overall force and direction of the resulting electromagnetic field, which transfers energy to push them forwards along the accelerator.

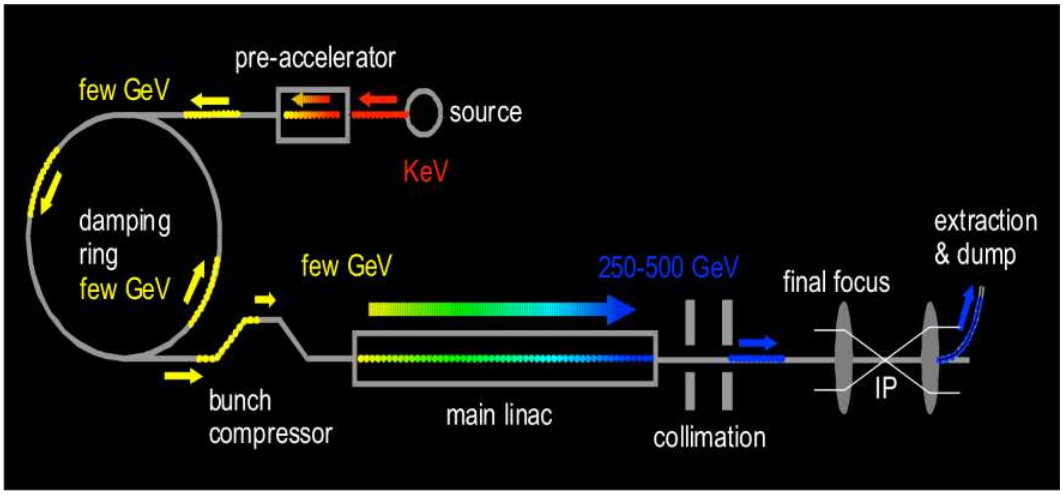

Figure 1.1: General layout of a “half” linear collider [4].

The general layout of a “half” linear collider is shown in Figure 1.1. The first part of the collider is the generation and injection system. The electrons are created in thermionic guns while the positrons are generated through pair production. After being accelerated and bunched, the low energy and high emittance beam is injected into the Damping Ring (DR), where the beam emittance is drastically reduced. The minimum emittance achievable in the DR is a crucial parameter because it is a lower limit for the rest of the collider and specially for the emittance at the IP. After the DR the beam naturally comes out extremely flat, this is an advantage for luminosity enhancement, as shown in Eq. (1.2). Once the emittance has been reduced in the DR, the bunch length is shortened in a bunch compresor. Then, the beam is injected into the main linac to be accelerated, using RF cavities, to the nominal energy prior to the collision. Apart from the RF cavities the linac has FODO cells, i.e. an arrangement of focusing and defocusing quadrupoles with the net effect of focusing the beam, dipole correctors and Beam Position Monitors (BPMs). This is the longest part of the accelerator. After the

acceleration of the beam comes the so-called Beam Delivery System (BDS). The BDS has the role of delivering the beam to the IP with the best quality. It is composed of a collimation section where the particles with position or energy out of a certain limits are eliminated in order to protect the Final Focus (FF) quadrupoles and reduce the background in the detector, and a chromatic correction section composed of sextupoles with the scope of correcting the aberrations introduced by the FF System (FFS), which is a set of very strong quadrupoles in different configurations that focus the beam to the smallest size in the IP. After that, the detectors will reconstruct and measure all the parameters in the collision event and the beam will be dumped.

During the last twenty years, dedicated and successful work by research groups worldwide has demonstrated that a linear collider can be built and reliably operated. Two e^+e^- linear collider projects have been proposed: the ILC in the range of 1 TeV, and the Compact Linear Collider (CLIC) in the range of 10 TeV. In June 2012, ICFA took the decision that the two projects start to work together under a unique Linear Collider effort collaborating on the technical issues that are common to both. L. Evans has been appointed as the new Linear Collider Collaboration (LCC) Director. The new leadership role unifies the two efforts, providing direction for R&D on both accelerator technologies. The LCC has three main sections, reflecting the three areas of research that will continue to be conducted: the ILC and CLIC accelerator, physics, and detectors sections, each of them with its associated director.

1.1.1 The International Linear Collider

The ILC is a linear e^+e^- collider with a centre-of-mass energy of 500 GeV and a luminosity of $2{\times}10^{34}\text{cm}^{-2}\text{s}^{-1}$, based on 1.3 GHz SCRF accelerating cavities with an accelerating gradient of 31.5 MV/m. The use of SCRF technology was recommended by the International Technology Recommendation Panel (ITRP) in August 2004, and shortly thereafter endorsed by the ICFA.

In an unprecedented milestone in high energy physics, the many institutes around the world involved in linear collider R&D join in a common effort to produce a global design for the ILC. As a result the ILC Global Design Effort (GDE) was formed. The first major goal of the GDE was to define the basic parameters and layout of the machine. During nearly a year the Baseline Configuration Document (BCD) was used as the basis for the detailed design work and cost estimate culminating in the completion of the second major milestone, the publication of the ILC Reference Design Report (RDR) [6]. With the completion of the RDR the GDE started an engineering design study, closely coupled with a prioritized R&D program. The goal was to produce the TDR [2], which was published in June 2013, presenting the matured technology design and construction plan for the ILC.

The ILC will extend approximately 31 km in length. The current baseline design, shown schematically in Fig. 1.2, allows for an upgrade to 50 kilometres, 1 TeV machine during the second stage of the project. There are also plans for an approach starting with a 250 GeV Higgs factory to study the properties of the particle discovered

at the LHC and then upgrading to 500 GeV.

The electron beam generation is made by means of a thermionic gun while the production of positrons is made by an undulator parallel to the electron linac. The electron beam is injected into the DR with a normalized vertical emittance of 45 μm. In the case of the positron beam, the injected normalized vertical emittance is 10 mm. These emittances are reduced in the DRs to 20 nm, by using wiggler magnets and RF cavities in their straight sections. After that and before the entrance of the main linac a bunch compressor reduces the bunch length from 6 mm to 300 μm in order to fulfill the linac requirements. The main linacs accelerate the bunches from 15 GeV to 250 GeV by means of SCRF units. Each SCRF unit has also a quadrupole to create a FODO lattice, a BPM and a superconducting horizontal and vertical corrector magnet in order to control the trajectory and preserve the emittance. The BDS is in charge of collimation and aberration corrections and focus the beam at the IP, in order to have a RMS beam size of 474 nm and 5.9 nm in the horizontal and the vertical plane, respectively. The beams collide with a 14 mrad angle: this angle prevents the interaction with new bunches and makes easier to eliminate the used beam. The beam is kicked by the so-called crab cavities in order to counter-cancel this angle to maximize the luminosity by making the bunches interact with no collision angle. Two detectors with a complex push-pull system are planned.

Parameter	**Value**	**[Unit]**
Luminosity, $\mathcal{L}$	1.8×10^{34}	[$cm^{-2}s^{-1}$]
Total length, L	31	[km]
Accelerating gradient, G	31.5	[MV/m]
Linac RF frequency, f_{RF}	1.3	[GHz]
Number of bunches, n_b	1312	
Bunch population, N	2.0×10^{10}	
Bunch separation, Δt_b	554	[ns]
RMS bunch length, σ_z	0.3	[mm]
Repetition rate, f_{rep}	5	[Hz]
Normalized horizontal emittance, $\gamma\epsilon_x$	10	[μm]
Normalized vertical emittance, $\gamma\epsilon_y$	35	[nm]
RMS horizontal beam size at IP, σ_x^*	474	[nm]
RMS vertical beam size at IP, σ_y^*	5.9	[nm]

Table 1.1: Summary table of the ILC parameters for the 500 GeV baseline [2].

Each one of these parts has technical challenges associated with the very tight requirements and constraints, which are summarized in Table 1.1. The main challenges are related to achieving the very high gradients in the main linacs and the small beam sizes in the IP, to provide the high luminosity required.

To demonstrate the industrialization of the SCRF technology and its application in a linac, the European X-Ray Free Electron Laser (XFEL) Project is under construction

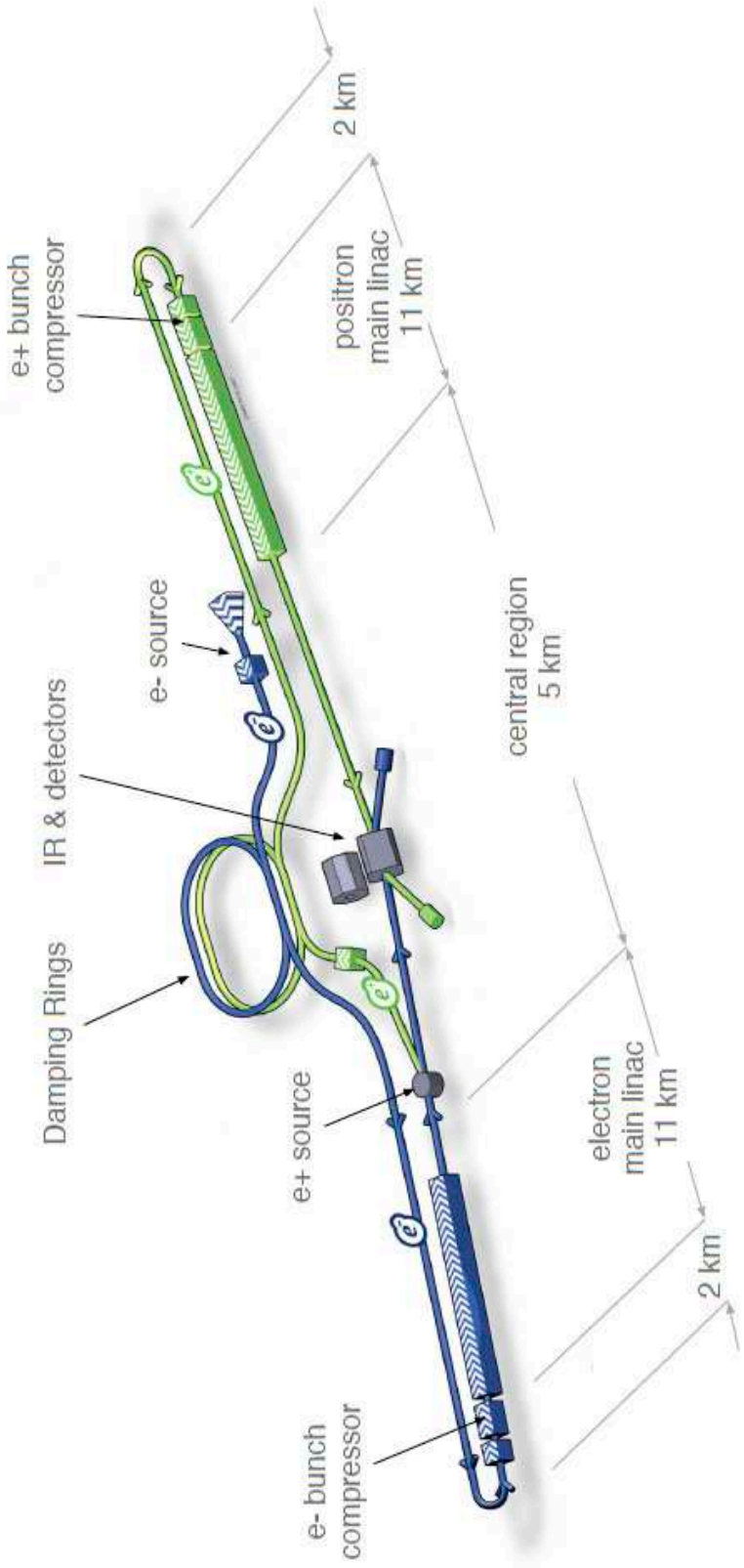

Figure 1.2: Schematic layout of the ILC [2].

in the Deutsches Elektronen-Synchrotron (DESY) since 2007 and has to be finished in 2015. In this complex the pilot facility, the Free-Electron Laser (FLASH), it is possible to run close to reference design gradients with nominal ILC beams. The primary goals of the 9 mA beam loading experiment are the demonstration of the bunch-to-bunch energy uniformity and stability, the characterization of the limits at high-gradient, and the quantification of the klystron power overhead required for low level RF control and measurement of the cryogenics loads. This facility provides important information on several goals of the "cryomodule string test" [7]. In addition, the construction of the Linear Coherent Light Source II (LCLSII) has been planned in the Stanford Linear Accelerator Center (SLAC), and will start to run in 2018. The LCLSII will consist of a 4 GeV SCRF linac based on ILC 1.3 GHz technology, to generate extremely bright electron beams [8]. As the European XFEL, the LCLSII will provide a solid SCRF technological base, bringing major labs in the field of cryomodule production.

An important technical challenge of ILC is the collision of extremely small beams of a few nanometers in size. The latter challenge has three distinct issues: creating small emittance beams, preserving the emittance during acceleration and transport, as well as focusing the beams to nanometers and colliding them. The Accelerator Test Facility (ATF) has been built at KEK to create these ultra-low emittance beams [9], at a beam energy of 1.3 GeV. In addition to ATF, several light sources are pushing the technology of low emittance rings, and achieving unprecedented low emittances in both horizontal and vertical planes. In 2011-2012, both the Australian Synchrotron Project (ASP) [10] and the Swiss Light Source (SLS) at the Paul Scherrer Institute (PSI) [11], achieved a vertical geometric emittance of 1 pm with a beam energy of 3 GeV and 2.4 GeV, respectively. On the other hand, the National Synchrotron Light Source II (NSLSII) [12], in the Brookhaven National Laboratory (BNL), has been constructed to achieve the lowest normalized horizontal emittance so far, 0.6 nm, with a beam energy of 3 GeV.

The ATF2 facility, which uses the beam extracted from the ATF DR, was constructed to address two major challenges of ILC: focusing the beams to nanometer scale using an ILC-like final focus system and providing nanometer stability [13]. Another key issue in the R&D of the ILC is the DR, needed to achieve the ultra-low vertical emittance required. In this framework three research areas have been identified: the development of methods to suppress the electron cloud instability and its impact on ultra-low emittance beams, undertaken mainly at the Cornell Electron-Positron Storage Ring Test Accelerator (CersTA) [14]; the demonstration of the ultra-low vertical emittance operation and the demonstration of fast injection/extraction systems undertaken in ATF.

1.1.2 The Compact Linear Collider

CLIC is being designed to have a centre-of-mass collision energy between 0.5-5 TeV, optimized for 3 TeV, and a luminosity of 10^{34}-10^{35} $cm^{-2}s^{-1}$. In order to reach this energy in a realistic and cost efficient scenario, the accelerating gradient has to

be very high –CLIC aims at an accelerating field of 100 MV/m, with a frequency of 12 GHz. This allows the accelerator to be “compact”, taking into account the energies to be reached and comparing with other linear collider projects. A design for 500 GeV has also been developed.

For the generation of the very high accelerating gradient, only klystrons are currently available as power sources. However, X-band klystrons working at a frequency of 12 GHz could not be feasible in terms of cost and maintenance. R&D is presently being carried out in X-band klystron technology, based on the accelerating structures developed in SLAC [15] and KEK [16]. In addition, CERN has constructed and is operating a klystron-based X-band test stand, called Xbox-1, dedicated to high-gradient testing of prototype accelerating structures [17], which uses a klystron built at SLAC able to produce 12 GHz RF [18]. Nevertheless, X-band klystron technology needs to be further developed. Therefore, in order to generate the required power for the short RF pulses, CLIC relies upon a novel two beam acceleration concept: the 12 GHz RF power is generated by a high current electron beam (drive beam) running parallel to the main beam, as shown in Fig. 1.3.

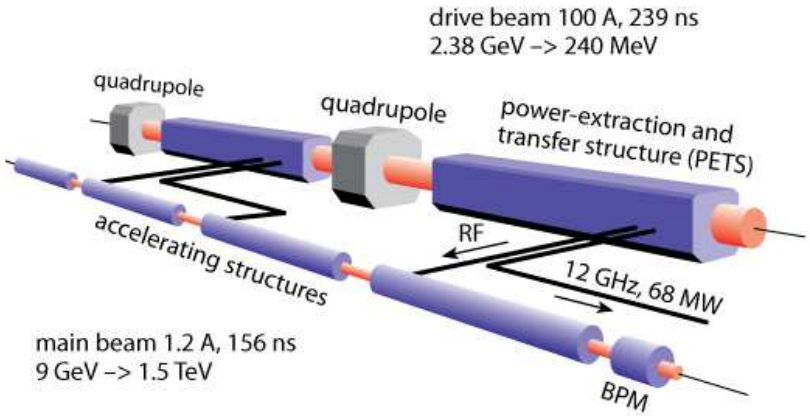

Figure 1.3: Two beam acceleration scheme [19].

The final layout of the collider for 3 TeV center-of-mass energy is shown in Fig. 1.4. The main beams are generated and pre-accelerated in the injector linacs, then enter the DRs for emittance reduction, and are extracted from the DRs with a normalized emittance of 500 nm in the horizontal plane and 5 nm in the vertical plane. These small emittance beams are further directed to the bunch compressor and transfer lines to the main linacs, where their energy reaches 1.5 TeV. To achieve this main beam energy, the drive beam is decelerated by means of the Power Extraction and Transfer Structures (PETS), and the generated RF power is extracted and transfered to the main beam. This leads to a very simple tunnel layout without any active RF components, i.e. klystrons. The main beams collide after a long BDS in one IP in the centre of the complex.

Main beam and main linac parameters are summarized in Table 1.2. In order to improve the RF to beam efficiency, a high charge per bunch is required, as well as

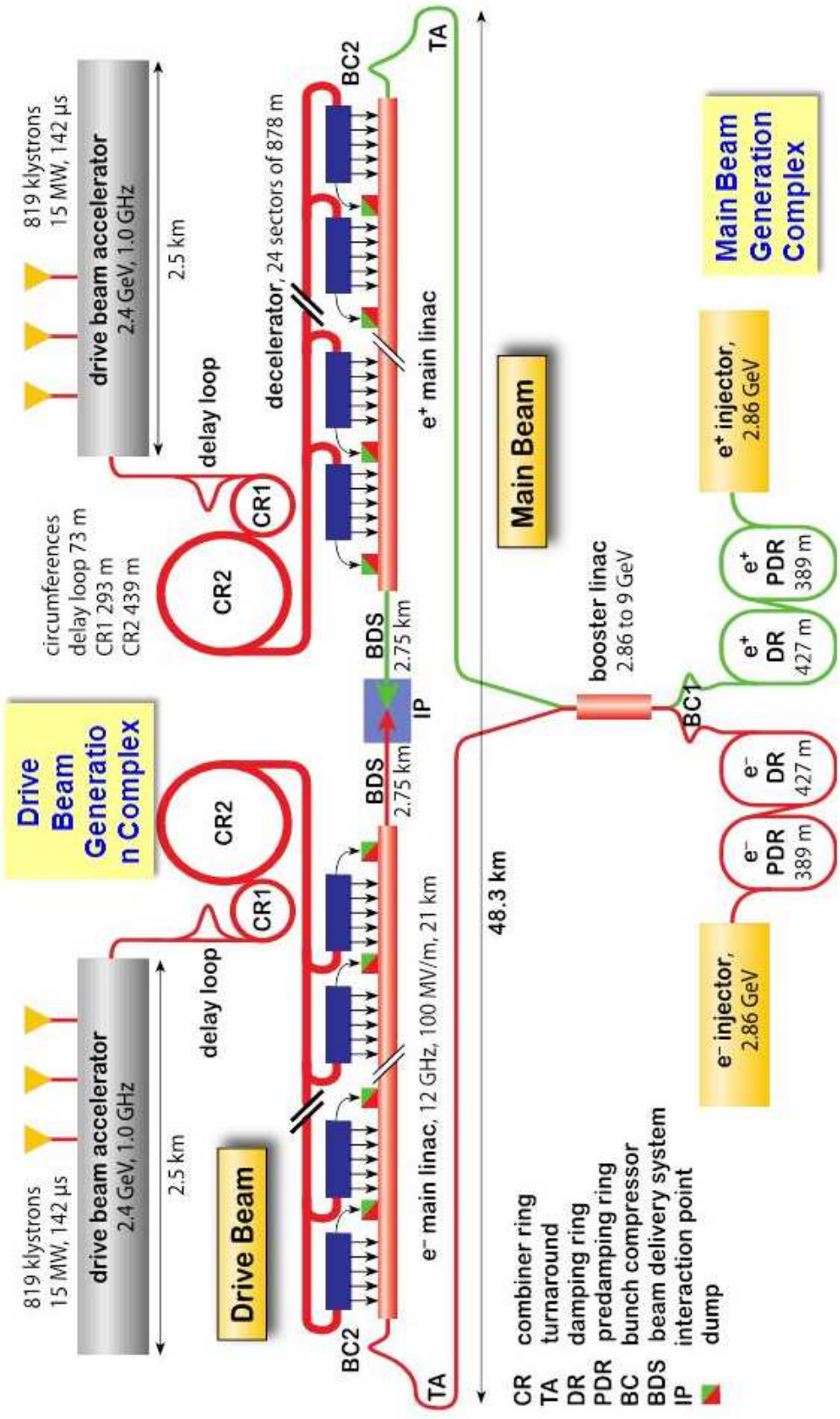

Figure 1.4: CLIC general layout at 3 TeV [19].

a large number of bunches per pulse with short bunch interval, which results in a challenging beam power of 14 MW per 1.5 TeV beam. Generation, handling, and machine protection systems with such high beam power are key issues.

Parameter	**Value**	**[Unit]**
Luminosity, $\mathcal{L}$	5.9×10^{34}	$[cm^{-2}s^{-1}]$
Total length, L	48.4	[km]
Accelerating gradient, G	100	[MV/m]
Linac RF frequency, f_{RF}	12	[GHz]
Number of bunches, n_b	312	
Bunch population, N	3.7×10^9	
Bunch separation, Δt_b	0.5	[ns]
Bunch length, σ_z	44	[μm]
Repetition rate, f_{rep}	50	[Hz]
Normalized horizontal emittance, $\gamma\epsilon_x$	0.66	[μm]
Normalized vertical emittance, $\gamma\epsilon_y$	20	[nm]
RMS horizontal beam size at IP, σ_x^*	40	[nm]
RMS vertical beam size at IP, σ_y^*	1	[nm]

Table 1.2: CLIC main parameters for the 3 TeV baseline [19].

The CLIC Conceptual Design Report (CDR) [19], published in October 2012, documents all aspects related to the two-beam acceleration scheme, both by comprehensive simulation studies of all parts of the machine and by a detailed experimental program in the CLIC Test Facility (CTF3) at CERN. CTF3 aims at demonstrating the feasibility of the CLIC scheme for multi-TeV e^+e^- linear collider. It is meant to demonstrate the technical feasibility of the key concepts of the novel CLIC RF power source, e.g., generation of high charge and high frequency electron bunch trains by beam combination in a ring using transverse RF deflectors, and operation with a fully loaded drive beam accelerator. CTF3 will also be used to test CLIC critical components and in particular will provide the 12 GHz RF power needed to test the main beam accelerating structures at the nominal gradient and pulse length, i.e. 100 MV/m for 140 ns.

1.2 Damping Rings in Linear Colliders

DRs for high energy e^+e^- colliders have a significant role for achieving high luminosity at the IP. The large emittance beams produced by the particle sources are damped in the DRs by several orders of magnitude producing ultra-low emittance beams necessary for high luminosity collisions within the repetition rate imposed by the collider. Moreover, DRs are required to damp the jitter in the incoming beams to provide very stable beams for delivery to the IP, and to delay the bunches coming from

the source in order to allow feedforward systems to compensate for pulse-to-pulse variations.

Fundamental to the performance of a DR is the damping of the transverse and longitudinal emittances. The emittance in any plane at a time t after injection is given by:

$$\epsilon(t) = \epsilon_{inj} e^{-2t/\tau} + \epsilon_{equ}(1 - e^{-2t/\tau}) \tag{1.5}$$

where ϵ_{inj} is the injected emittance, ϵ_{equ} is the equilibrium emittance, and τ is the damping time. Eq. (1.5) is usually the starting point for the design of a DR for a linear collider. The injected emittance depends on the particle sources. Positron production via a heavy metal target results in much larger emittances due to scattering, whereas electrons can be produced with much smaller emittances through an optimized design of the injector gun and its cathode. The values of the equilibrium emittances and damping times depend on the plane under consideration, and on a range of parameters related to the lattice design, the ring energy and the alignment of the magnets.

In DRs, the RF accelerating field used to compensate the energy lost by SR, collects the electrons into bunches, within which the individual electrons oscillate in longitudinal position and in energy relative to an ideal reference particle at the center of the bunch. This is called synchrotron oscillations. Furthermore, the magnetic field used to guide the electrons along the ring path, drives the electrons toward the ideal orbit, and causes them to execute transverse betatron oscillations about the ideal closed path. The energy lost by SR together with the compensating energy gain from the RF cavities gives rise to a slow damping of the synchrotron and betatron oscillations amplitudes, decreasing the beam emittance. However, the synchrotron and betatron oscillations damping is counteracted by the effect of quantum excitations, due to the random emission of photons of discrete energy, which increases the beam emittance. In stationary conditions a balance is reached between quantum excitation and radiation damping, leading to an equilibrium emittance [20]. This equilibrium emittance is affected by the collective effects, which dominate the beam dynamics in a DR.

The perfomance challenges of the DRs are driven by the key parameters of the linear collider and the requirements of the upstream and downstream systems, and mainly the efficiency of the main linac RF system. The technological choice of SCRF cavities, as in the ILC, over normal conducting RF cavities, as in CLIC, diversifies the design of DRs, although a number of design issues and challenges still remain common. In CLIC, the bunch trains are relatively short with even shorter bunch spacing and with a high repetition rate. The ILC bunch train is much longer, requiring a much longer ring circumference where the train is compressed and decompressed in a bunch-by-bunch beam transfer scheme. For getting the high luminosity in the ILC, the bunch charge is much higher, whereas CLIC targets for much smaller emittances. These emittances are unprecedented, specially in the vertical plane, aiming for an extracted normalized emittance of 20 nm and 5 nm for the ILC and CLIC DRs, respectively. However, several test facilities and other low emittance lattices in operation or under

construction, are rapidly approaching these regimes.

1.2.1 Collective Effects in Damping Rings

The high charge density associated with the large bunch current and low emittance, makes the beams in linear collider DRs susceptible to a several collective phenomena that may affect the operational performance. In the following the most critical collective effects for e^+e^- DRs are presented [20, 21]:

Space Charge (SC). The direct SC force is the Coulomb force between all the particles in the bunch. SC force causes a shift in each particle's tune, leading to an incoherent tune spread within the bunch. Particle's are also influenced by the environment (beam pipe, magnets, etc.), which generates indirect SC effects. The intrinsic effect of SC is important only at low energies, and vanishes for ultra-relativistic beams, where magnetic forces compensate electric forces. However, in electron and positron rings operating at low and medium energies, SC might be significant when dealing with high intensity beams.

Intrabeam scattering (IBS). Multiple small-angle collisions within a bunch couple the transverse and longitudinal particle's oscillations, and lead to an increase in beam emittance in both planes. This effect is more critical in proton machines, and it can limit the luminosity lifetime of an hadron collider. In electron machines, IBS is counteracted by radiation damping; however, if the particle density in a bunch is high enough, i.e. large bunch population and small emittances, and the energy is not too high, then emittance growth from IBS may be significant.

Coherent Synchrotron Radiation (CSR). A relativistic electron beam moving in a circular orbit can radiate coherently if the wavelength of the SR exceeds the length of the bunch. The constructive interference of the radiation can be a detrimental effect when dealing with low emittance beams, high charge bunches and short bunch lengths. CSR can contribute to an increase in emittance and energy spread, and can limit the process of bunch compression.

Short-range wakefields. Beam particles in a bunch might be affected by the short-range wakefields generated by leading particles in the same bunch, driving single-bunch instabilities. These short-range wakefields can be produced in all the discontinuities of the beam pipe, as well as in several non-resonating objects, like pick-ups and kickers. In order to define the instability threshold and the impedance budget, the broadband impedance model is used, which model the global effect of all the potential sources of short-range wakefields. The longitudinal broadband impedance may create turbulent bunch lengthening, whereas transverse broadband impedance may produce fast head tail instability.

Long-range wakefields. Bunch trains are susceptible to coupled-bunch instabilities driven by long-range wakefields. Long-range wakefields generated by the leading bunches cause deflecting transverse kicks on the trailing bunches, producing an exponential growth of the bunch oscillations. There are two main sources of long-range wakefields in storage rings: the resistive wall impedance, which depends on the aperture and material of the vacuum chamber, and the higher-order modes produced in the RF cavities.

Fast ion Instability (FII). The ionization of residual gas in the vacuum pipe by the circulating electron beam will create positive ions which will, under certain circumstances, become trapped in the potential well of the stored beam. The accumulation of these ions depends on several factors, e.g. the number of bunches, bunch spacing, the beam current, transverse beam sizes and the mass of trapped ions. It may lead to beam tune shift and spread, emittance blow-up, and coupling of horizontal and vertical motion.

Electron Cloud Instability (EC). In the beam pipe of a positron or proton storage ring, an EC may be produced by the photoelectrons generated when the SR photons hit the vacuum chamber walls, or by ionization of residual gases, and then increased by the secondary emission process. The EC density depends on beam properties, such as bunch length, bunch charge and bunch spacing, as well as on the secondary electron yield of the beam pipe wall. The EC can lead to beam instability and losses, ultimately producing a reduction in the collider luminosity.

1.2.2 The ILC Damping Rings Complex

At ILC the DR complex consists of one electron and one positron ring, as shown in Fig. 1.2, operating at a beam energy of 5 GeV. Both rings, with a circumference of 3.2 km each, are housed in a single tunnel with one ring positioned directly above the other. The DR complex is located in the central region, horizontally offset from the interaction region by approximately 100 m to avoid the detector hall. The design parameters of the ILC DRs are given in Table 1.3.

The ILC DRs must accept electron and positron beams with large transverse and longitudinal emittances and damp them to the low emittances required for luminosity production. In addition, the ILC bunch train structure with 2625 uniformily spaced bunches with 366 ns between them cannot fit to a reasonable ring circumference. Thus, the long bunch train has to be compressed into a much shorter ring, and it has to be decompressed while extracted, through a bunch-by-bunch extraction scheme.

The DR lattice follows a racetrack design, as shown in Fig. 1.5. The two arc sections are constructed from 75 Theoretical Minimum Emittance (TME) cells. One of the two 712 m long straight sections accommodates the RF cavities, damping wigglers,

Beam parameters	**Value**	**[Unit]**
Beam energy, E	5	[GeV]
Circumference, C	3.2	[km]
Bunch population, N_b	2.0×10^{10}	
Extracted norm. horizontal emittance, $\gamma\epsilon_x$	5.7	[μm]
Extracted norm. vertical emittance, $\gamma\epsilon_y$	20	[nm]
Number of bunches, n_b	2820	
Bunch spacing, Δt_b	6.1	[ns]
Bunch length, σ_z	6	[mm]

Table 1.3: Beam parameters for the ILC DRs [2].

and a variable path length to allow changes in phase (phase trombone), while the other contains the injection and extraction systems, and a circumference-adjustment chicane.

The many collective effects that may affect beam quality in the ILC DRs were examined during the original baseline configuration studies [22]. These include impedance driven instabilities, due to both short-range and long-range wakefields, IBS, SC effects, EC effects in the positron ring and FII in the electron ring. The largest sources of emittance dilution were found to be the EC instability in the positron DR and the FII in the electron DR. A trade-off is necessary between the bunch spacing in the ring, which should be the longest possible for reducing EC build-up and increasing the extraction kicker rise/fall times, and its circumference, being the shortest possible for cost but also reduction of single bunch collective effects, such as SC and IBS. Mitigation of the FII in the electron DR is achieved by limiting the gas pressure to below 1 nTorr and by the use of short gaps in the ring fill pattern and a fast transverse feedback system, similar to those used in B-factories.

1.2.3 The CLIC Damping Rings Complex

The CLIC DRs complex, consists of two PDRs and two DRs, as shown in Fig. 1.4. The four rings, operating at a beam energy of 2.86 GeV, will be required to damp both the electron and the positron beams. Once the beam is damped to the final emittance values, it is extracted from the DRs, and injected into the booster linac, where the beam will be accelerated up to 9 GeV. The large input emittance and energy spread, especially coming from the positron source and the high repetition rate of 50 Hz, require that the beam damping was performed in two stages, with a PDR for each particle species.

Two RF baselines are considered for the DR operation: 1 GHz and 2 GHz RF systems. The main linac operates with a 2 GHz RF baseline; however, the transient beam loading would be very challenging in DRs with a 2 GHz RF system, due to the very high peak and average current of a full train of 312 bunches spaced by 0.5 ns (Table 1.5). In the 1 GHz baseline, two bunch trains with 1 ns bunch spacing reduce

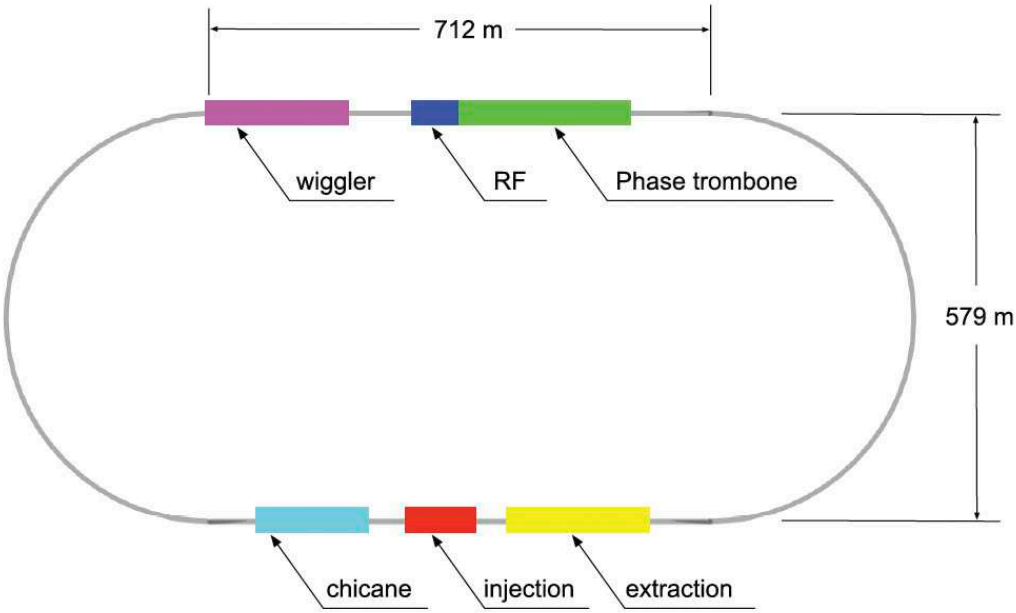

Figure 1.5: ILC DR layout [2].

significantly the beam loading, however the trains have to be recombined in a delay loop downstream of the DRs with an RF deflector, as shown in Fig. 1.6. In this case, the head of each train is separated by half of the DRs circumference. The two trains are damped simultaneously and then extracted in a single turn from the DRs. The same delay loop is used for both species and the downstream systems have different path lengths to compensate for the time delay between the positron and electron trains [19].

CLIC Pre-Damping Rings

The PDRs are needed to accommodate the large emittance bunches from the electron/positron injectors, and damp them to emittances that are small enough to be injected into the DR without losses. For electrons, the PDRs will damp the normalized beam emittance from 100 μm to 63 μm, in the horizontal plane, and from 100 μm to 1.5 μm, in the vertical plane. For positron beams, the PDRs are more challenging: they have to damp the input emittance of 7 mm to the same output emittances as for the electrons, in both vertical and horizontal planes. The positron beam has also a large energy spread which reduces the capture efficiency in the PDRs and requires a much larger bunch population in the ring.

The CLIC PDRs have a racetrack configuration, as it is shown in Fig. 1.7, with a length of 389.15 m. Each arc section has dipoles surrounded by doublet quadrupoles forming 17 TME cells. The long straight sections are composed of 13 FODO cells with normal conducting damping wigglers. The target emittances of the PDRs are not

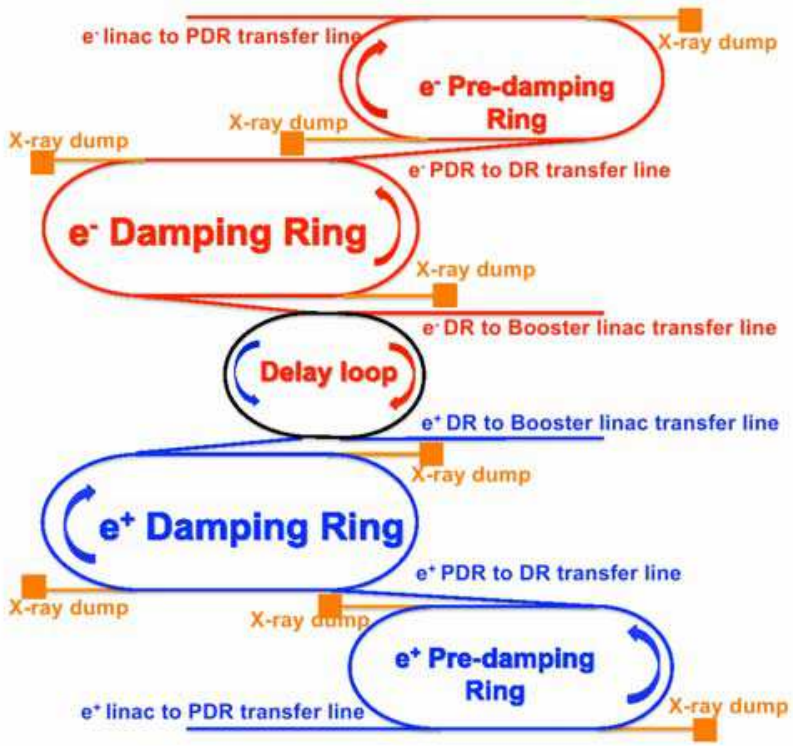

Figure 1.6: CLIC DRs complex layout [19].

extremely low and therefore the TME cells can be strongly detuned from the absolute minimum emittance. However, TME cells are chosen for their compactness, which reduces the overall size of the ring. The electron PDR design parameters are summarized in Table 1.4.

Collective effects are not expected to present serious limitations in PDRs as compared to the main DRs. The bunch population is moderately higher but the transverse emittance and bunch length are much larger, so SC effects are negligible. IBS is also negligible causing an emittance growth of less than 0.1%. The longer bunches and the larger vacuum chamber aperture increases significantly the thresholds for broadband impedance (short-range wakefields) and resistive wall impedance (long-range wakefields). FII in the electron PDR is not a problem due to the larger beam sizes and can be mitigated by moderately low vacuum pressure, whereas the EC in the positron PDR needs to be mitigated with special coatings for reducing the secondary electron yield, similar to the ones used in the positron DR.

CLIC Damping Rings

The role of the DRs is to provide the final stage of damping to the required low emittance at a fast repetition rate of 50 Hz. The normalized emittance requirements are extremely low, 500 nm in the horizontal plane, and 5 nm in the vertical plane, in

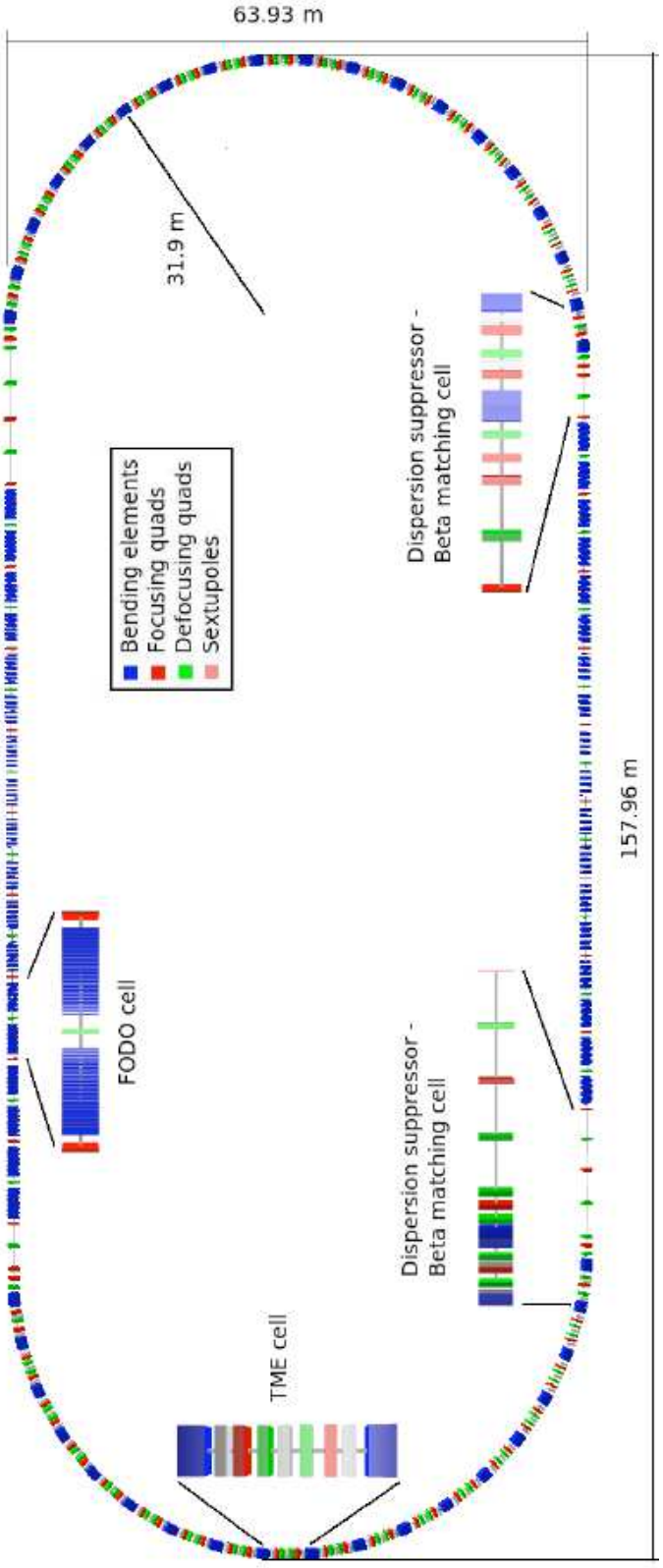

Figure 1.7: CLIC PDR layout [19].

Beam parameters	**Value**		**[Unit]**
	1 GHz	2 GHz	
Beam energy, E	2.86		[GeV]
Circumference, C	389.15		[m]
Bunch population, N_b	4.3×10^9		
Extracted norm. horizontal emittance, $\gamma\epsilon_x$	63		[μm]
Extracted norm. vertical emittance, $\gamma\epsilon_y$	1.5		[μm]
Number of bunches, n_b	156	312	
Bunch spacing, Δt_b	1	0.5	[ns]
Bunch length, σ_b	3.2	4.6	[mm]

Table 1.4: Beam parameters in the PDRs for electrons [19].

spite of the high bunch intensity of 4.1×10^9, at the given energy of 2.86 GeV.

The CLIC DRs have a racetrack configuration, as it is shown in Fig. 1.8, with a length of 427.5 m. Each arc is filled with 48 TME cells, and 2 half cells at either side for dispersion supression. The straight sections are filled with 13 FODO cells each, and include normal conducting damping wigglers. The injection and extraction regions are in the dispersion free sections upstream of the wigglers, while the RF cavities are downstream of this long straight section.

The design challenges of the CLIC DRs are driven by the extremely high bunch density and the collective effects associated. In this respect, the design parameters of the DRs, summarized in Table 1.5, have been carefully chosen and optimized in order to mitigate these effects. In addition, these parameters drive the technology of a number of components such as wigglers, RF system, kickers, vacuum, instrumentation and feedback. This thesis is devoted to the extraction kicker from CLIC DRs and it will be introduced in Chapter 2. A detailed description of the kicker design, manufacturing and laboratory measurements will be found in further chapters.

Beam parameters	**Value**		**[Unit]**
	1 GHz	2 GHz	
Beam energy, E	2.86		[GeV]
Circumference, C	427.5		[m]
Bunch population, N_b	4.1×10^9		
Extracted norm. horizontal emittance, $\gamma\epsilon_x$	0.5		[μm]
Extracted norm. vertical emittance, $\gamma\epsilon_y$	5		[nm]
Number of bunches, n_b	156	312	
Bunch spacing, Δt_b	1	0.5	[ns]
Bunch length, σ_b	1.6	1.8	[mm]

Table 1.5: Beam parameters in the DRs for electrons [19].

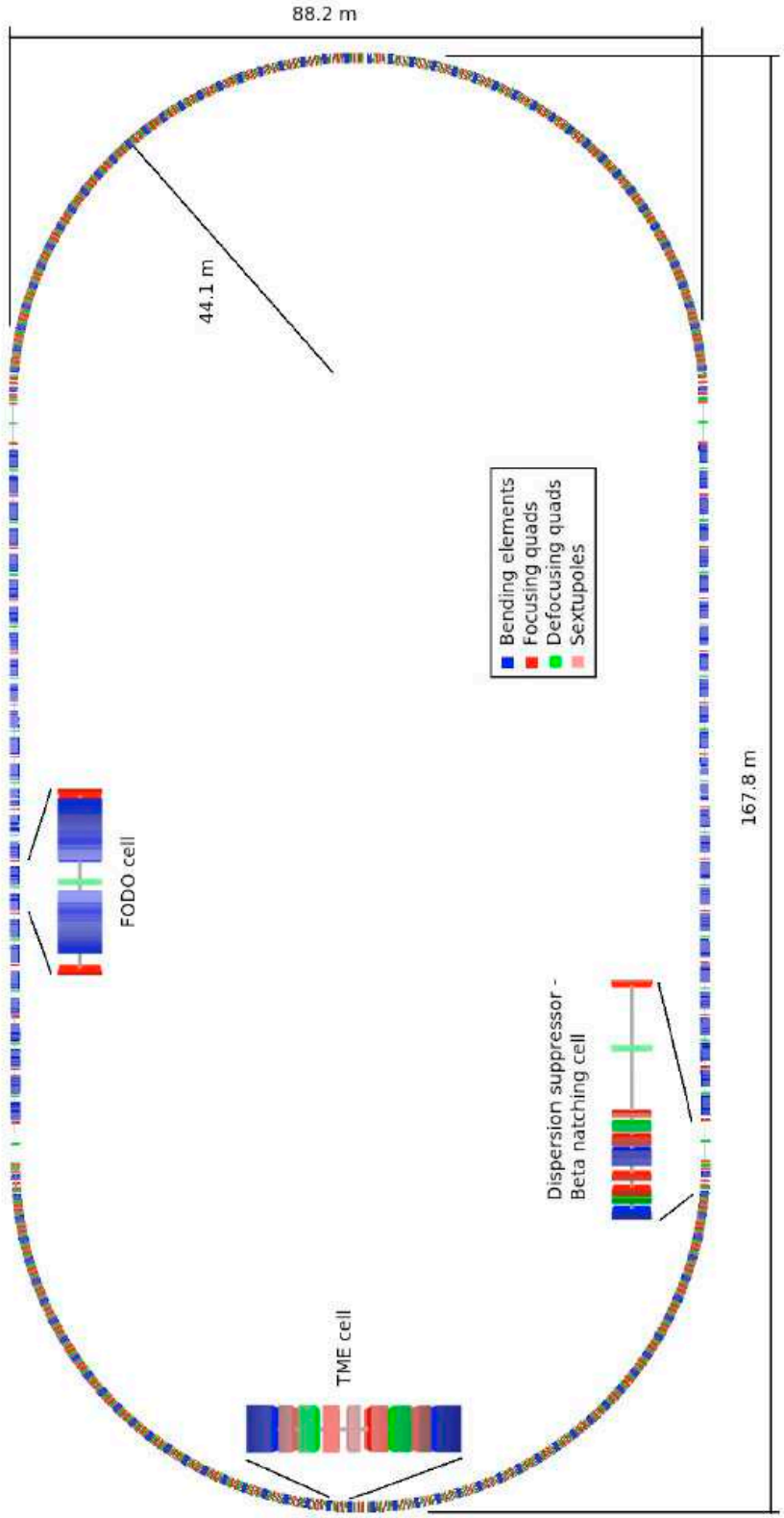

Figure 1.8: CLIC DR layout [19].

From the collective effects point of view, an impedance budget has been defined, taking into account the different impedance contributions such as the broadband resonator model in combination with the resistive wall contribution from the arcs and the wigglers of the DRs [23]. The IBS effect is reduced when increasing the energy; in this respect, the energy of 2.86 GeV was chosen for the CLIC DR, which is close to a steady state emittance minimum but also reduces the IBS impact [24]. A measurement campaign in CesrTA and the Swiss Light Source (SLS) has been initiated for evaluating the IBS effect and benchmark theories and simulation codes. In addition, due to the very small beam size, especially in the vertical plane, the SC effect needs to be diminished, by reducing the ring circumference as much as possible. At the same time, the bunch length has to be increased without affecting the performance of the downstream bunch compressors.

Simulation studies about EC and FII are being carried out [25]. To mitigate EC build-up in the positron ring, low secondary electron yield is achieved with special chamber coatings. Several mitigation techniques are presently under study, in particular, an amorphous carbon coating has been extensively tested at SPS and later at CesrTA, with promising results with respect to secondary electron yield and photo emission. In the electron DR, FII is reduced by coating the vacuum chambers with Non-Evaporable Getter (NEG) for increasing pumping and vacuum conditioning: with a gas pressure of 1nTorr, the induced tune shift introduced by the ion cloud at the end of the train is moderate. In addition, the train gaps, i.e. distance from train to train, have also proved to provide a natural cleaning mechanism for the trapped ions.

Chapter 2

Injection and Extraction Systems for Circular Accelerators

2.1 Introduction

In order to reach high energies, high energy accelerators need a chain of acceleration stages, due to each accelerators limited dynamic range. Beam transfer between the different stages of an accelerator requires injection, extraction and beam transfer lines. Injecting or extracting particles into or from a circular accelerator should be done with minimum beam loss and placing the injected and extracted particles onto the correct trajectory with the correct phase space parameters.

A combination of septa and kickers is frequently used to inject and extract beam from each stage. The kicker typically produces rectangular field pulses with fast rise and fall times; however, the field strength is relatively low. To compensate for their low field strength, the kickers are combined with septa. The septa provide relatively strong field strength but are either DC or slow pulsed.

A septum is a kind of dipole with homogeneous magnetic field to deflect injected or extracted beam, without disturbing the circulating beam. This is possible because the septum creates a spatial separation between two field regions: one region with homogeneous high field, to deflect the beam, and the other region with very low (ideally zero) field so as not to affect the circulating beam. Hence a septum provides a space separation of circulating and the injected or extracted beam. Two types of septa exist: electrostatic and magnetic septa. An electrostatic septum is a DC electrostatic device with very thin ($\sim \mu$m) separation between the zero field and high field regions. A magnetic septum is either a pulsed or DC dipole magnet with a thin ($\sim$ mm) separation between the zero field and high field regions [26].

A kicker system, by contrast, provides a time selection of the beam to be deflected, by producing a pulsed electrostatic, magnetic or electromagnetic field. The pulsed field produced by a kicker must rise and fall within the time period between the beam bunches or bunch trains, so typical rise and fall times are of the order of tens of ns to

μs, and pulse widths in the range of μs to tens of μs are usually required. In addition, the pulsed field must not significantly deviate from the flat top of the pulse or from zero between pulses, i.e. only very small pulse ripple and excursions are allowed. If a kicker exhibits a time-varying structure in the field pulse shape, this can translate into small offsets with respect to the closed orbit. Thus a fast, low-ripple kicker system is generally required for injection and extraction [27].

2.2 Injection and Extraction

In transferring the beam from one accelerator to another, preservation of the beam properties is essential. Injection should be accomplished with minimum beam loss and minimal emittance dilution. Single-turn injection, in which a single bunch of particles is injected in a single empty RF bucket, is usually straightforward. In many cases, however, to attain higher bunch currents, one may also wish to accumulate beam in a storage ring by reinjecting different beam pulses into the same RF bucket. This is called multi-turn injection.

Extraction refers to the removal of the beam from an accelerator. It is roughly the reverse process of injection. One difference is that usually at extraction the beam energy is higher, although this is not the case for a DR. A high extraction efficiency is necessary to avoid activation of accelerator components and also to make optimum use of the extracted beam, e.g. to achieve the maximum luminosity. Which extraction procedure is chosen depends on the specific application. Fast one-turn extraction is used for transferring bunches between different circular machines in an accelerator chain. For fixed-target experiments, slow extraction by the controlled excitation of nonlinear betatron resonances is a common technique, which provides a slow uniform depletion of particles in the ring.

In addition to these conventional schemes, several other injection and extraction techniques exist [28].

2.2.1 Single-turn Injection and Extraction

Single-turn injection and extraction consists of injecting or extracting one single pulse into or from a circular accelerator. Horizontal single-turn injection in one plane uses a septum magnet and a fast kicker element, as shown schematically in Fig. 2.1. The kicker is located at a point downstream from the septum unit with a phase advance of $\pi/2$. The septum and kicker are either side of a quadrupole, defocusing in the injection plane, which provides some of the required deflection and minimizes the required strength of the kicker.

The injected beam passes through the homogeneous field region (gap) of the septum, whereas the circulating beam is in the field-free region. The septum deflects the injected beam onto the closed orbit at the centre of the kicker, and the kicker compensates the remaining angle. As the injected beam is put on the ring axis at the exit of

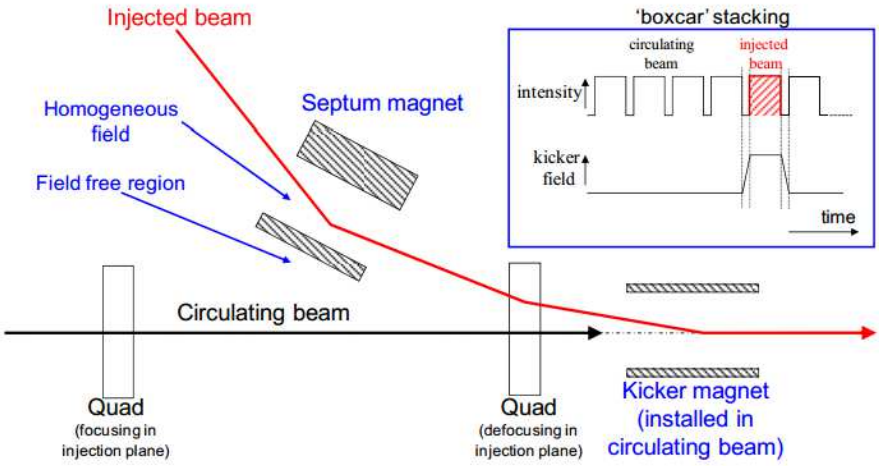

Figure 2.1: Fast single-turn injection in one plane [27].

the kicker, this is also called on-axis injection. The circulating beam is in the aperture of the kicker, therefore the septum and the kicker should not act on the injected beam when it comes back after one turn, otherwise it would be thrown out of the acceptance of the accelerator. This requires that the fringe field of the septum has an acceptable level, as well as the kicker field must be reduced to zero in a time that is short compared to the revolution period. Furthermore, the kicker field must rise from zero to full field in the time interval between the circulating beam and the start of the injected beam, and fall from full field to zero field in the time interval between the end of the injected beam and the subsequent circulating beam. For bunch-by-bunch injection, the kicker field must rise and fall within the time period between the beam bunches.

For single-turn extraction, orbit bumps are generated which move the circulating beam close to the septum magnet, as shown in Fig. 2.2. When the kicker is powered, the beam passing through the kicker is deflected towards the septum, and the septum deflects the entire kicked beam into the transfer line. The extracted beam passes through the homogeneous field region of the septum, whereas the circulating beam, prior to extraction, is in the field-free region of the septum. The most efficient extraction, i.e. lowest deflection angle required, occurs when the phase advance between the kicker and septum is $\pi/2$. As for single-turn injection, the circulating beam is in the aperture of the kicker. Thus the kicker field rise time must be short compared to the revolution period of the ring, then only a small fraction of the particles are lost. For bunch-by-bunch extraction, the rise time must be shorter than the time interval between two successive circulating bunches. The pulse length and fall time of the kicker are determined by the number of bunches to be extracted, and by the ring fill pattern [27].

The angular deflection that the kicker must give to the beam for single-turn injection and extraction in the horizontal plane is given by Eq. (2.1) [28]:

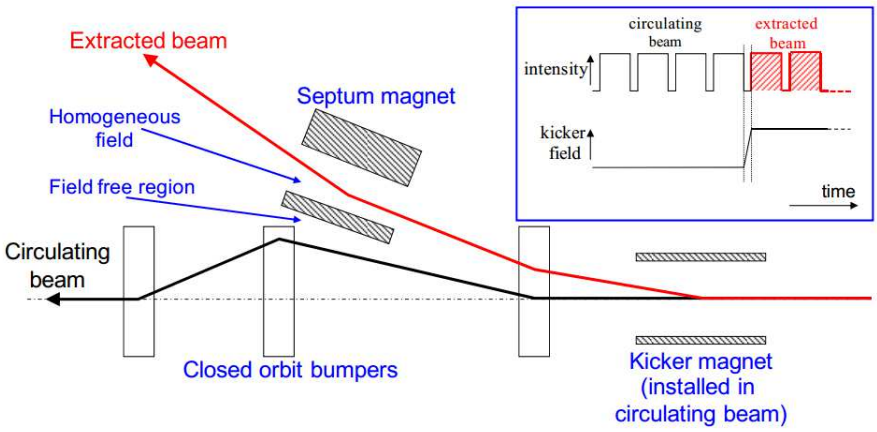

Figure 2.2: Fast single-turn extraction in one plane [27].

$$\theta = \frac{x_{sep}}{\sqrt{\beta_{x,sep}\beta_{x,kick}}\sin\Delta\mu_x} \tag{2.1}$$

where x_{sep} is the transverse displacement of the beam at the septum exit (for injection) or at the septum entry (for extraction), $\beta_{x,sep}$ and $\beta_{x,kick}$ are the horizontal β-functions at the septum and at the kicker position, respectively, and $\Delta\mu_x$ is the phase advance between the septum and the kicker. For single-turn exctraction, the initial orbit bump is used to reduce the value of x_{sep}. To minimize the kicker angle, large β values at the septum and kicker locations are required, as in the case of a standard FODO lattice.

The single-turn injection and extraction is used in the ATF DR [29] for bunch-by bunch manipulation. For the ILC DRs, the injection and extraction will be also bunch-by-bunch, whereas in the CLIC DRs one or two train of bunches will be injected or extracted at the same time, depending on the RF choice, as shown in Table 1.5.

2.2.2 Multi-turn Injection and Extraction

Most storage rings use multi-turn (off-axis) injection in order to accumulate many incoming trains of particles. Furthermore, many physics experiments and medical accelerators need a quasi-continuous flux of particles, by means of multi-turn extraction. A general scheme of multi-turn injection is shown in Fig. 2.3. Different techniques are employed for electrons and positrons than for protons or heavier particles.

In case of electron and positron rings, radiation damping is used for the injection. First, a single bunch is injected. Then the orbit bump is reduced over a few revolution periods. After a few damping times, when the beam size has shrunk to its equilibrium value, the orbit bump is reintroduced, and another bunch is injected into the same bucket.

For proton or heavy ion beams, the multi-turn injection is described as phase-space painting. In this case, the orbit bump is reduced slowly in time, and bunches are injected into different regions of the ring acceptance, so that the early bunches occupy the central region, and the later ones the outer parts of the acceptance. Some emittance dilution is inherent to this scheme, and much larger emittance dilutions arise at low beam energy or high intensity, when space charge effects are important. Another possibility is to install two kickers in the ring, powered by the same pulse generator. Only one of the kickers deflects the injected beam, however both kickers act on the circulating beam. If the phase advance between the two kickers is π or 2π, and the sign of the kick is appropriately chosen, the kicker deflections generate a closed bump for the circulating beam [28].

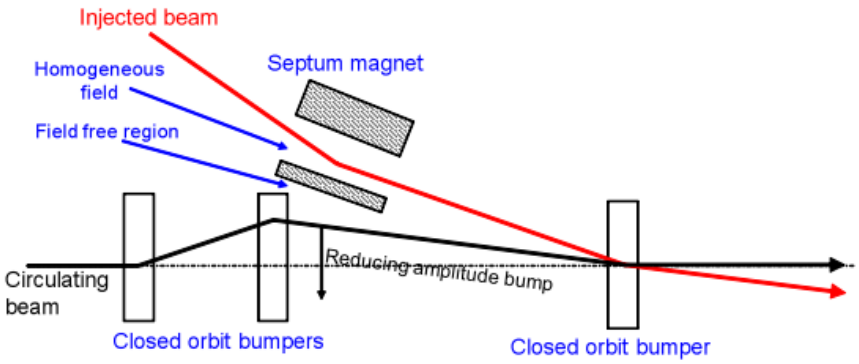

Figure 2.3: Multi-turn injection in one plane [26].

For multi-turn extraction, shown in Fig. 2.4, two techniques can be used: non-resonant and resonant extraction, mainly used for proton beams. When extracting the beam with the non-resonant method, a fast bumper deflects the whole beam onto the septum, and only a fraction of the beam is extracted. The main disadvantage of the non-resonant method is that this technique is intrinsically a high-loss process.

To improve the efficiency of the multi-turn extraction method, the beam can be slowly extracted by exciting a third order non-linear resonance, using sextupoles. This is the resonant method for multi-bunch extraction. As shown in Fig. 2.5, particles are first distributed in a circular normalized phase space. The sextupole fields distort the phase space and produce a triangular stable area. The particles inside the triangle area are stable, with small amplitude oscillations. Outside the triangle, the oscillation amplitude of the particles grows exponentially; therefore, particles in this region are rapidly lost, along the triangle branches. Then, the stable area is reduced adjusting the strength of the sextupoles and the betatron tune, and more particles reach the unstable area and are extracted. Finally, as the tune approaches to zero, the particles with very small amplitude are extracted. It is possible also to extract the beam by using non-linear fields produced not only by sextupoles, but octupoles too. This method consists of creating stability “islands” in the phase space, and has the advantage of reducing drastically beam losses.

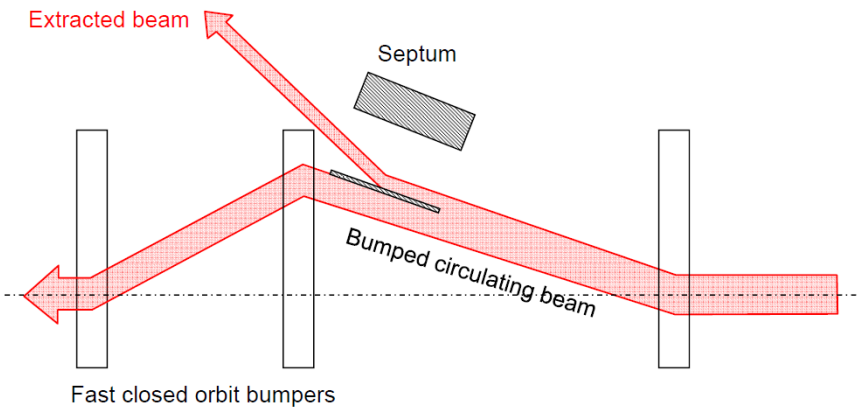

Figure 2.4: Multi-turn extraction in one plane [30].

The multi-turn injection scheme is used for example at CERN for beam injection into the Proton Synchrotron Booster (PSB). The beam extraction from the Proton Synchrotron (PS) at CERN is carried out by means of the non-resonant multi-turn extraction, whereas the beam extraction from the CERN SPS is done using the resonant technique [30].

2.3 Kicker Technology

Kickers are devices which create very fast fields to deflect charged particles. They are usually driven by a pulsed waveform with very fast rise or fall times, typically less than 1 μs, and good flat-top stability. A good pulse flat-top is required for uniform deflection of the whole beam or bunches of the beam. The field pulse must start and stop when the bunch or train of bunches enters or leave the kicker, respectively. When the field is interrupted inside the bunch or train of bunches, the device can be referred as a clipper [31].

The deflecting field in a kicker can be electric, magnetic or electromagnetic, as all these fields can deflect charged particles. For a charged particle q passing through an electric, magnetic or electromagnetic field, the force is governed by the Lorentz force equation:

$$\mathbf{F} = q[\mathbf{E} + (\mathbf{v} \times \mathbf{B})] \tag{2.2}$$

where **E** is the electric field, **B** the magnetic field, and **v** is the instantaneous velocity of the particle.

The horizontal deflection of a charged particle beam due to a vertical magnetic field B_y is given by the equation [27]:

$$\theta_{B,x} = \frac{0.3}{p} \int_{z_0}^{z_1} |B_y| dz = \frac{0.3L}{p} |B_y| \tag{2.3}$$

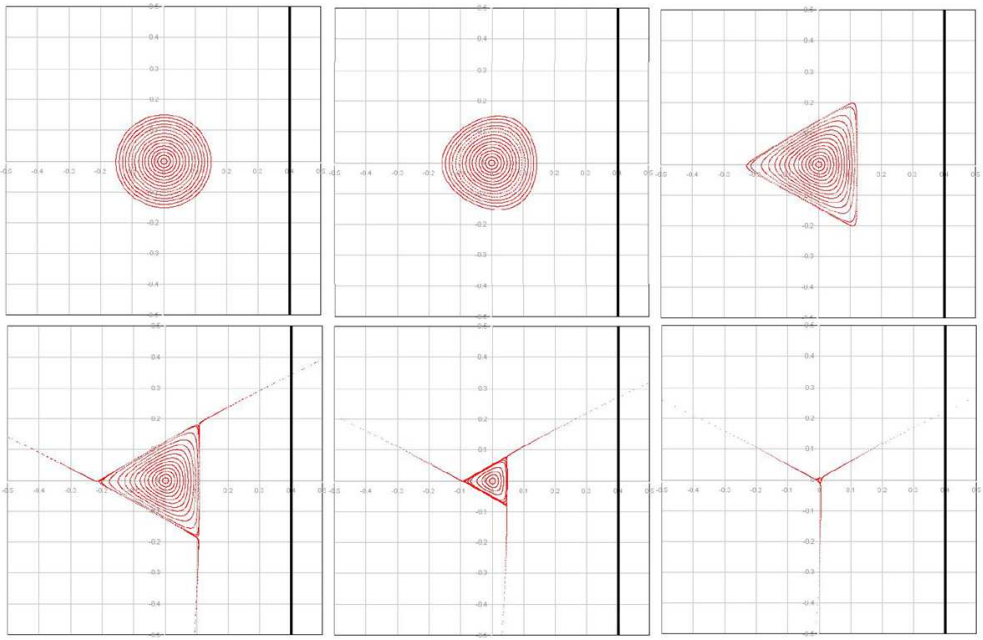

Figure 2.5: Third-order resonant extraction [30].

where p is the beam momentum, and L is the effective length of the magnet. The horizontal deflection of a charged particle beam with velocity $\beta = v/c$, due to an horizontal electric field E_x is given by [27]:

$$\theta_{E,x} = tan^{-1}\left[\frac{1}{(p \cdot 10^9)\beta}\int_{z_0}^{z_1}|E_x|dz\right] = tan^{-1}\left[\frac{|E_x|L}{(p \cdot 10^9)\beta}\right] \tag{2.4}$$

Therefore, kickers can be classified according to the deflecting field produced as magnetic kickers, electrostatic kickers and electromagnetic kickers (also known as stripline kickers), and they are described in the following.

2.3.1 Magnetic Kickers

Magnetic kickers, as shown in Fig. 2.6, are generally ferrite-loaded transmission line type magnets with a rectangular aperture of dimensions H_{ap} and V_{ap} embedding a coil. The horizontal deflection produced by a kicker magnet can be calculated from Eq. (2.3), where the flux density in the aperture B_y of the kicker is given by the equation:

$$B_y \approx \mu_0\left(\frac{NI}{V_{ap}}\right) \tag{2.5}$$

with $\mu_0 = 4\pi \times 10^{-7}$ H/m being the permeability of free space, N the number of turns, I the magnet current, and V_{ap} the distance between the inner edges of the legs of the ferrite.

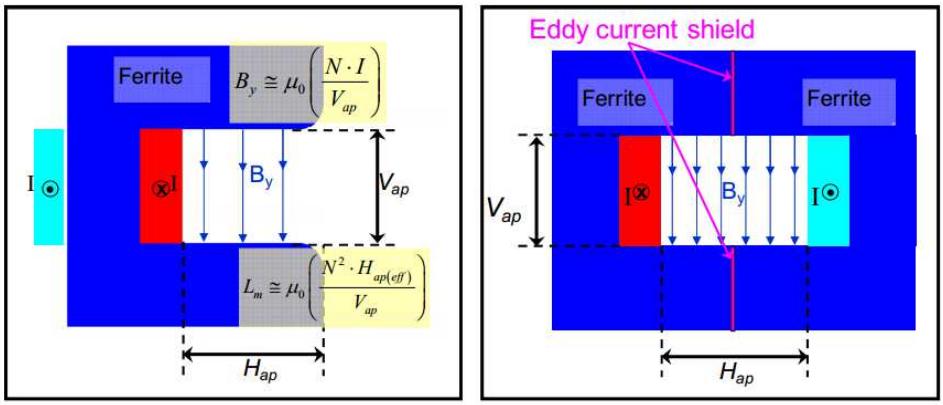

Figure 2.6: Cross-section of a typical C-core (left) and window frame (right) magnetic kicker. Window frame topology has been used in Fermi National Accelerator Laboratory (FNAL) and KEK for reducing filling time by a factor of two [27].

Magnetic kickers have some design concerns. Firstly, it is very difficult to get good field uniformity for large apertures and flat-top stability for fast rise time pulses. Moreover, magnetic kickers usually represent the highest contribution to the beam impedance in the accelerator. Longitudinal beam coupling impedance is significantly reduced by using serigraphy in the ferrites or by placing screen conductors within the kicker aperture. In addition, this high beam impedance can be avoided by using the two other types of kicker: electrostatic and stripline kickers [27].

2.3.2 Electrostatic kickers.

They consist of two parallel electrodes inside a vacuum pipe. Each electrode is driven by one electrical feedthrough to charge the capacitor formed by both electrodes and it is supported by an insulating stand-off. The field uniformity is given by the electrodes cross section and their position, i.e. the distance between them, like in a capacitor. When the electrodes are capacitively charged by a slow current source, the injected beam is deflected by the electrostatic field, and there is no magnetic field contribution. Electrostatic kickers are easier to manufacture than magnetic kickers, feature extremely good flat-top stability and very low beam impedance for smaller apertures. However, the technological restrictions about handling high electric fields, i.e high voltages, are the main problem for these devices not being very powerful. Furthermore, they usually need charging times in the order of a few μs [31].

The horizontal deflection produced by an electrostatic kicker is given by Eq. (2.4), where the electric field E_x is given by:

$$E_x = \frac{2V_k}{a} \tag{2.6}$$

where V_k is the voltage applied to an electrode, and a the aperture of the kicker, i.e.

the distance between the electrodes. The factor of 2 assumes that both electrodes are charged to equal magnitude but opposite polarity voltages.

A new type of electrostatic kicker, shown in Fig. 2.7, will be used to inject heavy ion particles in the KEK Digital Accelerator (KEK-DA), which is being planned as a new induction synchrotron, and will replace the KEK 500 MV booster Proton Synchrotron (PS) in Tsukuba [32]. The design consists of a number of intermediate electrodes between the two main electrodes in order to ensure field homogeneity throughout the beam passage [33].

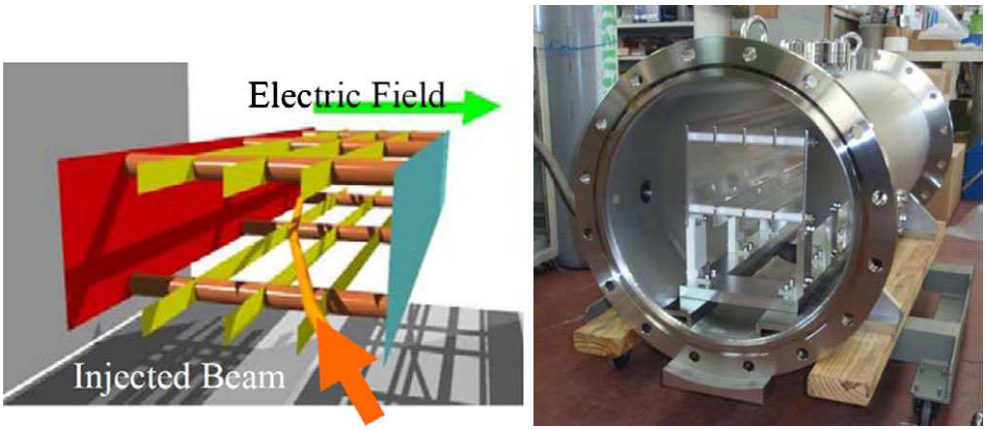

Figure 2.7: Electrostatic kicker for the KEK-DA [33].

2.3.3 Electromagnetic or Stripline kickers.

They also consist of two parallel metallic electrodes supported by ceramic standoffs inside a vacuum chamber. Nevertheless, the electrodes are connected at the ends by two feedthroughs each, to allow for power input and output, as shown in Fig. 2.8.

The field uniformity is given by the electrodes cross section and the distance between them, as for the electrostatic kickers. The structure is similar to a pair of striplines where each electrode forms a transmission line with the half beam pipe. Therefore, the working method consists of an electromagnetic wave that propagates along the striplines at the speed of light. In order to generate a transverse kick, the kicker should be driven in differential mode. Consequently, the ports located downstream of the beam direction should be powered by opposite polarity generators and the upstream ports should be connected to dissipation loads. Otherwise, the electric and magnetic fields of the electromagnetic wave would subtract each other or even be null in the kicker axis. This kind of excitation gives an electric and magnetic field distribution, known as Transverse Electromagnetic (TEM) mode, that generates a combined Lorentz force over the charged particles. For relativistic beams, $|E|$ is related with $|B|$ by the speed of light c in lossless TEM propagation mode. Therefore, the Lorentz

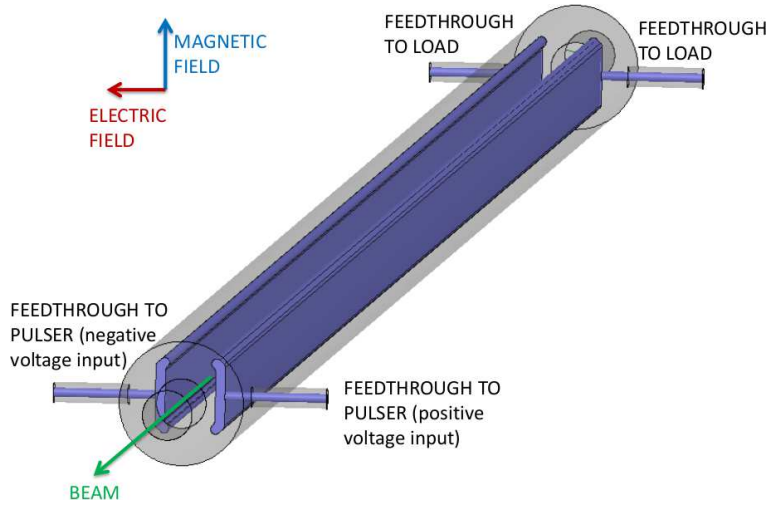

Figure 2.8: Scheme of a stripline kicker.

force effectuated by the electric field **E** is similar to the Lorentz force generated by the magnetic field **B** over a charged particle q:

$$F = q(\mathbf{E} + \mathbf{v} \times \mathbf{B}) = 2qE \tag{2.7}$$

This relation makes these devices more powerful than electrostatic kickers in terms of efficiency, as they use both electric and magnetic fields for deflecting the beam. However, the voltage used in stripline kickers is typically lower (up to 50 kV) due to pulsed power supply problems. Nevertheless, stripline kickers are much faster. These devices can handle rise and fall times of only a few ns, three orders of magnitude lower than electrostatic kickers. In contrast, they are harder to manufacture, consume much more power and flat-top stability is a challenging concern [31].

2.4 Kicker Systems for Future Linear Colliders

The injection and extraction kicker systems are one of the most critical issues for ILC and CLIC DRs. For injecion or extraction in DRs, single-turn injection is used, in which bunches are injected on-axis into empty RF buckets, and single turn-extraction is also required. Fast kickers are used to deflect the trajectories of incoming or outgoing bunches, without disturbing the stored bunches. It is extremely important that the deflection given by the kicker has a very small pulse fluctuation or jitter. Any ripple on the extraction kicker pulse produces beam size jitter which could be propagated up to the collider IP. On the other hand, jitter on the injection kicker reduces the beam stay clear during the injection process. Usually, kickers have a jitter tolerance of 10% of the beam size, although the injection jitter could be larger. The relative deflection stability requirement is [19]:

$$\frac{\delta\theta}{\theta} \leq \frac{\sigma_{jit}}{x_{sep}} = \frac{0.1\sigma_x}{x_{sep}} \tag{2.8}$$

where σ_{jit} is the jitter tolerance and σ_x is the horizontal beam size at extraction. Using typical parameters for a linear collider DR, the relative jitter tolerance for the kicker, $\delta\theta/\theta$, is on the order of a few 10^{-4}.

2.4.1 ILC Kickers

Several kicker systems will be required in many stages of the ILC. In each DR, two kickers with challenging rise and fall times will be required for bunch-by-bunch injection and extraction. Furthermore, fast bunch-by-bunch feedback systems based on kicker technology will also be required in the DRs to reduce coupled-bunch instabilities arising from long-range wakefields, which can cause bunch jitter and emittance growth. Other feedback and feedforward kicker systems will be required at the exit of the main linacs and the BDS. Just before the IP, two stripline kickers will correct the beam offset and angle. In addition, several kickers will be used as a beam abort system, extracting the beam into dumps. These kicker systems will be located at the end of each main linac and at the entrance to the BDS on the positron linac [2].

Injection and Extraction Kickers for ILC Damping Rings

The ILC DRs injection and extraction kickers act as the bunch-by-bunch beam manipulator to compress and decompress the bunch spacing into and from the DR. For the ILC baseline parameters, the bunch spacing is ~ 8 ns, which sets the limit for the rise and fall time for the injection and extraction kicker systems.

The injection and extraction are performed simultaneously to reduce variations in beam loading, but the injection kicker starts to pulse a few turns after the beginning of the extraction. Thus, injected bunches fill the gaps left by extracted bunches in the same order as the bunches were extracted. Individual bunch injection is required to change the bunch spacing and on-axis injection is required to allow the injection of a beam with a large emittance. On the other hand, individual bunch extraction must preserve low emittance, which means that the extraction does not use a closed orbit bump as is usual for beam extraction. The kicker parameters are given in Table 2.1.

The kickers require high bunch repetition rate, 3MHz for the nominal configuration and 6 MHz for the proposed luminosity upgrade, and very fast rise and fall times of the kicker field, 6 ns and 3 ns, respectively. The tolerance on horizontal beam jitter of the extracted beam is around 10% of the beam size, which requires the relative stability of the extraction kicker amplitude to be below 7×10^{-4}. To achieve these parameters, no conventional kicker magnets could be used. Two prototypes were proposed, using stripline kicker technology, and are explained in the following.

Kicker parameters	**ILC DR**		**[Unit]**
	Nominal Luminosity	High Luminosity	
Beam energy, E	5		[GeV]
Deflection angle, α	0.6 (extr) - 0.7 (inj)		[mrad]
Field rise and fall time	6	3	[ns]
Pulse flat top	~ 4		[ns]
Flat top reproducibility	$\pm 1 \times 10^{-3}$		
Injection stability	7×10^{-4}		
Extraction stability	7×10^{-4}		
Repetition rate, f_{rep}	5		[Hz]
Bunch repetition rate	3	6	[MHz]

Table 2.1: Extraction kicker specifications for the ILC DRs [2].

ILC-like multi-bunch extraction at ATF. The ATF facility at KEK, in Tsukuba, is a test facility operating at a beam energy of 1.3 GeV, mainly focused on the demonstration of the small emittances needed for future linear colliders. ATF has the same configuration as the ILC electron injector, and consists of an electron gun, a linac, and a DR [9]. Nowadays, the beam can be extracted from the DR to the ATF2 facility, which was constructed to address two major challenges of ILC: focusing the beams to nanometer scale using an ILC-like final focus system and providing nanometer stability. The two ATF2 goals, first one being achievement of 35nm beam size, and second being achievement of nanometer scale beam stability at IP, are being addressed sequentially [13].

The study of the extraction kicker from ILC DRs was carried out in ATF. The stripline kicker consists of multiple units of stripline electrodes, to improve the rise and fall time, and very fast pulse power supplies. Each of these units of stripline electrodes has a length of 30 cm. The characteristic impedance of the striplines is 49 Ω in the operation mode of the kicker, and a field homogeneity of 0.07% in a 1.8 mm radius at the center of the striplines was achieved using flat electrodes with curved edges, as shown in Fig. 2.9.

A beam test of a single unit was carried out at the ATF DR. The development was focused on realizing rise and fall times of less than 3 ns of the kick field, because this is the most difficult issue. The bunch repetition rate of the fast pulse power supply is 3 MHz, whereas the specification of the ILC bunch repetition rate is 6 MHz for the luminosity upgrade. In this beam test, a rise and fall time of 3 ns was demonstrated [34]. In order to achieve the repetition rate of 6 MHz, an ILC-type beam-extraction experiment using two stripline kickers was also carried out [29]. The complete length of the two striplines was 60 cm and the aperture was 9 mm and 11 mm for each kicker. Two pairs of pulsers with a peak amplitude of ±5 kV, a rise time of 1.5 ns and a bunch repetition rate of 3.3 MHz were used to drive the striplines. The stripline kicker system

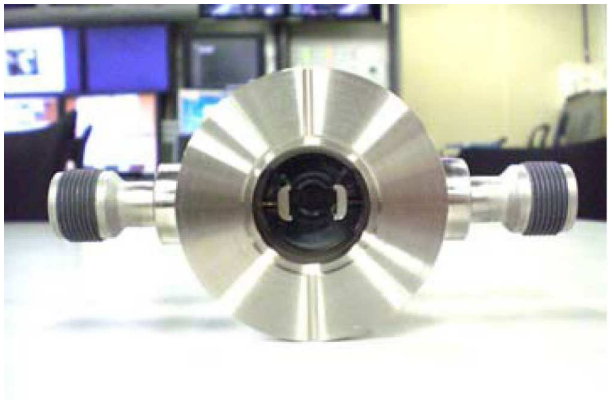

Figure 2.9: ATF stripline kicker prototype for multi-bunch extraction [29].

produced a 3 mrad total kick angle for a 1.3 GeV beam. The multi-bunch beam stored in the DR with 5.6 ns bunch separation was successfully extracted, with a 3 mrad total kick angle and 308 ns bunch spacing in the extraction line. No deterioration of the extracted vertical beam size was observed, as measured with the laser wire. The relative angle jitter of the single-bunch beam extraction was 3.5×10^{-4} r.m.s., which is better than the requirements for ILC DR extraction. For beam injection and extraction in the ILC DRs, 42 units of striplines with 30 cm length each will be required.

Stripline kicker design for beam injection at DAΦNE. The Φ-factory DAΦNE, at the Laboratori Nazionali di Frascati (LNF), is a circular e^+e^- collider operating with a center-of-mass energy of 1.02 GeV, mainly for studies of Charge Parity (CP) violation. The collider complex consists of an injection system composed of a linac, an accumulator ring and transfer lines from the linac to the accumulator and from the accumulator to the collider. The DAΦNE collider is based on two independent rings having two common Interaction Regions (IR) [35].

The design of the new, fast stripline kickers for the injection upgrade of DAΦNE, shown in Fig. 2.10, is based on stripline tapering to obtain a device with low beam impedance, and an excellent uniformity of the deflecting field in the transverse plane, as required for the ILC kickers.

The striplines electrodes must be driven at ± 45 kV for a 5 mrad deflection angle, and the deflecting field has rise and fall times of less than 6 ns, which corresponds to the nominal rise and fall times required for the ILC DRs kickers. Therefore, the experience gained with the new DAΦNE injection system will be applied to the design of the ILC DR injection system. The DAΦNE injection kicker has an effective length of about 0.85 m, and an aperture at the centre of the striplines of 54.8 mm. The characteristic impedance have been matched to 50 Ω in the kicker operating mode, and the inhomogeneity of the deflecting field as a function of the horizontal coordinate is of the order of 2% over all the kicker horizontal aperture, while it is less than 10% over 1 cm along the vertical coordinate. This uniformity has been achieved by optimizing

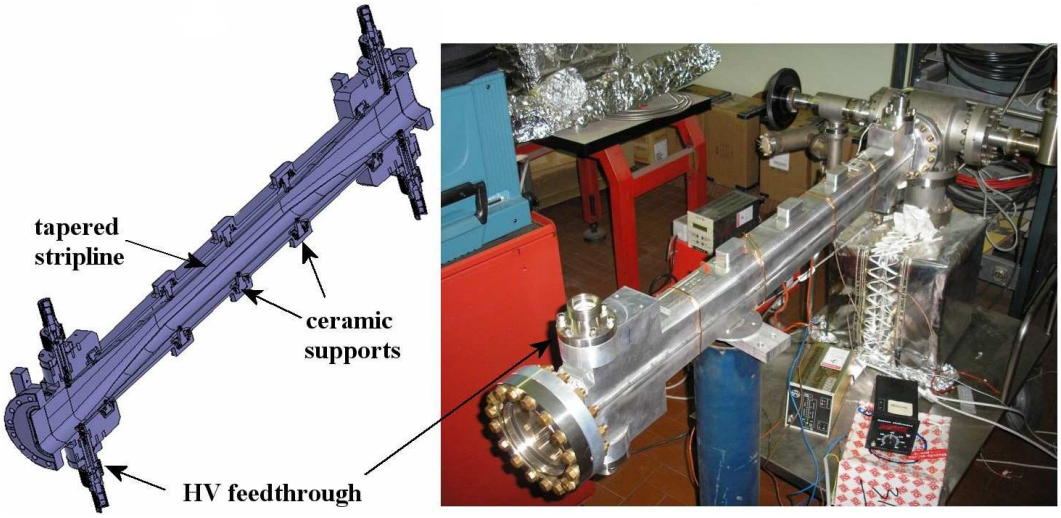

Figure 2.10: DAΦNE stripline kicker [19].

the curved and tapered electrodes [36]. The coupling impedance measurements and simulations have pointed out the absence of trapped HOMs in the longitudinal and horizontal planes when at least two ports are loaded by 50 Ω [37]. In the vertical plane, only four trapped HOMs were found. The instability growth rates of these resonances, in the worst case, were well below the damping rates provided by the DAΦNE feedback systems. After installing the injection system, no instability effects due to the kickers were observed and the DAΦNE broadband impedance arising from this and other vacuum chamber modifications made at the same time was reduced by about 50% [38].

2.4.2 CLIC Kickers

A number of challenging kicker systems are required for both the Main Beam and Drive Beam of CLIC, as shown in Fig. 2.11. For the Main Beam, one injection and one extraction kicker are required for each PDR and DR, as well as a kicker in the IP, to correct relative beam-beam offset and steer the beams back into collision. For the Drive Beam, extraction kicker systems are required for the CRs, whereas the injection is done by an RF deflector instead of a kicker. Furthermore, a number of turn-around kickers, to reduce beam phase jitter, and loop phase compensation kickers, to synchronize the phase between the Drive Beam and the Main Beam, will also be required [19].

Extraction Kicker from the CTF3 CR

The Drive Beam Accelerator of CLIC accelerates long bunch trains of 140 ns with a repetition frequency of 500 MHz and an average beam current of 4.2 A. Finally the repetition frequency has to be 12 GHz and the beam current 101 A. The final values

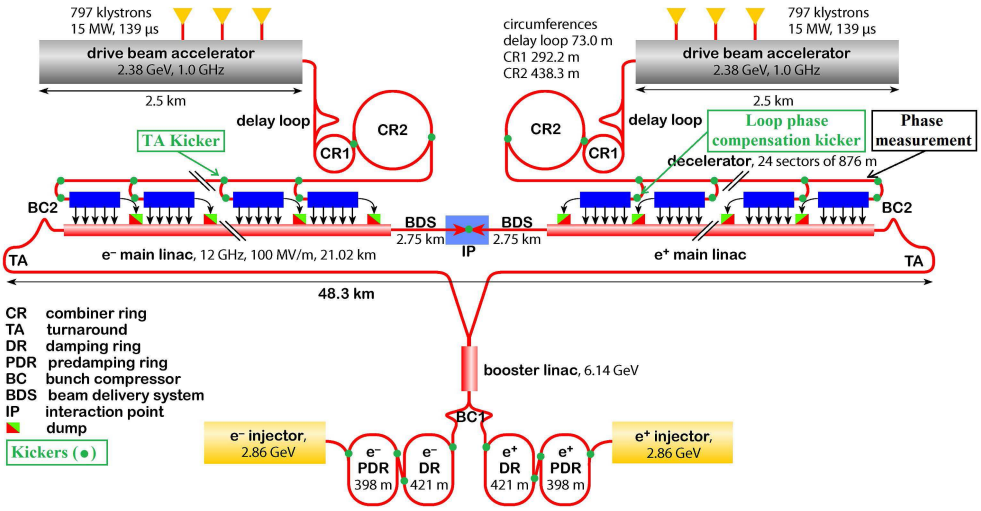

Figure 2.11: General layout of CLIC, with kickers pointed out in green [19].

are achieved combining different incoming bunch trains by means of a delay loop and two CRs [19].

CTF3 is meant to demonstrate the principle of the RF power source and to provide the 12 GHz RF required. One of the most important issues to be tested in CTF3 is the frequency multiplication by the novel bunch interleaving technique. In CTF3, a long train of bunches with a bunch spacing of 20 cm, is converted into a series of short bunch trains of 2 cm bunch spacing. This bunch spacing reduction is done in two stages, first is reduced by a factor of two in a delay loop, and then by a factor of four in a CR. After being extracted from the CR, the individual bunches are compressed in a magnetic bunch compressor and transported to an experimental area to produce the 12 GHz RF power required for two-beam studies. The specifications for the existing CTF3 CR extraction kicker as well as for the CLIC CRs are summarized in Table 2.2.

Kicker parameters	**CTF3 CRs**	**CLIC CRs**	**[Unit]**
Beam energy, E	300	2380	[MeV]
Deflection angle, α	8	2.5	[mrad]
Aperture, a	40	20	[mm]
Effective length, L	1.7	3	[m]
Field rise and fall time	70	150	[ns]
Pulse flat top	200	450	[ns]
Flat top reproducibility	$\pm 1\times10^{-3}$		
Extraction stability	$\pm 2.5\times10^{-3}$		
Repetition rate, f_{rep}	50		[Hz]

Table 2.2: Extraction kicker specifications for the CTF3 CRs and CLIC CRs [31].

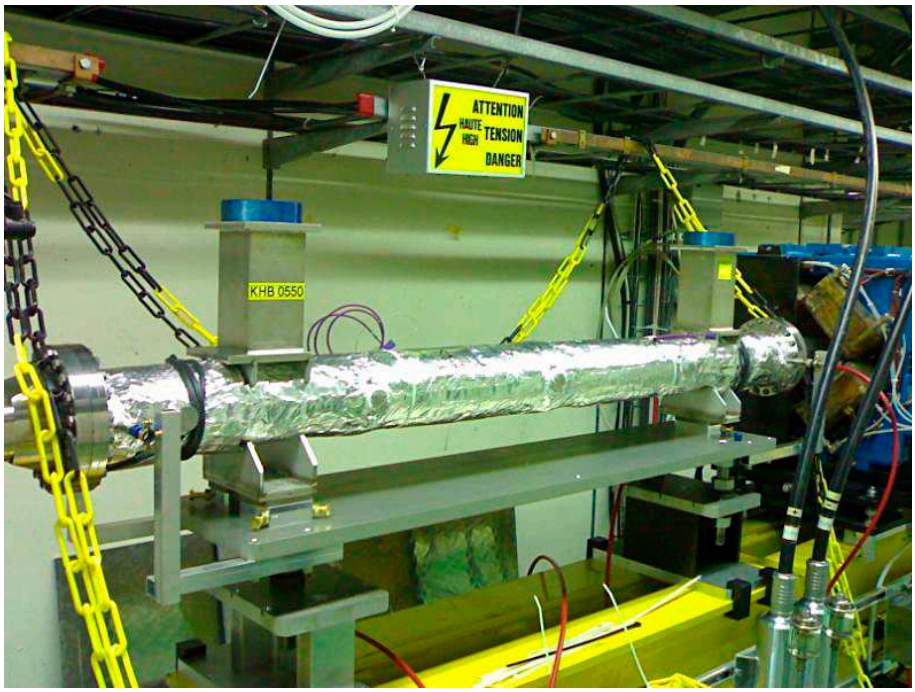

Figure 2.12: Stripline kicker installed in the CTF3 CR [31].

The extraction kicker for the CTF3 CR is shown in Fig. 2.12. This kicker has an effective length of 1.7 m, and an aperture of 40 mm. The stripline electrodes shape have been optimized in order to achieve both an optimum characteristic impedance of 50 Ω and a field homogeneity of ± 1% over 30 mm radius. The striplines horizontally extract the 140 ns and 150 MeV beam. As shown in Table 2.2, a beam energy of 300 MeV has been used for the kicker design, to be able to deflect higher energy beams for tests. The kicker pulse is required to feature a flat-top long enough to extract 140 ns of bunches. In addition, the rise time should be fast enough to reach the flat-top field after the beam exits the kicker and before it arrives again to the kicker to be extracted, and a rise time of 70 ns has been specified. This required rise time does not justify the selection of stripline technology, as kicker magnets could be also well fitted. However, the beam impedance requirements made the stripline technology the ideal solution for extracting the CTF3 high current beams [31]. The kicker was installed at the exit of the CTF3 CR in mid-2008 and is successfully working since then.

Injection and Extraction Kickers from CLIC PDRs and DRs

The injection and extraction process will be carried out using one injection and one extraction system in each ring, with only one pulse stored in the rings per cycle. This pulse contains either one single train of 312 bunches with 2 GHz RF structure, or two trains of 156 bunches with 1 GHz RF structure, as shown in Table 1.4 and Table 1.5. The kickers are located at a maximum of the horizontal beta function to minimize

the deflection angle. For the same reason, the phase advance between injection or extraction septa and kickers is around $\pi/2$.

Kicker parameters	**PDR**		**DR**		**[Unit]**
	1 GHz	2 GHz	1 GHz	2 GHz	
Beam energy, E	2.86		2.86		[GeV]
Deflection angle, α	2		1.5		[mrad]
Aperture, a	40		20		[mm]
Effective length, L	3.4		1.7		[m]
Field rise and fall time	428	1000	560	1000	[ns]
Pulse flat top	900	160	900	160	[ns]
Flat top reproducibility	$\pm1\times10^{-4}$		$\pm1\times10^{-4}$		
Injection stability	$\pm2\times10^{-2}$		$\pm2\times10^{-3}$		
Extraction stability	$\pm2\times10^{-3}$		$\pm2\times10^{-4}$		
Injection uniformity (%)	±0.1 (over 3.5 mm radius)		±0.1 (over 3.5 mm radius)		
Extraction uniformity (%)	±0.1 (over 3.5 mm radius)		±0.01 (over 1 mm radius)		
Repetition rate, f_{rep}	50		50		[Hz]

Table 2.3: Kicker specifications for the DRs [19].

In the DRs, the quadrupole magnets have a circular aperture of 20 mm diameter, and the dipoles and wigglers have an elliptical aperture with vertical gaps of 20 and 13 mm, respectively. To minimize the impact of the DR extraction kicker on the overall machine beam coupling impedance, the same beam pipe cross-section is used as for the downstream quadrupoles. For that reason, a circular aperture of 20 mm diameter was selected for the aperture of the striplines of the CLIC DRs extraction kicker. For the PDRs, the striplines aperture needs to be larger, 40 mm, in order to accept larger emittance beams, as shown in Table 1.4.

The complete beam pulse will be extracted at the same time. Therefore, the flat top corresponds to the length of the bunch train for the 2 GHz baseline, or the length of the two bunch trains plus the train separation for the 1 GHz baseline. In order to limit the beam emittance blow-up due to oscillations at extraction the combined flat top ripple and droop of the field pulse for the DR extraction kickers must be less than 0.02%. In the case of PDRs, the injection and extraction stabilities required are lower than for the DRs, due to the larger emittances of the injected and extracted beams.

The total allowable beam coupling impedance in each ring is also very low. The allowable broad band impedances in the CLIC PDRs and DRs are 1 Ω/n, where n is the number of turns, for longitudinal beam coupling impedance, and 10 MΩ/m in the transverse plane. These requirements will guarantee the beam stability against single bunch effects [21]. Since the allowable beam impedance is for a complete ring, which is composed of many systems including both injection and extraction kicker systems,

the permissible beam coupling impedances, per kicker system, are assumed to be 5% of the longitudinal impedance allowance, i.e. 0.05 Ω/*n*, and 2% of the transverse impedance allowance, i.e. 200 kΩ/m [39].

2.4.3 Technological Choice of the Extraction Kicker for CLIC DRs

This thesis is based on the design, development, construction and lab measurements of the first extraction kicker prototype for the CLIC DRs, since it is the most challenging from the field homogeneity point of view, as shown in Table 2.3. The very tight stability tolerances required in order to extract the low emittance beam from the CLIC DRs, as well as the low beam coupling impedance requirements, make the stripline technology an ideal solution for extracting high current beams, as it was also the case for the CTF3 CR extraction kicker [31]. The geometry of the CTF3 CR extraction kicker, which has the same stripline length but larger aperture (40 mm instead of 20 mm), was first studied for the CLIC DR extraction kicker, though not all the specifications were met. Furthermore, several challenges were identified that made it impossible to reuse the designs for the ILC injection and extraction kickers previously reported:

- The curved and tapered electrodes used in DAΦNE would give higher field inhomogeneity than is permissible for the CLIC DRs. In addition, tapering has been demonstrated to increase the beam coupling impedance at very low frequencies, and this is undesirable for CLIC.

- The 30 cm-long stripline kicker for extracting the beam in ATF, with a beam energy of 1.3 GeV, could not be feasible for deflecting the CLIC beam with an energy of 2.86 GeV by the specified 1.5 mrad. Furthermore, for this kicker the field homogeneity is approximately three times larger than the required for CLIC DRs.

- The CLIC DR extraction will not be bunch-by-bunch, but a complete train of 156 (1 GHz) or 312 (2 GHz) bunches will be extracted at the same time; hence the required rise time for the CLIC DR kickers is two orders of magnitude larger than the DAΦNE injection kicker and the ILC DR extraction kicker.

In addition, the design of all these kickers was optimized for the operating mode of the kicker (odd mode), whereas the non-operating mode of the kicker (even mode) was not taken into account.

In the following we will make a complete study of the design, manufacturing and calibration tests of the first stripline prototype for extracting the beam from the CLIC DRs. The design of the striplines, presented in Chapter 3, have been done under a collaboration between the Accelerators Group of the Instituto de Física Corpuscular (IFIC) [40], the Accelerators Technology Group of the Technology Department of the Centro de Investigaciones Energéticas, Medioambientales y Tecnológicas

(CIEMAT) [41], and the Accelerator Beam Transfer (ABT) Group of the Technology (TE) Department at CERN. The striplines manufacturing has been funded by the Centro para el Desarrollo Tecnológico Industrial (CDTI) [42], a Spanish public entity that supports the industrial research of the Spanish companies, under a collaborative scheme with research institutes. In this framework, the company Trinos Vacuum Projects S.L. [43] has been in charge of the striplines manufacturing, under a CDTI contract [44]. Studies of the materials and components for the kicker fabrication, as well as manufacturing details, are reported in Chapter 4. The laboratory tests required to characterize the electromagnetic response of the striplines, have been carried out at CERN, and the results are presented in Chapter 5. Finally, in Chapter 6, studies towards improvement of future striplines are discussed.

Chapter 3

Design and Optimization of the Striplines

3.1 Introduction

Low emittance rings demand very tight tolerances for the injection and extraction systems, in order to inject and extract the beam in a very stable and reproducible way. The most challenging requirements are an excellent field uniformity at the beam position and a very low beam coupling impedance. In this chapter, the main techniques for the design of a stripline kicker for low emittance rings are proposed. In particular, the study will be focused on the specifications for the extraction kicker from CLIC DRs, but the method can be generalized to any low emittance ring kicker.

The requirements for the extraction kicker from CLIC DRs are collected in Table 2.3. The most important challenges are the following: first, the excellent field homogeneity, with only ± 0.01% of inhomogeneity allowed over 1 mm radius, in the centre of the aperture; second, good power transmission, with extremely low ripple, by achieving good impedance matching of the striplines in the deflecting (odd) mode; and third, a very low beam coupling impedance, which should be below 0.05 Ω/n, where n is the number of turns, in the longitudinal plane and 200 kΩ/m in the transverse plane: the beam coupling impedance is important during both the deflecting and non-deflecting (even) mode. In order to achieve all these requirements, the design of the striplines has to be carefully optimized. This study has been done in several steps, both analytically and numerically, from 2D concepts such as characteristic impedance, field homogeneity and RF breakdown, to 3D studies for the reflection parameter and beam coupling impedance at low frequencies. Finally, other calculations at high frequencies are reported.

3.2 Description of a Stripline Kicker System

A stripline kicker consists of two parallel electrodes housed in a conducting pipe: each of the electrodes is driven by an equal but opposite polarity pulse, produced by a pulsed power supply. The striplines will be powered, via coaxial feedthroughs, from the beam exit end: the upstream feedthroughs will be connected to resistive loads, as shown in Fig. 2.8. Each of the stripline electrodes with its adjacent ground planes (beam pipe walls) forms a transmission line for TEM waves. Besides the two transmission lines, a stripline kicker system is composed by a High Voltage (HV) DC power supply and two terminating loads, as schematically shown in Fig. 3.1, for only one of the two transmission lines. The HV DC power supply charges a Pulse Forming Line (PFL) and the fast switch is then closed to launch a pulse towards the striplines. The pulse propagates through the striplines and is deposited in the terminating loads.

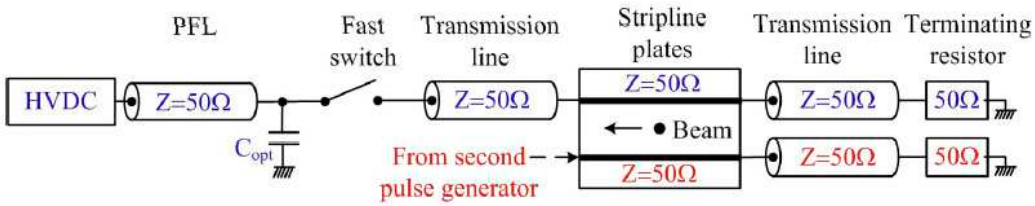

Figure 3.1: Simplified schematic of a stripline kicker system. For simplicity, only one of the two HV DC supplies, PFL and fast switches is shown [19].

A transmission line is schematically represented as a two-wire line, as shown in Fig. 3.2 (a), since transmission lines for TEM wave propagation always have at least two conductors. Furthermore, a transmission line can be modelled as a distributed-parameter network when the length of the line is larger than the wavelength. In this case, voltages and currents can vary in magnitude and phase over its length, as shown in Fig. 3.2 (b), where R, L, G and C are defined per unit length. The series inductance L represents the total self-inductance of the two conductors, and its proximity gives rise to a shunt capacitance C. The series resistance R and the shunt conductance G represent the resistance due to the finite conductivity, and the dielectric loss in the material between the conductors, respectively. In addition, $i(z,t)$ and $v(z,t)$ represents the current and voltage applied to the transmission line.

The voltages and currents of a transmission line can be described by two coupled linear differential equations, known as the telegrapher's equations, and represents the time-domain form of the transmission line [45]:

$$\frac{\partial v(z,t)}{\partial z} = -Ri(z,t) - L\frac{\partial i(z,t)}{\partial t} \tag{3.1}$$

$$\frac{\partial i(z,t)}{\partial z} = -Gv(z,t) - C\frac{\partial v(z,t)}{\partial t} \tag{3.2}$$

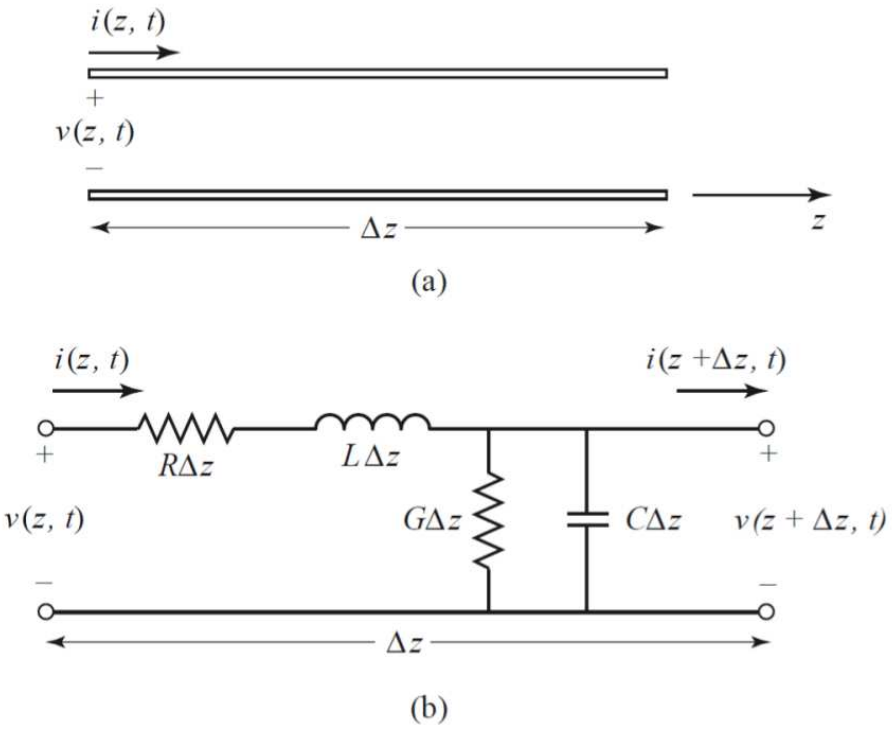

Figure 3.2: (a) Two-wire representation of a transmission line, (b) distributed-parameter network model for a transmission line [45].

where R, L, G, C, $i(z,t)$ and $v(z,t)$ have been defined before. In the frequency domain, these transmission line equations simplify to

$$\frac{dV(z,\omega)}{dz} = -(R + j\omega L)I(z,\omega) \tag{3.3}$$

$$\frac{dI(z,\omega)}{dz} = -(G + j\omega C)V(z,\omega) \tag{3.4}$$

where $V(z,\omega)$ and $I(z,\omega)$ represents the voltage and current applied to the transmission line in frequency domain, j is the imaginary unit $j^2 = -1$ and ω is the angular frequency.

The stripline kicker operates as two coupled transmission lines, each of which should ideally have a characteristic impedance matched to 50 Ω. The characteristic impedances of the PFL, transmission lines, striplines and terminating resistors are matched as far as possible to minimize reflections, which could cause ripple on the flat-top of the deflection waveform. The PFL and fast switch, shown in Fig. 3.1, can be replaced with an inductive adder, as in the case of the kicker systems for CLIC DRs [46]. An inductive adder is a solid-state modulator, which can provide relatively

short and precise pulses, compensating for ripple as well as attenuation and dispersion in transmission lines. The inductive adder concept is also good for machine protection and reliability. The first inductive adder prototype for the extraction kicker system from CLIC DRs is shown in Fig. 3.3.

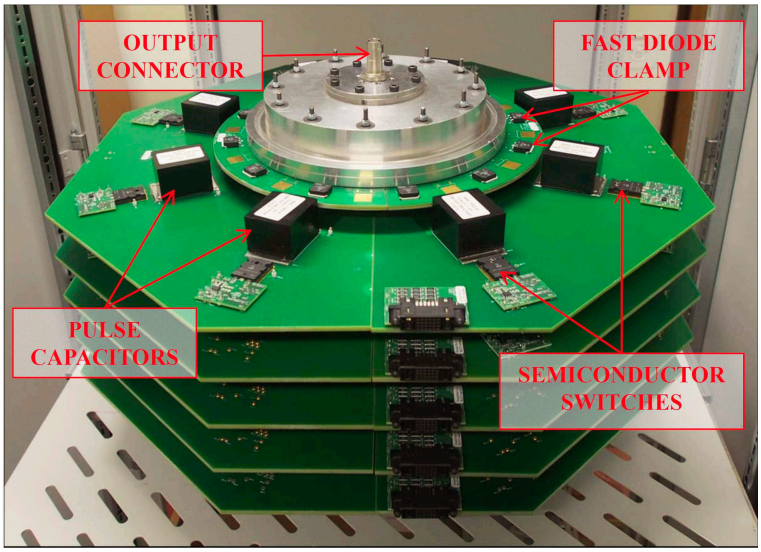

Figure 3.3: Five-layer inductive adder prototye developed at CERN, for CLIC DRs beam extraction system [46].

The main pulse definitions are shown in Fig. 3.4. The rise time is the time needed to reach the required field, including the settling time, which is the time needed to damp oscillations to within specification. The fall time is the time required for the field to return to zero. The droop and ripple is defined as the time window during which the combined droop and ripple must be also within specification. And the pulse reproducibility refers to the maximum difference allowed between two consecutive pulses.

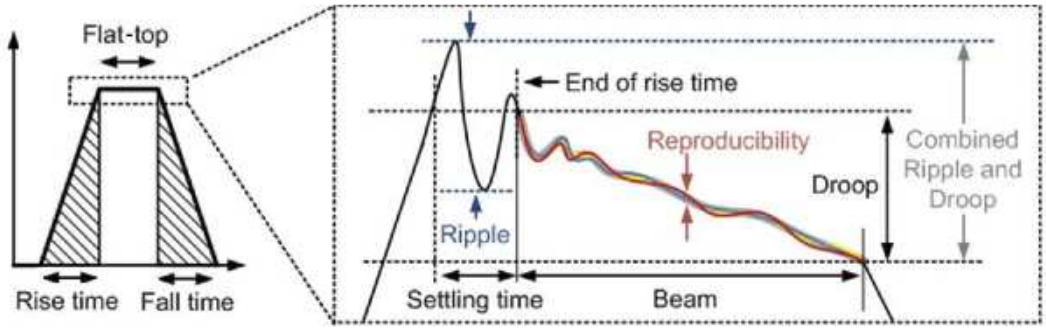

Figure 3.4: Definitions for the pulse required for beam extraction from CLIC DRs [47].

The pulse parameters are based on beam characteristics and kicker requirements. For example, for bunch-by-bunch injection or extraction, as for the ILC DRs, fast rise and fall times are required, whereas for injecting or extracting a number of trains of bunches, it is more important to have a long pulse flat-top with very good stability, which is the case of injection and extraction for CLIC DRs. To limit the beam emittance blow-up due to oscillations, the inductive adder for the CLIC DR kickers must provide extremely flat HV pulses: specifications call for a 160 ns duration flat-top for a pulse of 12.5 kV, with a combined ripple and droop of not more than 0.02%, as shown in Table 2.3, referred to as extraction stability.

All the power transmitted by the pulse has to be dissipated by using two dissipation loads, connected to the upstream ports of the striplines, as shown in Fig. 2.8. The loads should be matched in impedance with the kicker and the power supply to avoid pulse reflected power. The load must also be designed to handle the frequency content of the pulse, keeping a good impedance match at all the pulse frequency range. When dealing with pulsed signals, the highest frequency (in GHz) content can be roughly determined by the rise time T_r (in ns) of the pulse, as $1/T_r$ [31]. In the case of the CLIC DRs, although a rise time of 560 ns (1 GHz baseline) and 1 μs (2 GHz baseline) is allowed, as shown in Table 2.3, a rise time of approximately 100 ns (including settling time) is desired, in order to reduce the stress on the kicker system [47]. A rise time of 100 ns corresponds to a frequency content up to 10 MHz.

3.3 Stripline Kicker Basics

The striplines performance is completely defined by a number of parameters that will impose some restrictions on the striplines design, which are the following: the characteristic impedance, field homogeneity, RF breakdown, S-parameters and longitudinal and transverse beam coupling impedance. All these parameters will be described in this section.

3.3.1 Characteristic Impedance

The characteristic impedance of a transmission line Z_0 is defined as the ratio of voltage to current for a traveling wave on a transmission line. Solving simultaneously Eq. (3.3) and Eq. (3.4), the voltage and current along the transmission line can be calculated, and the characteristic impedance is found to be:

$$Z_0 = \frac{V}{I} = \sqrt{\frac{R + j\omega L}{G + j\omega C}} \tag{3.5}$$

Since voltage and current are uniquely defined for TEM waves, the characteristic impedance of a TEM wave is unique. For a lossless line, R and G are both zero, so the equation for the characteristic impedance reduces to:

$$Z_0 = \sqrt{\frac{L}{C}} \tag{3.6}$$

In addition, in a lossless transmission line, the TEM wave propagates at the speed of the light c, which can be related with the line parameters:

$$c = \frac{1}{\sqrt{LC}} \tag{3.7}$$

and therefore:

$$Z_0 = \frac{1}{cC} \tag{3.8}$$

The characteristic impedance of a lossless transmission line is purely real, with no reactive component. When using air or vacuum as dielectric between the two conductors, the characteristic impedance is a geometrical parameter, only depending on the cross section of the transmission line by means of the capacitance per unit length C. Eq. (3.8) can be analytically solved for simple geometries like a coaxial line or parallel plates. However, in non analytical cases, it is necessary to obtain the full solution of the electromagnetic field using numerical methods.

When two transmission lines are close together, as in the case of a stripline kicker, power can be coupled between the lines due to the interaction of the electromagnetic fields of each line. Therefore, stripline kickers operate as two coupled transmission lines, with two TEM operating modes, since three conductors are involved in the signal transmission, i.e. both electrodes and the vacuum beam pipe. These modes are known as odd and even mode [45]. When the electrodes are excited with equal magnitude but opposite polarity voltages, the current flow is in opposite directions in each stripline electrode and an electromagnetic field is created between the electrodes, giving a transverse kick to the beam: this is the odd mode. When unkicked circulating beam passes through the aperture of the striplines, it induces image currents in the electrodes with the same direction –this is the even mode. The induced current generates an electromagnetic field, which gives a longitudinal kick to the beam and can produce beam instabilities.

In the case of the stripline kicker, both operation modes must be taken into account when optimizing the characteristic impedance of the striplines. For the odd mode, the electric field lines have an odd symmetry about the centre line, and a null voltage exists between the two electrodes. Hence, there is a virtual ground plane midway between the electrodes and the capacitance between an electrode and the virtual ground is $2C_{12}$. In this case, the effective capacitance between an electrode and ground is $C_{odd} = C_{11} + 2C_{12}$ (Fig. 3.5, up). In the even mode, since the two electrodes are at the same effective potential, there is no charge stored in the capacitance between them, and the resulting capacitance of either electrode to ground for the even mode is $C_{even} = C_{11}$ (Fig. 3.5, down).

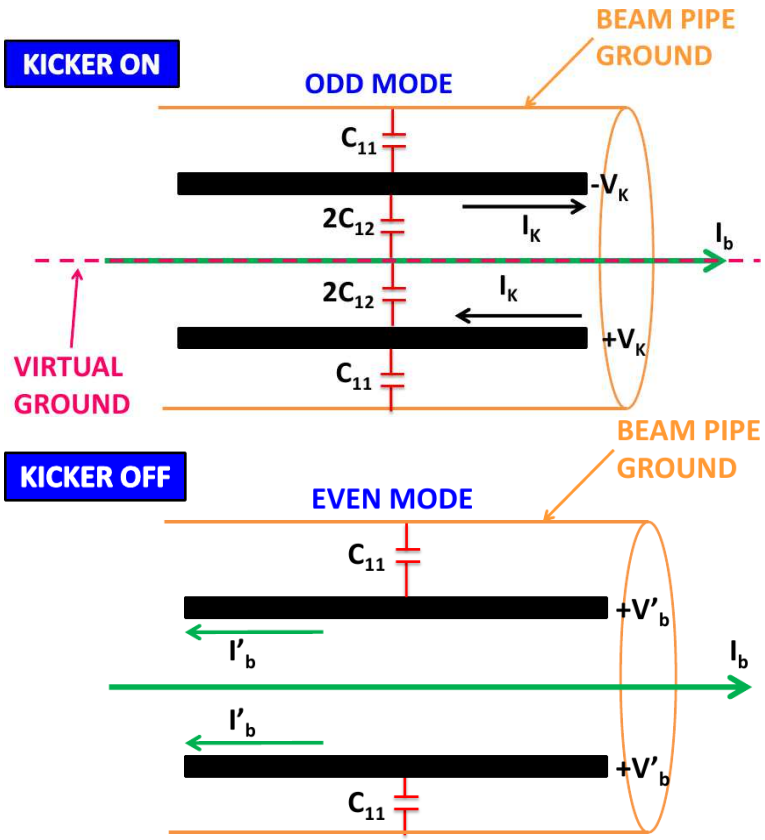

Figure 3.5: Scheme of the two operation modes of a pair of coupled electrodes: odd mode (up) and even mode (down). For the even mode, I'_b and V'_b corresponds to the image current and voltage created by the beam when passing through the aperture of the striplines.

The uncoupled impedance Z_0 is defined as the impedance one would measure if the electrodes were widely separated, so they could not interact. The odd mode impedance of a coupled transmission line is always less than the uncoupled impedance, whereas the even mode impedance is always greater. The smaller the distance between the two electrodes, the more coupling will be induced, and the greater is the discrepancy between the odd mode, uncoupled mode and even mode impedances. This even-odd mode decomposition can be carried out only in the case of identical lines both of which have the same load and generator impedances, which is the case of the striplines for CLIC DRs.

The odd and even mode characteristic impedances for the striplines can be analytically calculated using the following equations:

$$Z_{odd} = \frac{1}{c(C_{11} + 2C_{12})} \tag{3.9}$$

$$Z_{even} = \frac{1}{cC_{11}} \tag{3.10}$$

where c is the speed of light, C_{11} is the capacitance between an electrode and the beam pipe surrounding, and C_{12} is the capacitance between both electrodes, as shown in Fig. 3.5. For a first-order analytical approximation, C_{11} can be calculated as the capacitance between a strip conductor and an infinite ground plane, as shown in Fig. 3.6 (up), by using Eq. (3.11) [48]:

$$C_{11} = \frac{\sqrt{\epsilon_r + 1.41}}{87c}\left(ln\left(\frac{5.98\,d}{0.8\,h + w}\right)\right)^{-1} \tag{3.11}$$

where $\epsilon_r = 1$ is the relative permittivity of the vacuum, d is the distance between the plate and the ground plane, i.e. the distance between the electrode and the beam pipe wall behind, h is the electrode height and w is the electrode thickness.

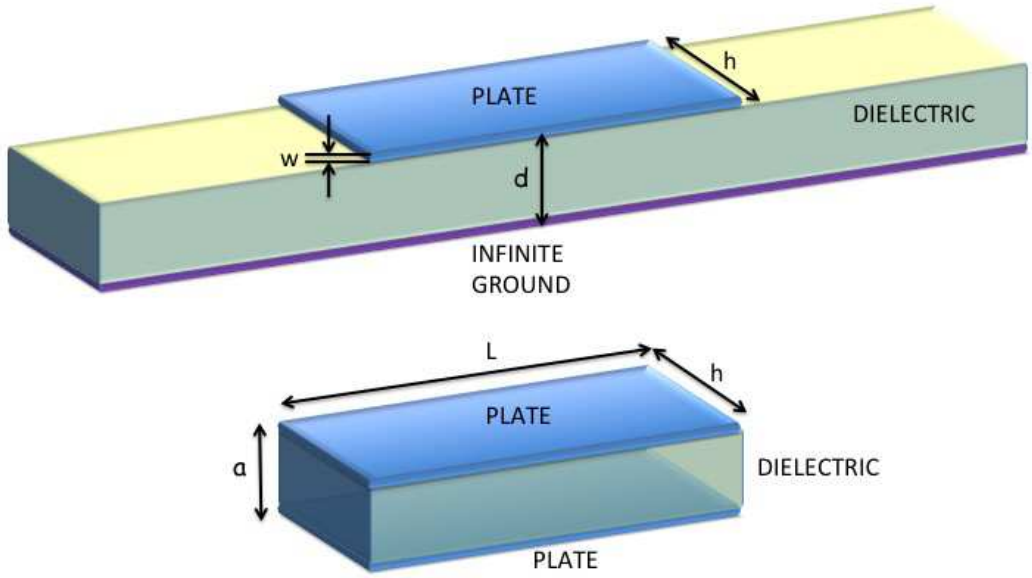

Figure 3.6: Schematic of a strip conductor separated from a ground plane by a dielectric (up) and schematic of a parallel plate capacitor (down).

To a first approximation the electrodes can be considered as parallel plate capacitors where edge effects and fringe fields are neglected, as shown in Fig. 3.6 (down). Therefore, C_{12} can be calculated as the capacitance of a parallel plate per unit length, given by the equation:

$$C_{12} = \frac{\epsilon_0 A/L}{a} = \frac{\epsilon_0 h}{a} \tag{3.12}$$

where $\epsilon_0 = 8.854 \times 10^{-12} F/m$ is the permittivity of free-space, A is the surface area of one plate, L is the plate length, h is the plate height, and a is the distance between

plates, i.e. the aperture. Taking into account these approximations, the equations considered for calculating Z_{odd} and Z_{even} are the following:

$$Z_{odd} = ln\left(\frac{5.98(d/R)}{0.8(h/R)+(w/R)}\right)\left(\frac{\sqrt{\epsilon_r+1.41}}{87}+\frac{2c\epsilon_0 h}{a}ln\left(\frac{5.98(d/R)}{0.8(h/R)+(w/R)}\right)\right)^{-1} \quad (3.13)$$

$$Z_{even} = \frac{87}{\sqrt{\epsilon_r+1.41}}ln\left(\frac{5.98(d/R)}{0.8(h/R)+(w/R)}\right) \quad (3.14)$$

where R is the striplines beam pipe radius.

3.3.2 Field Homogeneity

The concept of field homogeneity refers to the uniformity of the dipolar fields in the striplines aperture. It mainly depends on the geometry of the electrodes. For example, two parallel plates of a capacitor generate a perfect unidirectional electric field between them except from the end effects. Those end effects distort the pure unidirectional field in the space between the plates, with more impact close to the ends. The same happens for the magnetic field in TEM propagation mode. Generally, the kicker specifications gives a value for the maximum field inhomogeneity allowed, which is calculated as a variation percentage of the unidirectional field component in an area determined by beam optics requirements. In the case of low emittance rings, an excellent field uniformity is required in order to inject and extract the beam without emittance dilution. For the CLIC DRs extraction kicker the field inhomogeneity required is unprecedented: it should not exceed the value of ± 0.01% in an area that corresponds to a circumference of 1 mm radius at the center of the striplines.

Each operation mode of the striplines, odd and even, has its own electromagnetic field pattern, as shown in Fig. 3.7. However, since the field inhomogeneity requirement refers to the field that can be seen by the beam when it is being deflected, only the odd mode field homogeneity will be studied. The study will be done numerically, since the important effect of the electrode edges over the field homogeneity can not be taken into account analytically.

3.3.3 RF Breakdown

When a current flows between two conductors at different electric potential, an electrical discharge may be produced. These electrical discharges appear in structures even though they are under ultra high vacuum conditions, where no media is hardly available for electricity conduction, if high enough electric potential difference is sustained between two points of the structure. In that particular case, the electrical discharge receives the name of vacuum arc. The accelerator community refers to the phenomenon as electric or RF breakdown. Sharp edges, by instance, can become a source of RF breakdowns.

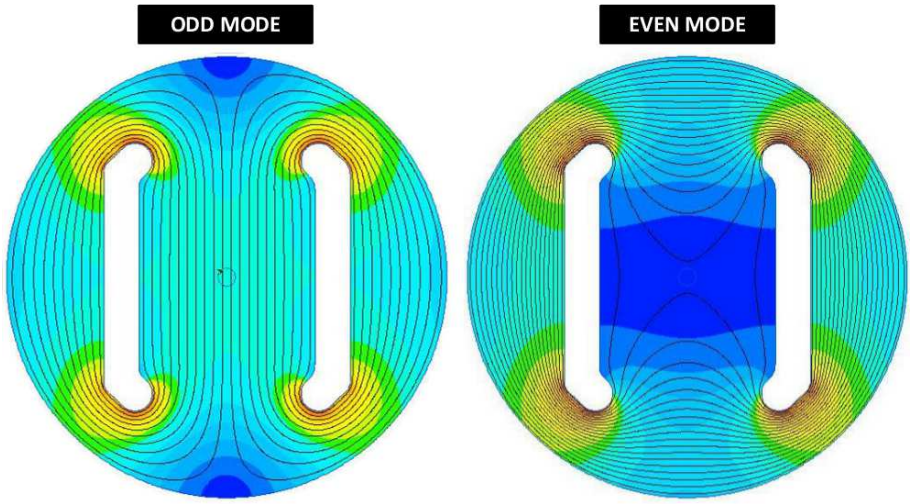

Figure 3.7: Electric field pattern for the odd (left) and even (right) modes. The colour pattern goes from orange (maximum electric field) to dark blue (minimum electric field).

The first attempt to describe quantitatively the limitation to high voltage operation came from W. D. Kilpatrick, who provided a threshold to the maximum field (E_k) beyond which the safe operation was not guaranteed [49]. The criterion was applicable to both DC and RF structures. The Kilpatrick criterion can be expressed as [50]:

$$f = 1.64 E_k^2 e^{-8.5/E_k} \tag{3.15}$$

where f is the RF frequency in MHz, and E_k is the Kilpatrick limit for the electric field, given in MV/m. The Kilpatrick criterion is based on experimental results that were obtained before clean vacuum systems were common. Many other studies had already gone beyond the threshold set by Kilpatrick, as results of improved surface treatments and clean vacuum systems [51]. Therefore, the Kilpatrick criterion is considered conservative by today's standards. Nevertheless, this criteria can still be used for choosing the design field level for the CLIC stripline kicker. For a maximum frequency content of 10 MHz, the Kilpatrick limit is set to $E_k \approx 5.5$ MV/m.

When the RF breakdown takes place on or just above the surfaces of insulators, instead of occurring within the insulating material, the breakdown effect is known as surface flashover. Several studies have been carried out at the LHC, due to the fact that during 2012 operation, a total of six kicker magnet flashovers occurred, which were thought to have been on the surface of the ceramic tube used to support the beam screen conductors [52]. In the stripline kicker for CLIC DRs, if some ceramic material is used inside the tube of the striplines or in the feedthroughs, a flashover process may be expected due to the high voltage operation of the kicker.

3.3.4 S-Parameters: Power Transmission through the Striplines

The scattering parameters (S-parameters) in RF define the transmission and reflection of voltage waves through a multi-port electrical network. For an RF signal incident on one port, some fraction of the signal bounces back out of that port, some of it scatters and exits other ports, and some of it disappears as heat or even electromagnetic radiation. S-parameters are complex because both the magnitude and phase of the input signal are changed by the network. S-parameters are defined for a given frequency and system impedance, and vary as a function of frequency for any non-ideal network.

The striplines can be considered as a simple 2-port network with an impedance Z, as it is shown in Fig. 3.8, where V_0 is the wave voltage from the generator, V_1, I_1, V_2 and I_2 are the wave voltages and currents flowing in port 1 and port 2, respectively, and Z_G and Z_L are the generator and load impedances.

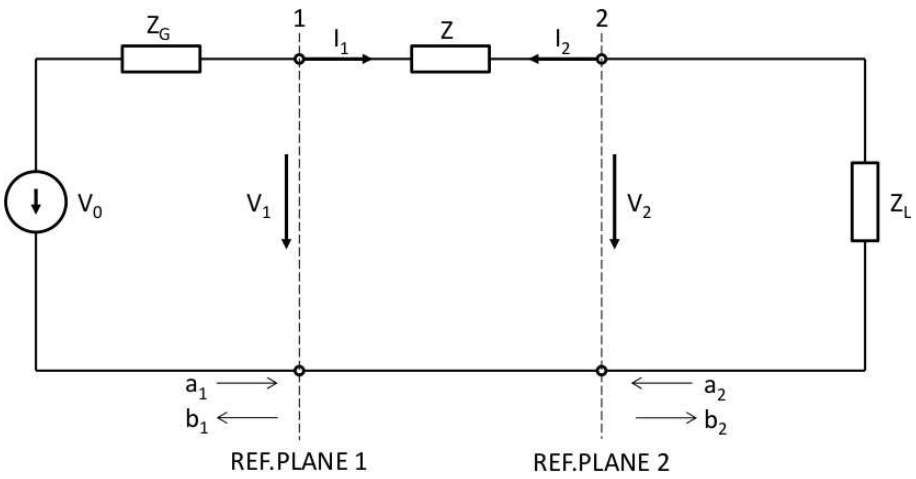

Figure 3.8: Example for a 2-port network consisting of a series impedance Z in a transmission line [53].

If $Z = 0$ and $Z_L = Z_G$, it corresponds to a match load, hence the maximum available power goes into the load and $V_1 = V_2 = V_0/2$. The waves going towards the 2-port are $a = (a_1, a_2)$, and the waves travelling away from the 2-port are $b = (b_1, b_2)$. In order to make the definitions consistent with the conservation of energy, the voltage is normalized to $\sqrt{Z_0}$, where Z_0 is the characteristic impedance of the transmission line. The definitions of the waves a_1 and b_1 are the following:

$$a_1 = \frac{V_0}{2\sqrt{Z_0}} = \frac{V_1^{inc}}{\sqrt{Z_0}} \tag{3.16}$$

$$b_1 = \frac{V_1^{ref}}{\sqrt{Z_0}} \tag{3.17}$$

where V_1^{inc} and V_1^{ref} are the incident and reflected voltage waves, respectively. Therefore, $|a_1|^2$ is defined as the power incident on the input of the network, i.e the power available when the source impedance is Z_0. And $|b_1|^2$ is the power reflected back to the input port of the network. The general definition of the waves a_1 travelling into and b_1 travelling out of a 2-port network is:

$$a_1 = \frac{V_1 + I_1 Z_0}{2\sqrt{Z_0}} \tag{3.18}$$

$$b_1 = \frac{V_1 - I_1 Z_0}{2\sqrt{Z_0}} \tag{3.19}$$

and the relation between (a_1,a_2) and (b_1,b_2) can be written as a system of two linear equations:

$$b_1 = S_{11} a_1 + S_{12} a_2 \tag{3.20}$$

$$b_2 = S_{21} a_1 + S_{22} a_2 \tag{3.21}$$

where S_{11} is the input reflection coefficient with the output of the network terminated by a matched load ($a_2 = 0$). S_{21} and S_{12} are the forward transmission from port 1 to port 2 and the reverse transmission from port 2 to port 1, respectively, and S_{22} the output reflection coefficient, as shown in Fig. 3.9.

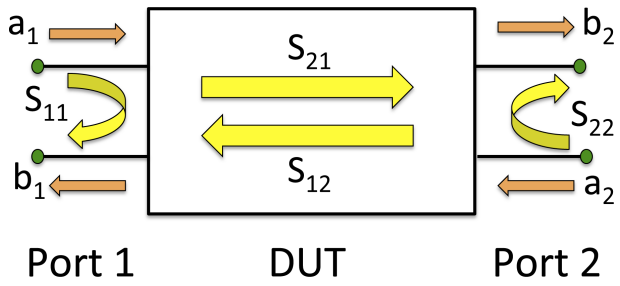

Figure 3.9: Scheme of the S-parameters for a 2-port network.

Using Eq. (3.18), Eq. (3.19), Eq. (3.20) and Eq. (3.21), the S_{11} parameter of a single impedance Z_L connected to a generator of source impedance Z_0 is found:

$$S_{11} = \frac{b_1}{a_1} = \frac{V_1 - I_1 Z_0}{V_1 + I_1 Z_0} = \frac{Z_L - Z_0}{Z_L + Z_0} \tag{3.22}$$

where the impedance Z_L is a function of frequency ω and given by the transmission line impedance equation [45]:

$$Z_L = Z_1 \frac{R_L + jZ_1 tan(\omega l/c)}{Z_1 + jR_L tan(\omega l/c)} \tag{3.23}$$

where l is the electrical length of the transmission line. From Eq.(3.23) it is seen that there is a perfect match ($S_{11} = 0$), when $(\omega l/c) = \pi/2$, i.e. when the electrical length of the transmission line is $\lambda/4$ or an odd multiple of $\lambda/4$, whereas an impedance mismatch will occur at the rest of frequencies. As it is shown in Fig. 3.10, there is a maximum-minimum pattern which depends on the distance between feedthroughs. The identical mismatching in both transitions of the stripline allows the existence of standing waves in the transmission line. There are reflection nodes at kicker lengths equal to multiple quarter wavelengths ($\lambda/4$, $3\lambda/4$, $5\lambda/4$, etc.) which represent a perfectly matched transmission for the correspondent frequencies. At those approximate frequencies, the reflected waves between both transitions separated by the transmission line present a null interference at odd multiples of $\lambda/4$ due to the composite S_{11} parameter of both transitions. In addition, the reflection may increase with frequency depending on the coaxial to stripline transition quality.

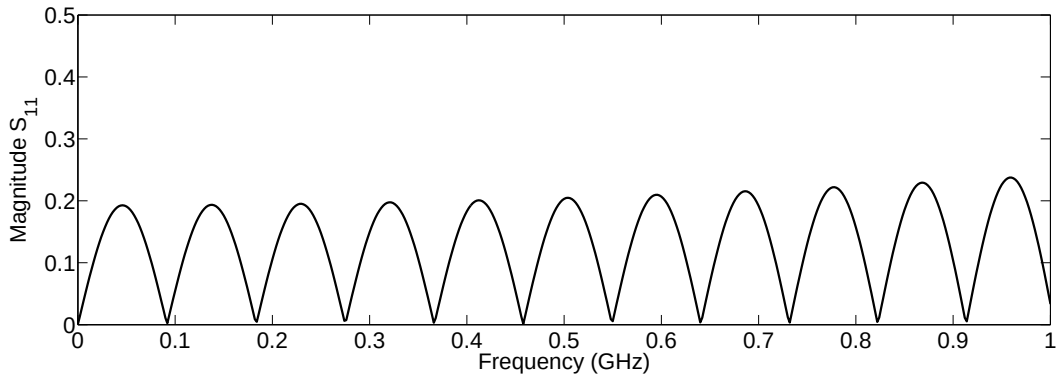

Figure 3.10: Typical plot for the reflection parameter of a stripline kicker.

Therefore, the reflection parameter of a stripline kicker has the same frequency response as a quarter-wave transformer. The quarter-wave transformer is a simple circuit that matches a real load impedance to a transmission line of length $\lambda/4$, as it is shown in Fig. 3.11. The load resistance R_L and the feedline characteristic impedance Z_0 are both real. These two components are connected with a lossless piece of transmission line of characteristic impedance Z_1. This approximation could be a good starting point if a stripline kicker must be designed with a reflection parameter magnitude below a certain value.

3.3.5 Wakefields and Impedances for Stripline Kickers

Longitudinal and Transverse Wakefields

A charged particle beam traveling inside a vacuum chamber, when passing by cross section variations of the vacuum chamber wall, induces electromagnetic fields, known as wakefields, which act back on the beam itself. These wakefields contain three spatial

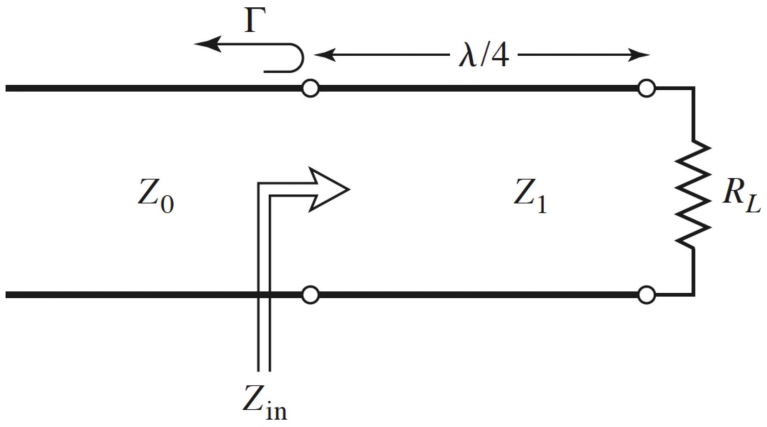

Figure 3.11: Schematic of a quarter-wave matching transformer [45].

components: longitudinal (directed along the average particle motion), and transverse (horizontal and vertical, or radial and azimuthal). The longitudinal component of the electric field may change the effective amplitude and phase of the applied accelerating field, and thereby the rate of acceleration, as well as the energy distribution in the bunch and its effective length. This in turn may influence the optics of the accelerator, in particular by changing the focusing, and the closed orbit around which particles perform transverse betatron oscillations. Similarly, transverse field components may increase the cross section of a bunch, change its closed orbit, its frequency of oscillation around it, and shorten the life time of the beam in storage rings due to increased loss of particles. These effects become more severe at higher beam currents.

Depending on the design of the vacuum chamber and other accelerator elements, longitudinal and transverse instabilities of a beam will occur. Then the beam may start to oscillate, develop tails and halos, and be partially or even completely lost. If the wakepotential induced by a bunch vanishes before the arrival of the next bunch (short-range wakefield or broadband impedance), it only affects the single-bunch dynamics. When the decay time of the wakefield is larger than the time spacing between the bunches (long-range wakefield or narrow-band impedance) the coupling between subsequent bunches cannot be neglected [54]. Other important consideration that should be taken into account is that the high intensity electromagnetic fields can excessively heat sensitive elements close to the beam, which may damage or even destroy them in some cases or produce undesirable increase in vacuum pressure [55]. This effect will be studied in Section 3.5.2.

Two different concepts arise when dealing with wakefields: wakefunctions and wakepotentials. Wakefunction is the normalized integral over the electromagnetic force due to fields excited by a point charge or delta function distribution. In the ultrarelativistic limit, the wakefunction depends only on the surrounding structure. The longitudinal wakefunction is obtained by integrating over the electric field component E_z normalized by the charge q [55]:

$$W_{\parallel} = -\frac{1}{q}\int_{-\infty}^{\infty} E_z dz \tag{3.24}$$

The minus sign makes the wakefunction positive for a decelerating electric field component. The dimensions of the wakefunction are V/C.

The transverse wakefunction is the transverse momentum kick experienced by the beam because of the deflecting fields [55]:

$$W_{\perp} = -\frac{1}{q}\int_{-\infty}^{\infty} (\mathbf{E} + \mathbf{v} \times \mathbf{B})_{\perp} dz \tag{3.25}$$

The transverse (horizontal and vertical) wakefunctions can be separated in two terms: the driving (or dipolar) and the detuning (or quadrupolar) components [54]:

$$W_x = W_x^{driv} x_0 + W_x^{det} x \tag{3.26}$$

$$W_y = W_y^{driv} y_0 + W_y^{det} y \tag{3.27}$$

where (x_0, y_0) and (x, y) define the transverse offset of source and test particle with respect to the geometric center of the structure, respectively.

The integrated effect over a finite distribution of charged particles is described by the wakepotential, which can be determined by the convolution of the wakefunction with the charge distribution in the bunch. Consequently, the wakepotential depends not only on the structure, but also on the charge distribution which excites it.

Longitudinal and Transverse Beam Coupling Impedances

When studying the beam dynamics in the time domain, as usually done for linear accelerators, it is convenient to make use of the wakefunctions or wakepotentials. However, the frequency domain analysis is usually adopted for circular accelerators due to the intrinsic periodicity. In frequency domain, the concept of beam coupling impedance is used, defined as the Fourier transform of the wakefunctions. Beam coupling impedance only depends on the surrounding structures, and does not depend on beam parameters except on its velocity.

In particle accelerators, the current consists of a beam of charged particles moving in high vacuum, and thus experiences no direct resistance. However, the electromagnetic fields excited by the moving charges induce currents and voltages in the surrounding vacuum chamber walls. The concept of a coupling impedance is introduced to relate the beam current to the total induced voltage along the beam trajectory. This voltage is defined as the normalized integral over all electromagnetic force components acting on the beam. For a beam moving with a constant velocity v, only the electric force is relevant in the direction of beam motion, since magnetic forces are perpendicular to it. The longitudinal impedance is then given by [55]:

$$Z_{\parallel} = \int_{-\infty}^{\infty} W_{\parallel} e^{j\omega\tau} d\tau \tag{3.28}$$

where $\tau = z/v$. The transverse coupling impedance is calculated as the integral over the Lorentz force in the transverse direction [55]:

$$Z_{\perp} = \int_{-\infty}^{\infty} W_{\perp} e^{j\omega\tau} \tau \tag{3.29}$$

This equation is normalized by the transverse momentum of the charge, which changes the dimension to Ω/m, i.e. impedance per transverse displacement. Analogously to its equivalent in the time domain the transverse beam impedance can be divided in two terms [54]:

$$Z_x = Z_x^{driv} x_0 + Z_x^{det} x \tag{3.30}$$

$$Z_y = Z_y^{driv} y_0 + Z_y^{det} y \tag{3.31}$$

In addition, a constant term also appears in Eq. 3.30 when the beam passes off axis in a symmetric geometry, generally defined as the transverse impedance when both source and test particle are on the nominal beam axis.

The impedance is in general a complex function. The real (or resistive) part of the longitudinal impedance, describes the energy loss, while the imaginary (or reactive) part shifts the frequency of the beam oscillation. Although the impedance and wake-function are integral transforms of each other, in practice they contain complementary information since the impedance is usually known up to some maximum frequency, while the wake function is calculated up to some finite time or distance. Hence the impedance description is more appropriate for long range phenomena, while the wake formalism is better over short distances.

Analytical Approximation for the Beam Coupling Impedance of a Stripline Kicker

The beam coupling impedance can be calculated analytically only for very few and idealized structures such as uniform, cylindrical beam pipes or closed pill-box cavities with rotational symmetry. For stripline beam position monitors (BPMs) and kickers, general expressions for longitudinal and transverse beam coupling impedance at low frequencies have been found [56] and will be used in the following.

The starting point for the analysis of the longitudinal and transverse beam coupling impedance of a stripline kicker is the study of the image currents I(ω) induced by the beam. A complete explanation about how the image currents created by the beam travel through the striplines is presented in [57–59]. As it is shown in Fig. 3.12, the image currents created in the beam pipe walls splits into two equal parts when arriving at the electrodes, one half going to the upstream port and the other half traveling

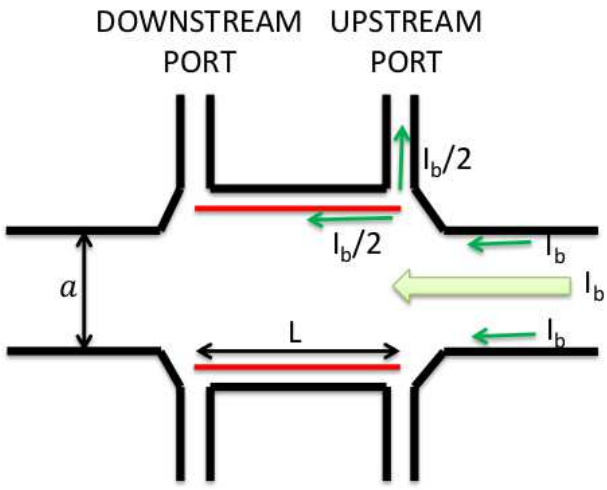

Figure 3.12: Stripline kicker operation model used for calculating the longitudinal beam coupling impedance.

through the plate: this is due to the upstream port and the striplines having the same characteristic impedance.

The same happens when the beam arrives to the downstream port. Therefore, when the beam passes the striplines, a current doublet is created in the upstream port, as shown in Eq. (3.32), whereas the current in the downstream port is cancelled:

$$I(\omega) = I_b \left(1 - e^{-j2\omega L/c}\right) \tag{3.32}$$

where I_b is the beam current, L is the electrode length and c is the speed of light. This is only true when the beam is ultrarelativistic. The voltage seen by the beam is $V_b = gV_u$, where g is the single-electrode geometrical factor and V_u is the voltage created by the image currents in the upstream gap, given by the expression:

$$V_u = \frac{Z_{even}}{2} g I(\omega) \tag{3.33}$$

The longitudinal beam coupling impedance is calculated as $Z_{\|} = V_b/I_b$, and therefore [56]:

$$Z_{\|}(\omega) = \frac{Z_{even}}{2} g_{\|}^2 \left[sin^2\left(\frac{\omega L}{c}\right) + j sin\left(\frac{\omega L}{c}\right) cos\left(\frac{\omega L}{c}\right)\right] \tag{3.34}$$

In Eq. (3.34), $g_{\|}$ is the longitudinal geometric factor when considering the two electrodes, Z_{even} is the even mode characteristic impedance and L is the striplines length. The longitudinal geometric factor can be numerically calculated with a 2D electrostatic solver. The method consists of modelling a cross-section of the striplines in the even mode configuration, i.e. both electrodes have the same voltage and the same polarity, and calculate the voltage at the center of the striplines. The ratio between the voltage at the centre and the voltage of the electrode is the longitudinal geometric factor. The

longitudinal factor tends to ϕ_0/π when the striplines aperture is equal to the beam pipe diameter, where ϕ_0 is the coverage angle of the striplines.

The dipolar component of the transverse beam coupling impedance can be calculated in a similar way, when considering that the image currents created by an off-centered beam are unequally divided, and defined as [58]:

$$I_+ = (I(\omega)/2)(1 + x_b/b) \tag{3.35}$$

$$I_- = (I(\omega)/2)(1 - x_b/b) \tag{3.36}$$

where $I(\omega)$ is given by Eq.(3.32), x_b is the offset of the beam with respect to the centre of the aperture, and b is the distance between the centre of the aperture and the electrode, i.e. half of the aperture. Therefore, equal but opposite voltages are assumed to be induced in the electrodes, which is related with the odd mode of the striplines. Using the same approximation as for the longitudinal case, the voltage at the right electrode (supposing horizontal striplines) is given by:

$$V_R = \frac{Z_{odd}}{2} g_\perp \frac{x_b}{b} I(\omega) \tag{3.37}$$

where Z_{odd} is the odd mode characteristic impedance and $g_\perp$ is the transverse geometric factor. Assuming a linear distribution of the longitudinal voltage with x, it can be expressed as:

$$V(x) = V_R g_\perp \frac{x}{b} \tag{3.38}$$

The transverse impedance is defined as [58]:

$$Z_\perp(\omega) = j\frac{\Delta p_\perp c}{I_b x_b} \tag{3.39}$$

where $\Delta p_\perp$ is the transverse momentum change of a particle, defined as:

$$\Delta p_\perp = -\frac{1}{j\omega}\frac{\partial V(x)}{\partial x} = -\frac{1}{j\omega} g_\perp^2 \frac{I(\omega) x_b}{2b^2} Z_{odd} \tag{3.40}$$

The dipolar component of the transverse beam coupling impedance is, therefore [56]:

$$Z_\perp = Z_{odd}\left(\frac{g_\perp}{b}\right)^2 \frac{c}{\omega}\left[sin^2\left(\frac{\omega L}{c}\right) + jsin\left(\frac{\omega L}{c}\right)cos\left(\frac{\omega L}{c}\right)\right] \tag{3.41}$$

As in the longitudinal case, $g_\perp$ can be calculated with a 2D electrostatic solver; however, in this case, the cross-section of the striplines is modelled in the odd mode, i.e. both electrodes have the same voltage but opposite polarity. The voltage is calculated at a distance x from the center, and $g_\perp$ is calculated as $g_\perp = V(x,0)b/x$ for an electrode voltage of ± 1 V. The transverse factor tends to $4/\pi$ when the striplines aperture is the same as the beam pipe diameter.

In axisymmetric structures, there is no quadrupolar component of the transverse beam coupling impedance. However, this is not the case of the stripline kicker, and therefore, this component must be taken into account. No analytical expressions for the quadrupolar component of the transverse beam coupling impedance has been found in the literature, and further studies will be developed in order to find an equivalent expression of Eq. (3.41) for the quadrupolar component.

Other expressions for longitudinal and transverse beam coupling impedance have been found in [57,59,60]. However, these equations assume that the striplines have the same aperture as the beam pipe diameter, and therefore, will not be used in this thesis.

Low-frequency approximation for the longitudinal beam coupling impedance. In general, an impedance is a function of frequency rather than just a value. For longitudinal beam coupling impedance, when saying that the impedance of a vacuum chamber is a certain number of Ω refers only to the low-frequency limit of $Z_{\|}/n$, i.e. the impedance divided by the harmonic number $n = \omega/\omega_0$, where ω_0 is the revolution frequency. At low frequencies, the imaginary part of many impedances becomes more proportional to frequency, and hence to the harmonic number, while the real part vanishes more rapidly. The imaginary part of the ratio $Z_{\|}/n$ thus tend to a single value. For the transverse beam coupling impedance, it refers to the value of the imaginary component when $\omega/2pi << c/4L$. However, these values do not contain any information about the non less important high-frequency behavior of the beam coupling impedance function.

For a stripline kicker, the longitudinal impedance per harmonic and the transverse impedance at low frequencies ($\omega/2\pi << c/4L$) are, respectively:

$$\frac{Z_{\|}}{n} \approx jg_{\|}^2 Z_{even} \frac{\pi L}{cT_0} \tag{3.42}$$

$$Z_{\perp} \approx jg_{\perp}^2 Z_{odd} \frac{L}{2b^2} \tag{3.43}$$

where T_0 is the revolution period of the accelerator.

3.4 Optimization of the Striplines Geometry

The optimization of the striplines kicker for the CLIC DRs has been started from one of the specifications of Table 2.3, the effective length L of the stripline kicker, which is 1.7 m. For this kicker length, and an aperture a = 20 mm, the voltage V_k that must be applied to each electrode can be found by the relation:

$$V_k = \frac{aV_{\perp}}{4L} \tag{3.44}$$

where $V_{\perp}$ is the transverse voltage that a particle experiences when passing through the kicker due to the travelling electromagnetic fields, defined as:

$$V_{\perp} = \int (\mathbf{E} + \mathbf{v} \times \mathbf{B})_{\perp} dz \tag{3.45}$$

There is a close relation between the deflection angle α and the transverse voltage, by means of the beam energy E_b [31]:

$$\alpha = tan^{-1}\left(\frac{V_{\perp}}{E_b}\right) \approx \frac{V_{\perp}}{E_b} \tag{3.46}$$

This approximation can be done for small deflection angles. For extracting the beam from the CLIC DRs, with an energy of 2.86 GeV and a deflection angle of 1.5 mrad, as shown in Table 2.3, a transverse voltage of 4.3 MV is required. From the transverse voltage, the voltage applied to each electrode V_k has been calculated. For a striplines aperture of 20 mm and a deflection angle of 1.5 mrad, a striplines length of 1.7 m allows for an electrode voltage of ± 12.5 kV. To calculate the current passing through the striplines when the kicker is operating, the relation $I_k = V_k/Z_0$ should be used.

3.4.1 2D Calculations for the Striplines Cross-Section Optimization

For two coupled transmission lines, two TEM modes exist, odd and even mode, and therefore two characteristic impedances have to be taken into account. The characteristic impedance of both odd and even modes should ideally be optimized to 50 Ω, since this value represents an optimum compromise between power transmission and energy losses [45]. In addition, this characteristic impedance is a standard value and thus commercial components are available. However for coupled electrodes this is not possible to achieve. Ensuring that the odd mode characteristic impedance of each electrode is close to 50 Ω will avoid large mismatches to the characteristic impedance of feedthroughs, coaxial cables and the inductive adder. This will help to minimize reflections when pulses are applied to energize the electrodes, as it will be shown in Section 3.4.2. On the other hand, the longitudinal beam coupling impedance is directly proportional to the even mode characteristic impedance, so it is desirable that the even mode impedance will be not larger than 50 Ω: this will be also shown in Section 3.4.2.

Due to the tight requirement for beam coupling impedance, as well as the fact that the inductive adder could hold a certain degree of impedance mismatch, it was decided that the starting point for the striplines design would be to achieve 50 Ω characteristic impedance in the even mode, to minimize impedance mismatches seen by the beam, while keeping the odd mode characteristic impedance as close as possible to 50 Ω.

Striplines Cross-Section: Flat and Curved Electrodes

As a first approximation, an analytical method has been developed in this thesis, in order to calculate the characteristic impedance for a stripline kicker in both operation

modes. In this approach, the dependence of the odd and even mode characteristic impedances upon the cross section geometry of the striplines has been studied.

As shown in Eq. (3.13) and Eq. (3.14), Z_{odd} and Z_{even} depends on the striplines geometry by the ratios d/R, h/R and w/R, where $d = R - a - w$. Since the thickness of the electrodes w must be kept between 3 and 4 mm for mechanical considerations and the aperture a is 20 mm, only the ratio h/R is considered. Therefore, the odd and even characteristic impedances of the striplines approximation have been only studied as a function of the ratio between the electrode height and the stripline beam pipe radius h/R: these parameters are shown in Fig. 3.13.

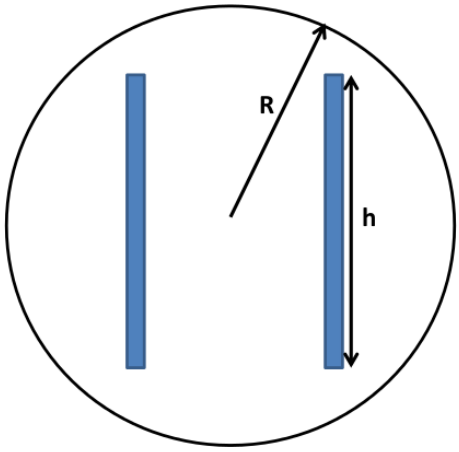

Figure 3.13: Schematic of a stripline kicker, where the parameters used in the analytical appproximation are shown.

The analytical results for the odd and even characteristic impedances, given by Eq. (3.13) and Eq. (3.14) are plotted in Fig. 3.14. This figure represents Z_{odd} and Z_{even}, when changing the ratio between the electrode height and the stripline beam pipe radius h/R, for three different radius: 20 mm, 25 mm and 30 mm. These three radius are commercial radius and were considered during the design study. Results confirm that a small stripline beam pipe radius results in closer values of even and odd mode characteristic impedances, and that the even mode characteristic impedance of striplines is always higher than the odd mode.

This analytical approach has turned out to be a simple, but very effective, method to understand how the odd and even characteristic impedances change with the electrode shapes. To evaluate the potential of the method, numerical results have been compared with the analytical results. Firstly, the studied striplines cross-sections consist of flat and curved electrodes inside a cylindrical beam pipe, as shown in Fig. 3.15, since they are the most common cross-sections used for striplines. The extraction kickers for the ILC DRs and the CTF3 CR [31, 34], have flat electrodes. Flat electrodes are usually designed with curved edges, as shown in Fig. 3.15, to improve mechanical stiffness and diminish the end effects upon the uniformity of the field. In DAΦNE, the injection kicker has elliptical cross-section, both electrodes and beam pipe [36];

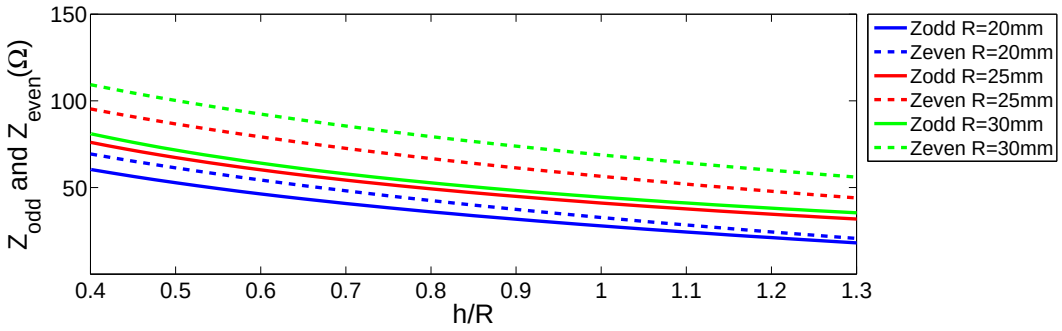

Figure 3.14: Analytical estimate for the odd and even modes characteristic impedance versus h/R.

however this geometry has not been considered for the CLIC DRs, since the transition from circular beam pipe to the elliptical striplines beam pipe will increase the beam coupling impedace.

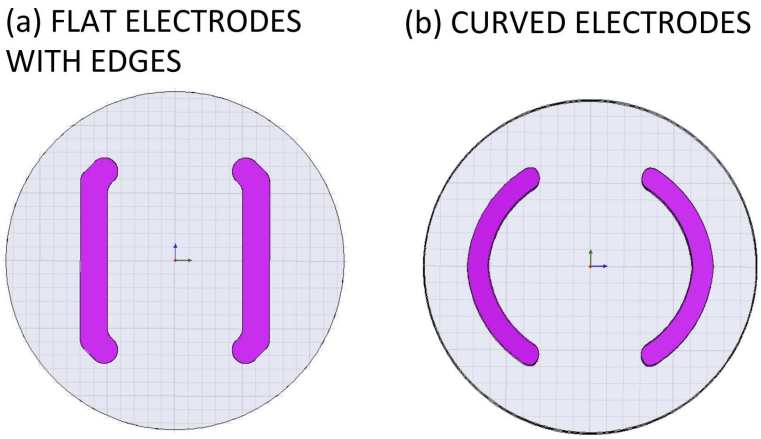

Figure 3.15: Electrode shapes studied: (a) flat electrodes with edges, and (b) curved electrodes.

Flat electrodes have a very good field uniformity at the center of the aperture. However, a larger stripline beam pipe is required in order to reduce the maximum electric field between the electrodes and the beam pipe walls: it increase the mismatching between the characteristic impedances of the two operation modes, as shown in Fig. 3.14. On the other hand, with curved electrodes it is difficult to achieve good field homogeneity, whereas a smaller radius and therefore, a better impedance mismatching, is more easily achieved than in the case of flat electrodes.

The characteristic impedance and the field homogeneity of these two models have been calculated, and results will be shown in the following. Computer simulations have been carried out by changing the ratio between the electrode height (*h* in Fig. 3.16) and the stripline beam pipe radius *R*, for the three different stripline beam pipe radii used in the analytical approximation: 20, 25 and 30 mm.

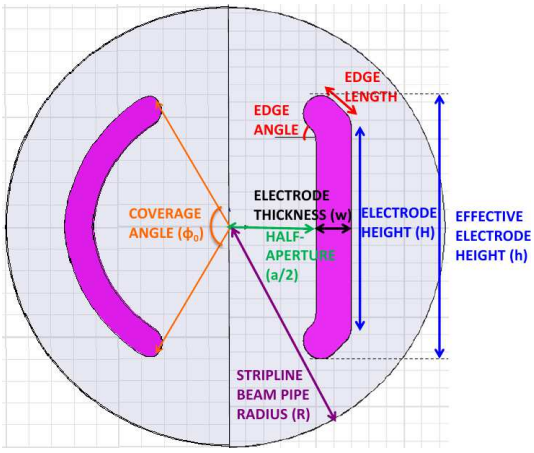

Figure 3.16: Geometric parameters used to optimize the shape of the electrodes for a curved and a flat electrode

Characteristic Impedance. The characteristic impedance of the striplines has been numerically calculated with the 3D solver High Frequency Structure Simulator (HFSS) [61], for the electrode shapes shown in Fig. 3.15. HFSS is a commercial Finite Element Method (FEM) solver from Ansys, in frequency domain, for electromagnetic structures. Although 2D codes exist which numerically solve the electromagnetic fields of a structure, with HFSS it is easy to go from the 2D model to the 3D model. To calculate the characteristic impedance with HFSS, a thin slice of a quarter of the striplines has been modeled. For simulating a quarter of the striplines, and take into account the two operating modes (odd and even), proper symmetries should be used, as shown in Fig. 3.17 for flat electrodes.

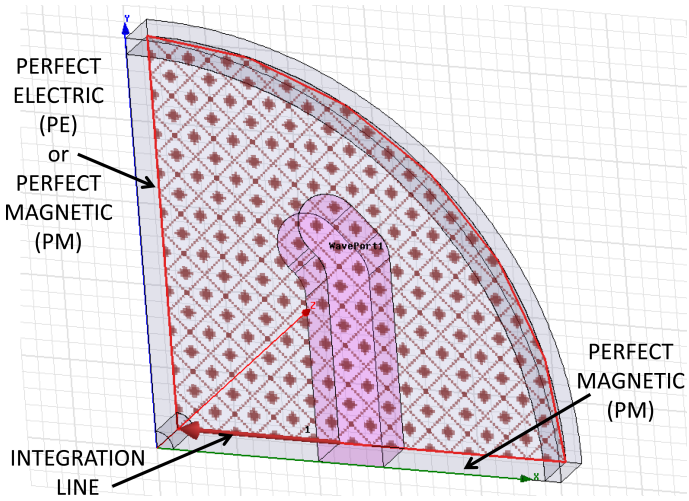

Figure 3.17: Boundary conditions and integration line of the HFSS model for flat electrodes.

The odd mode has been modelled by using an electric wall, i.e. perfect electric (PE) boundary condition, between the striplines: this type of symmetry forces the electric field to be perpendicular to the surface. For the even mode, a magnetic wall, or perfect magnetic (PM) boundary condition, has been used, forcing the electric field to be tangential to the surface. The same boundary conditions have been used for all the studied electrode shapes. The Driven Modal simulator has been used with waveguide ports. The waveports are calibrated using integration lines, defined as the path over which HFSS integrates the electric field to obtain the voltage at a waveport: the path line defined in our models is shown in Fig. 3.17. HFSS uses this voltage to compute the characteristic impedance. Due to the magnetic symmetry in the horizontal plane, the characteristic impedance calculated with HFSS has to be divided by two. The frequency used for the simulations has been 10 MHz, although for these simulations this parameter is not relevant. The calculated characteristic impedance with HFSS is shown in Fig. 3.18 for both electrode shapes.

The agreement between the analytical approximation studied before, and the HFSS simulation is very good, especially for flat electrode. This result is as expected, the flat electrodes behave as a planar parallel capacitor, except for the round edges. For curved electrodes, the odd and even characteristic impedances remain separated in all the range studied, and for 25 and 30 mm radius an even mode characteristic impedance of 50 Ω has been impossible to achieve, over the range of h/R studied. In both cases, the smaller the radius, the closer values between both characteristic impedances, which agrees with the results obtained with the analytical approach.

Field Inhomogeneity. The field inhomogeneity of the striplines has been calculated by finding the maximum and mininum values of the deflecting field component in a semi-circle of 1 mm radius, and results are shown in Fig. 3.19. For flat electrodes, the field inhomogeneity goes below the maximum value allowed, i.e. $\pm 0.01\%$, for 25 and 30 mm radius. For curved electrodes, the field inhomogeneity required is never achieved in the range studied. This result is as expected: curved electrodes provide a poor field uniformity compared with the field homogeneity achieved when using flat electrodes.

Discussion of the Flat and Curved Electrodes Results. In order to have a 50 Ω even mode characteristic impedance, and the field homogeneity required, the optimum geometric parameters for each electrode shape have been defined, and they are collected in Table 3.1.

For flat electrodes it is possible to achieve the required field inhomogeneity with beam pipe radii of 25 mm and 30 mm. For a beam pipe of 25 mm radius, the field inhomogeneity requirement is achieved when $h/R \geq 0.7$, as shown in Fig. 3.19. Looking now to Fig. 3.18, it is seen that Z_{even} is 50 Ω for a ratio h/R of 1.0, and at this point, the odd mode characteristic impedance $Z_{odd} = 36.8\ \Omega$. The same can be done for a beam pipe of 30 mm radius. In this case the field inhomogeneity is consistently below

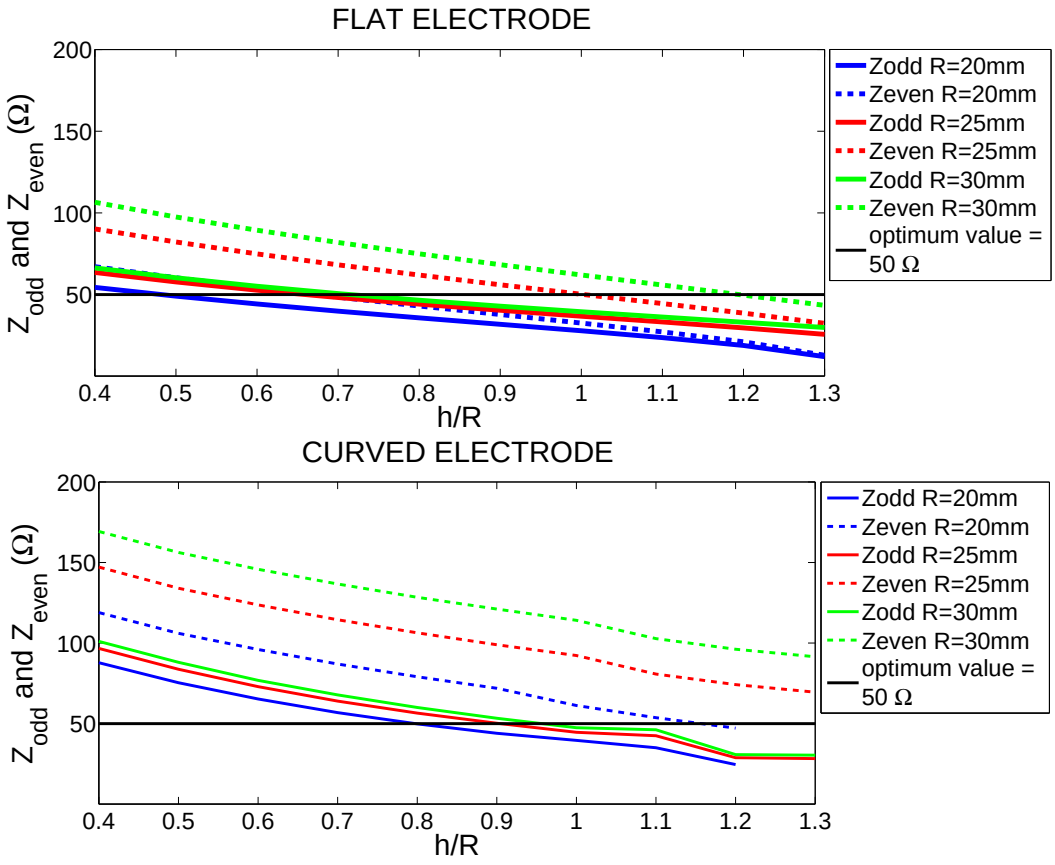

Figure 3.18: Odd and even mode characteristic impedance versus h/R, for flat and curved electrodes.

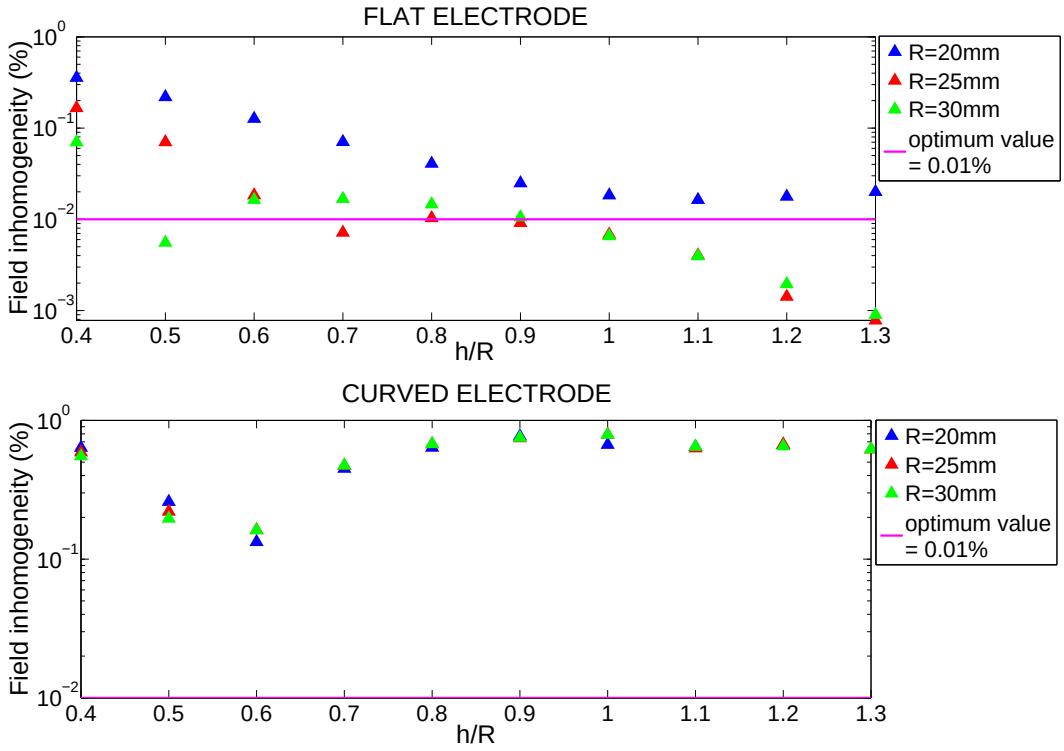

Figure 3.19: Odd mode field inhomogeneity over 1 mm radius versus h/R, for flat and curved electrodes.

Configuration	R (mm)	h/R	$Z_{odd}(\Omega)$	Field inhomogeneity
Flat	25	1.0	36.8	$< \pm 0.01\%$
Flat	30	1.2	33.1	$< \pm 0.01\%$
Curved	20	1.1	37.0	$\pm 0.65\%$

Table 3.1: Optimum values for the geometric parameters of the striplines studied, for a $Z_{even} = 50\,\Omega$.

0.01 % for $h/R \geq 1$, and $Z_{even} = 50\ \Omega$ is achieved for a $h/R = 1.2$. For this value, a $Z_{odd} = 33.1\ \Omega$ has been calculated. For curved electrodes, the high field homogeneity required has not been possible to achieve, due to the curved surface of each electrode facing the other electrode, which distorts the field lines. In addition, only with a 20 mm radius a 50 Ω even mode characteristic impedance has been achieved, with a $Z_{odd} = 37\ \Omega$ and a field inhomogeneity of 0.65 %, which is 65 times higher than the maximum field inhomogeneity required.

A New Electrode Shape: Half-moon Electrode

The study of the flat and curved electrodes presented before results in an optimum geometry for the CLIC DRs striplines that consists of flat electrodes inside a beam pipe of 25 mm radius, in order to achieve an even mode characteristic impedance of 50 Ω and a field inhomogeneity below ± 0.01 % over a circumference of 1 mm radius at the center of the striplines. However, for this geometry, the odd mode characteristic impedance is 36.8 Ω, a value that may introduce a significant distortion on the pulse produced by the inductive adder by increasing the settling time, as well as the transmission of the pulse through the striplines, due to the impedance mismatching. A closer value of the odd mode characteristic impedance to 50 Ω would be desirable. For that reason, other approaches were studied.

In the ILC injection and extraction kickers [34, 36], as well as in the CTF3 CR kicker [31], only the deflecting (odd) mode has been optimized to have 50 Ω characteristic impedance. This is also the case of the electrostatic injection kicker that has been developed and installed in the KEK digital accelerator [33], shown in Fig. 2.7. In addition, an electrostatic kicker is not the most suitable solution for the CLIC DRs extraction kicker, as it makes use of only the electric field, whereas a stripline kicker makes use of both electric and magnetic fields to deflect the beam, making stripline kickers more efficient than electrostatic kickers. Furthermore, due to their lower efficiency, an electrostatic kicker needs to be larger than a stripline kicker for the same deflection angle, which makes the filling time of an electrostatic kicker longer than in a stripline kicker.

A design for good matching of both the odd and even mode characteristic impedances, is being developed for the Advanced Photon Source Upgrade (APS-U) injection kicker [62]. In this kicker, good matching is achieved by introducing ground fen-

ders in the cross section of the striplines. These ground fenders are not useful in our case: with these it is not possible to achieve the excellent field homogeneity required for the extraction kicker of the CLIC DRs. Furthermore, due to the small aperture, fenders would be very close to the electrode edges, so the electric field in those regions would be too high. In addition, due to the long striplines, ground fenders should be manufactured as an independent part, and it would be difficult to assemble them with high accuracy.

The studies of the odd and even characteristic impedance and field homogeneity of the flat and curved electrodes developed in this thesis has shown that flat electrodes have a good field homogeneity, whereas curved electrodes allow for smaller radius, which helps to match both characteristic impedances. Therefore, in order to combine both features, a new electrode shape was proposed, that in the following will be known as half-moon electrode. This new electrode shape allows for both features: the flat part of the electrode gives a good field homogeneity whereas the curved part of the electrode allows for a suitable impedance matching. Three half-moon electrodes, shown in Fig. 3.20, were considered: the first shape (Fig. 3.20, (a)) was the most simple from the geometric point of view, although it was rejected due to the high electric field that can be expected near the sharp edges of the electrode. In order to decrease the electric field, rounded edges were considered, and a new geometry of half-moon electrodes was considered (Fig. 3.20, (b)). Finally, in order to decrease the beam pipe radius and have a better matching of the two characteristic impedances, another half-moon electrode shape was designed, with round edges perpendicular to the electrodes, as it is shown in Fig. 3.20, (c).

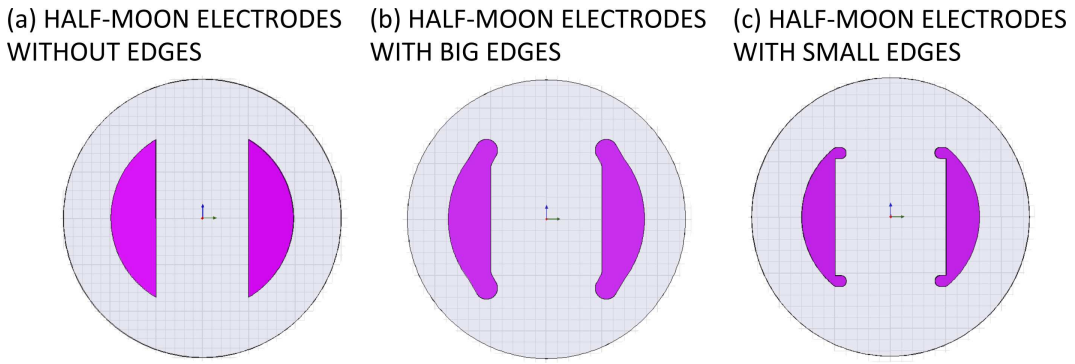

Figure 3.20: New electrode shapes studied: (a) half-moon electrodes without edges, (b) half-moon electrodes with big edges, and (c) half-moon electrodes with small edges.

Characteristic Impedance. The calculated characteristic impedance with HFSS is shown in Fig. 3.21 for the two electrode shapes considered. The half-moon electrode with big edges (Fig. 3.20 (b)) has a similar behaviour as flat electrodes, whereas the

half-moon electrodes with small edges (Fig. 3.20) (c)) have equal odd mode characteristic impedances for the different beam pipe radii considered. The reason for that could be the fact that, for this geometry, the effective distance between electrodes is smaller, due to the completely perpendicular edges. This makes the capacitance between the electrodes C_{12} increase and become the dominant factor in the odd mode characteristic impedance $C_{odd} = C_{11} + 2C_{12} \approx 2C_{12}$. Since C_{12} only depends on the electrode height and the distance between the electrodes (the aperture), no variation with the beam pipe radius is expected. Again, the smaller the radius, the better matching between both operation modes.

Field Inhomogeneity. The field inhomogeneity of the striplines with half-moon geometry has been calculated as in the case of flat and curved electrodes, and results are shown in Fig. 3.22.

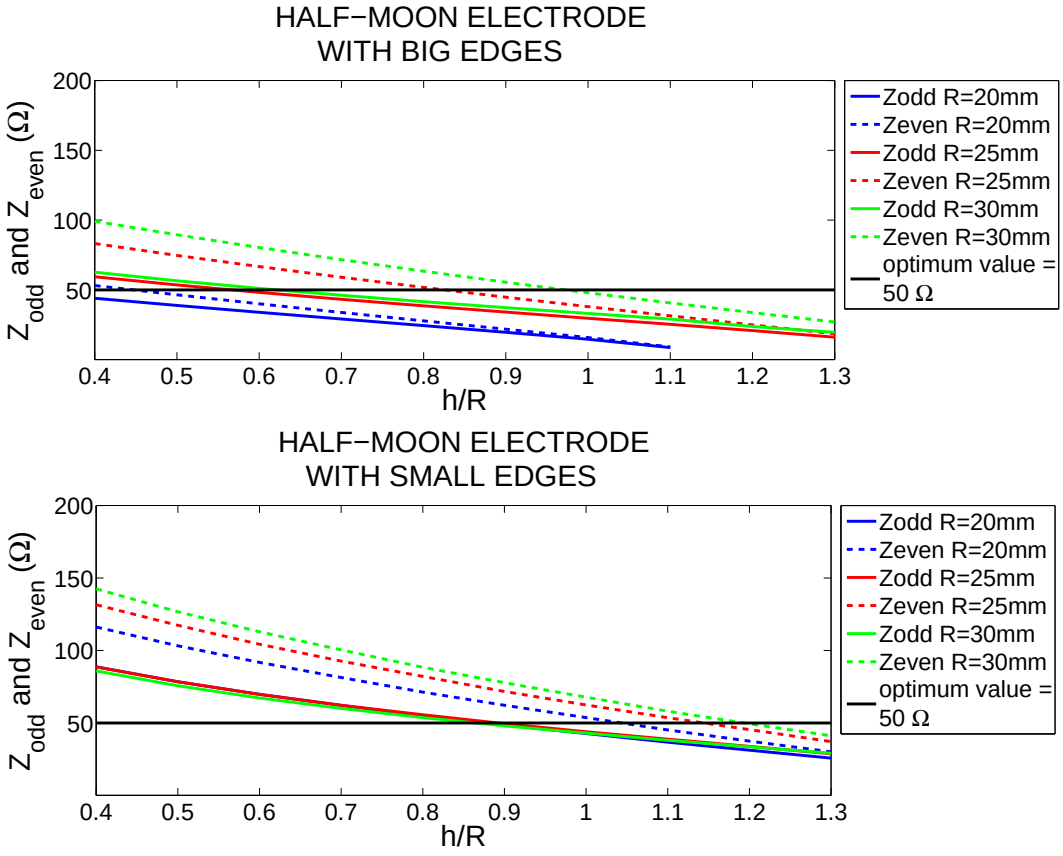

Figure 3.21: Odd and even mode characteristic impedance versus h/R, for half-moon electrodes.

For half-moon electrodes with big edges, a stripline beam pipe radius of 25 mm or 30 mm is required in order to have a field inhomogeneity below ±0.01%, whereas for the half-moon electrodes with small edges, the required field homogeneity is achieved

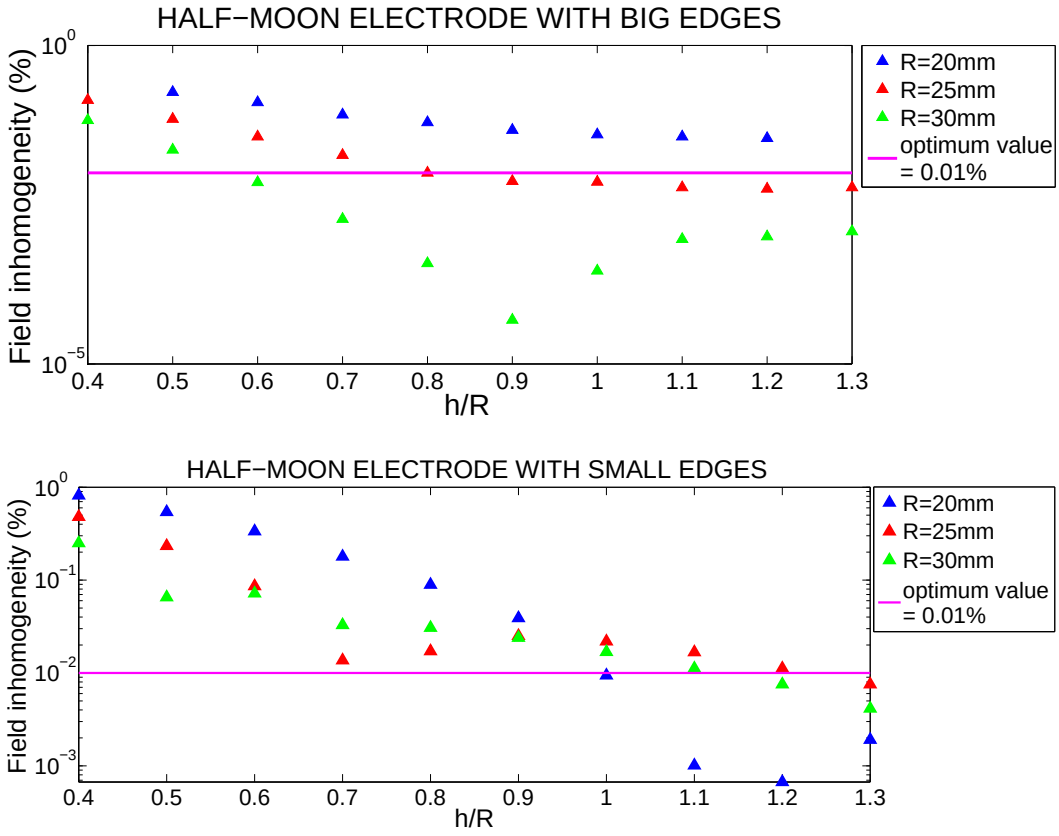

Figure 3.22: Odd mode field inhomogeneity over 1 mm radius versus h/R, for half-moon electrodes.

for the three radii, but only for high values of h/R, due to the perpendicular edges which distort the field lines, with more impact when the electrodes are small.

Discussion of the Half-moon Electrodes Results. Table 3.2 shows the characteristic impedance and field inhomogeneity results for the two types of half-moon electrodes considered. As in the case of flat and curved electrodes, a small stripline beam pipe radius allows for a better impedance matching of the two operation modes: this was also expected from the analytical approximation. For the half-moon electrode shape with big edges, a minimum radius of 25 mm is required in order to achieve the field homogeneity, whereas for half-moon electrodes with small edges it is achieved with 20 mm striplines beam pipe radius: it makes that the odd mode characteristic impedance is closer to 50 Ω for the latter case.

Configuration	**R (mm)**	**h/R**	**Z_{odd}(Ω)**	**Field inhomogeneity**
Half-moon with big edges	25	0.8	38.6	$< \pm 0.01\%$
Half-moon with big edges	30	1.0	34.2	$< \pm 0.01\%$
Half-moon with small edges	20	1.05	40.9	$< \pm 0.01\%$
Half-moon with small edges	30	1.2	33.6	$< \pm 0.01\%$

Table 3.2: Optimum values for the geometric parameters of the striplines studied, for a $Z_{even} = 50\,\Omega$.

Final Discussion for the Striplines Cross-Section

As shown in Table 3.1 and Table 3.2, with flat electrodes and half-moon electrodes it is possible to achieve the required field inhomogeneity. For flat electrodes with 50 Ω even mode characteristic impedance, an odd mode characteristic impedance of 36.8 Ω was achieved with a stripline beam pipe radius of 25 mm. For half-moon electrodes with big edges, the highest odd mode characteristic impedance achieved is 38.6 Ω for a 25 mm radius, whereas an odd mode of 40.9 Ω has been achieved with half-moon electrodes with small edges and a stripline beam pipe radius of 20 mm. The higher odd mode impedance for the half-moon electrodes with small edges is due to the smaller radius, which makes the distance between the electrode and the stripline beam pipe smaller than for either the flat electrodes or the half-moon electrodes with big edges.

Taking into account these results, more time consuming studies have been done only for flat and half-moon electrodes with small edges (from now on, half-moon electrodes), in order to compare the features of both electrode shapes, which will allow the final geometry design of the striplines to be chosen.

RF Breakdown Calculations

The maximum electric field that the stripline kicker can hold without RF breakdown issues has been calculated with HFSS and compared with the Kilpatrick criterion, for the two electrode shapes considered. In all the models, the waveport has been excited with a power of 3.125 MW, which corresponds to the power created by a voltage of 12.5 kV. Results are shown in Fig. 3.23 and Table 3.3.

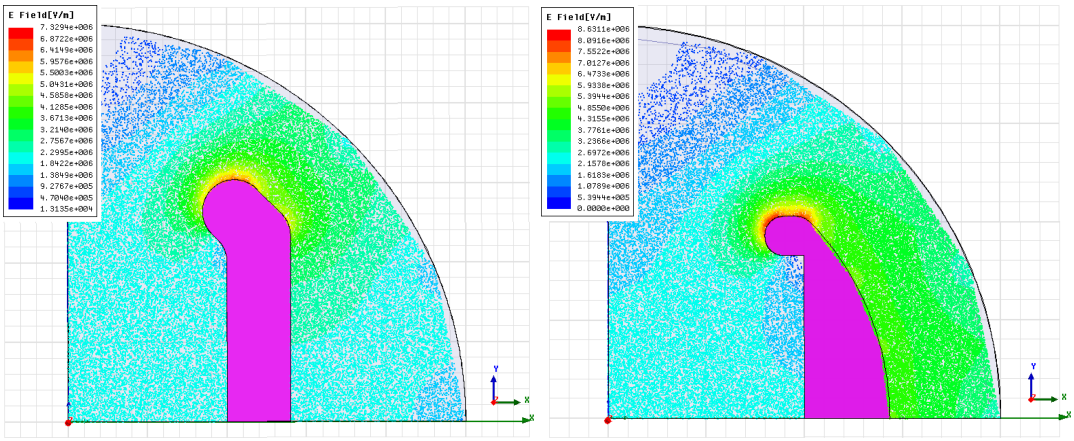

Figure 3.23: Maximum electric field expected for a pulse power of 3 MW, for the two geometries considered.

Configuration		**R (mm)**	**h/R**	**E_k** (MV/m)
Flat	(a)	25	1.0	7.3
Half-moon with small edges	(e)	20	1.05	8.6

Table 3.3: Summary of the results for the maximum electric field E_k expected in the striplines beam pipe wall.

As it is shown in Table 3.3, the expected maximum electric field is 7.3 MV/m for flat electrodes and 8.6 MV/m for half-moon electrodes, for a minimum distance between the electrode and the beam pipe wall of 6.8 mm and 5.8 mm, respectively. Furthermore, the two geometries have different edge rounding radius, which also affects the maximum electric field: 2 mm for flat electrodes and 1 mm for half-moon electrodes. In the case of the half-moon electrode, this value is higher than for flat electrodes due to the smaller beam pipe radius, which makes the distance between the electrode and the beam pipe wall smaller, and the smaller edge rounding radius. Both values exceed the maximum value given by the Kilpatrick limit, which is 5.5 MV/m for a pulse frequency of 10 MHz. In order to decrease the maximum electric field expected, the distance between the electrodes and the beam pipe wall could be increased, however it will change the characteristic impedances of both odd and even modes and

the field homogeneity. The rounding radius could be also increased in order to diminish the maximum electric field, but it would make more difficult the manufacturing process. Therefore, and taking into account that the Kilpatrick limit gives a conservative value for the maximum electric field, these values represent a good compromise between kicker specifications, fabrication criterion and safety.

3.4.2 3D Calculations for the Striplines Optimization

Reflection Parameter S_{11} for the Stripline Kicker

A total of four coaxial feedthroughs are required to transfer power from the inductive adders to the two electrodes and from the electrodes to the two 50 Ω loads. The feedthroughs are coaxial outside of the beam pipe but the connection from a feedthrough to an electrode cannot be coaxial: hence the characteristic impedance of the connection to the electrode is not 50 Ω. To characterize the impedance mismatching due to the feedthrough-electrode connection in both flat and half-moon electrodes, a 3D model of the two geometries must be studied. At that point, a commercial stripline tube of 40.5 mm with thin wall was found, and therefore, from this model on all the simulations were done for a stripline beam pipe radius of 20.25 mm. To model the coaxial feedthroughs the well-known formula for the characteristic impedance of a coaxial line, with vacuum as dielectric, has been used [45]:

$$Z_0 = \frac{ln(b/a)}{2\pi c\epsilon_0} \tag{3.47}$$

where $\epsilon_0 = 8.854 \times 10^{-12} F/m$ and a and b are the inner and outer radius, respectively. A commercial feedthrough was being considered at that point, with an inner conductor of 1.8 mm radius. For that reason, in order to have 50 Ω characteristic impedance, a coaxial line with 1.8 mm inner radius and 4.1 mm outer radius has been used. In addition, a 100 mm length feedthrough was considered for the same reason.

For beam coupling impedance simulations, a wire between the electrodes should be modelled in HFSS, whereas with the Computer Simulation Technology (CST) [63] it is possible to use a particle beam instead of a wire, which makes the simulation more realistic but not so comparable with measurements. For that reason, it was decided to export the HFSS model to the CST solver, in order to be able to optimize the striplines from both the reflection parameter and the beam coupling impedance point of view by using the same model in CST Microwave Studio (MWS) and CST Particle Studio (PS), respectively. CST is a commercial solver for electromagnetic simulation of high frequency components, in time domain, whereas HFSS is a solver in frequency domain. Therefore, a benchmarking between the results from HFSS and CST MWS was done. A good agreement was found for the S_{11} parameter, as shown in Fig. 3.24.

The coaxial feedthroughs for the model shown in Fig. 3.25 are placed at 4 mm of distance from the electrode ends. This distance was changed in order to study the

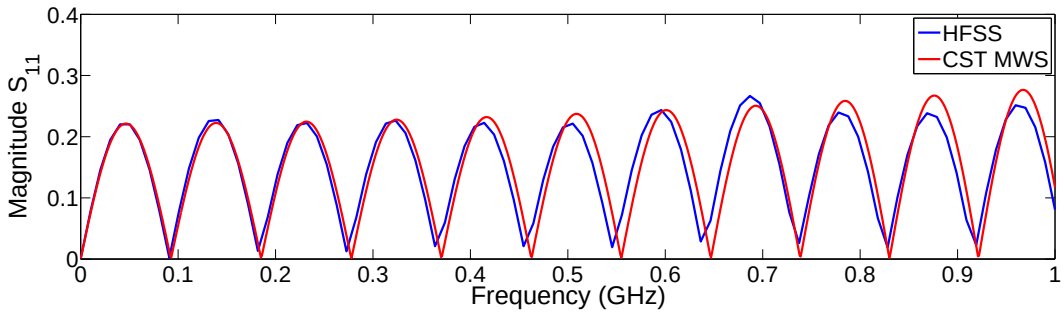

Figure 3.24: Comparison of the S_{11} parameter for half-moon electrodes in the odd mode, calculated with HFSS and CST MWS.

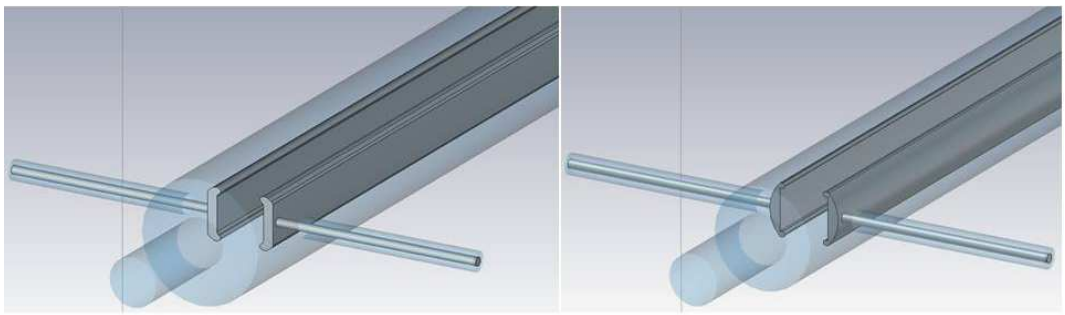

Figure 3.25: CST model, exported from HFSS, used to compare the S_{11} parameter for flat electrodes (left) and half-moon electrodes (right).

dependence of the reflection parameter magnitude with the feedthroughs position, but no significant differences were found in the magnitude of the reflection parameter.

The two operation modes, odd and even, have been simulated using waveguide ports at the input of the coaxial feedthroughs. For the odd mode, an electric wall has been used as a symmetry between the electrodes, whereas for simulating the even mode, a magnetic wall has been used. No material information has been added to the model: the electrodes are assumed to be Perfect Electric Condutor (PEC) and the beam pipe is vacuum, with a background of PEC. The total length of the striplines modelled has been 1.6 m, in order to leave space for the transitions between the striplines beam pipe and the CLIC DR beam pipe. By using the adaptive mesh refinement feature of the Transient Solver of CST MWS, the optimum number of cells per wavelength has been found to be 25, with a number of hexahedral mesh cells of about $3{\times}10^5$ for the half-model. The results are shown in Fig. 3.26 and Fig. 3.27, for the odd and even modes, respectively.

In the odd mode, the flat electrode has a maximum reflection magnitude between 0.3 and 0.5 in the frequency range analyzed (up to 1 GHz), whereas the half-moon electrode shape has a reflection parameter consistently below 0.3. Furthermore, the peaks of the reflection parameter increase with frequency and, for flat electrodes, the increase is higher than in the case of the half-moon electrode, due to the fact that, for

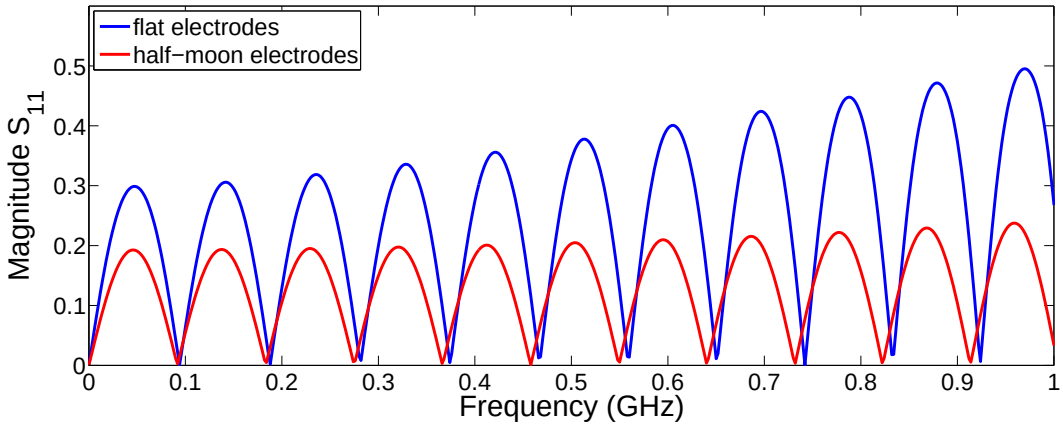

Figure 3.26: Odd mode S_{11} parameter numerically calculated for flat electrodes (blue) and half-moon electrodes (red) .

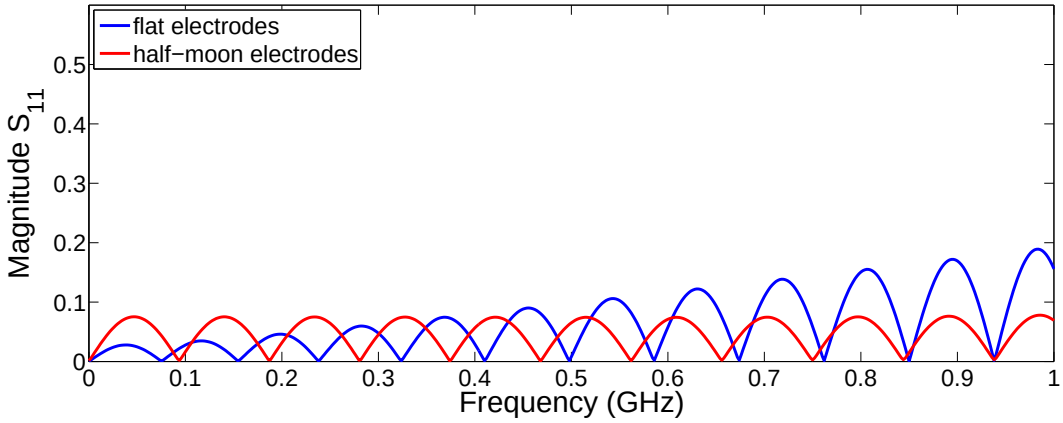

Figure 3.27: Even mode S_{11} parameter numerically calculated for flat electrodes (blue) and half-moon electrodes (red).

half-moon electrodes, the stripline beam pipe radius is smaller than for flat electrodes and, therefore, the electrodes are closer to the beam pipe, which makes the transition between the feedthrough and the electrode shorter and improves the reflection parameter. In the even mode, the same magnitude of the S_{11} parameter would be expected, since both geometries have a characteristic impedance of 50 Ω in the even mode. However, the effect of the unknown characteristic impedance of the transition between the feedthrough and the electrode plays an important role: for half-moon electrodes the magnitude of the reflection parameter keeps constant at a maximum value of ≈ 0.07 in the whole frequency range analyzed, whereas for flat electrodes the S_{11} parameter grows up from ≈ 0.03 to ≈ 0.2. The good stability of the S_{11} parameter in both operation modes for half-moon electrodes, makes this electrode shape more suitable from the beam impedance point of view: the beam excites high frequencies in the striplines,

and the growth of the S_{11} parameter at high frequencies for flat electrodes would create higher resonances than in the case of the half-moon electrodes.

The frequency range where the transmission is expected to be good depends on the pulse frequency content, therefore, only frequencies below 10 MHz have to be considered to guarantee a good transmission of the pulse through the kicker, as shown in Fig. 3.28. In this respect, a reflection parameter below 0.1 is usually a good design consideration from the power supply point of view [**?**].

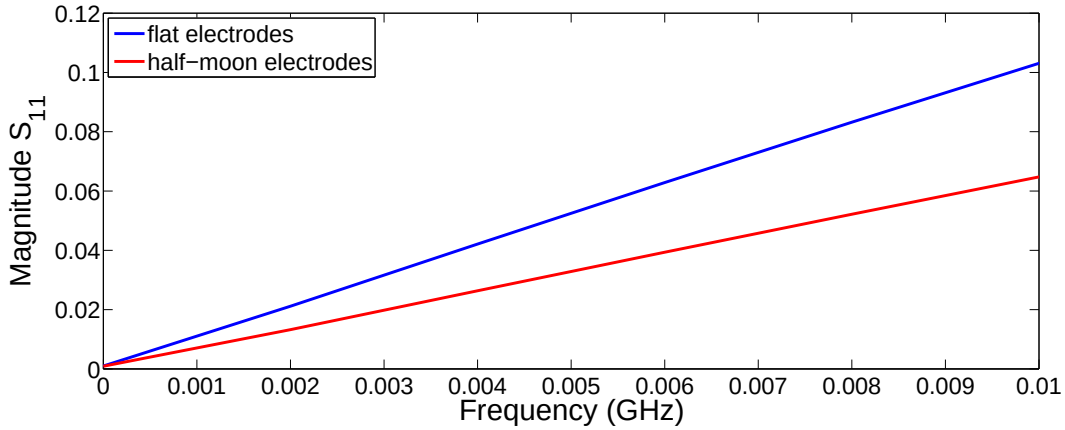

Figure 3.28: Odd mode S_{11} parameter, up to 10 MHz, for flat electrodes (blue) and half-moon electrodes (red).

Settling Time

The inductive adder is considered to generate trapezoidal pulses of rise time T_r, as shown in Fig. 3.4. Impedance mismatches create reflections and thus ripple. The time for the ripple to reduce within specification (± 0.02%) is called the settling time, and is measured from the end of the rise time. Settling time increases the required pulse width, thus increasing power dissipation and cross-sectional area of magnetic material. Hence the aim is to limit settling time (T_s) such that is no more than 100 ns.

Fig. 3.29 shows the predicted settling time versus odd mode characteristic impedance of the electrodes, by using the simulation program Personal Simulation Program with Integrated Circuit Emphasis (PSpice) [64], for different 0% to 100% rise times of the output pulse of the inductive adder. For these simulations the output pulse is modeled as being trapezoidal. Furthermore, the inductive adder and coaxial cable to striplines have a total single way delay of 13 ns, whereas the striplines, modelled as an ideal transmission line with a defined characteristic impedance, have a single way delay of 7 ns. The faster the rise time of the output pulse, from the inductive adder, in general the longer is the settling time. For flat electrodes, an odd mode characteristic impedance of 36.8 Ω results in a settling time of 113 ns for a rise time of the output pulse, from the inductive adder, of 100 ns. For the same rise time, a settling time of

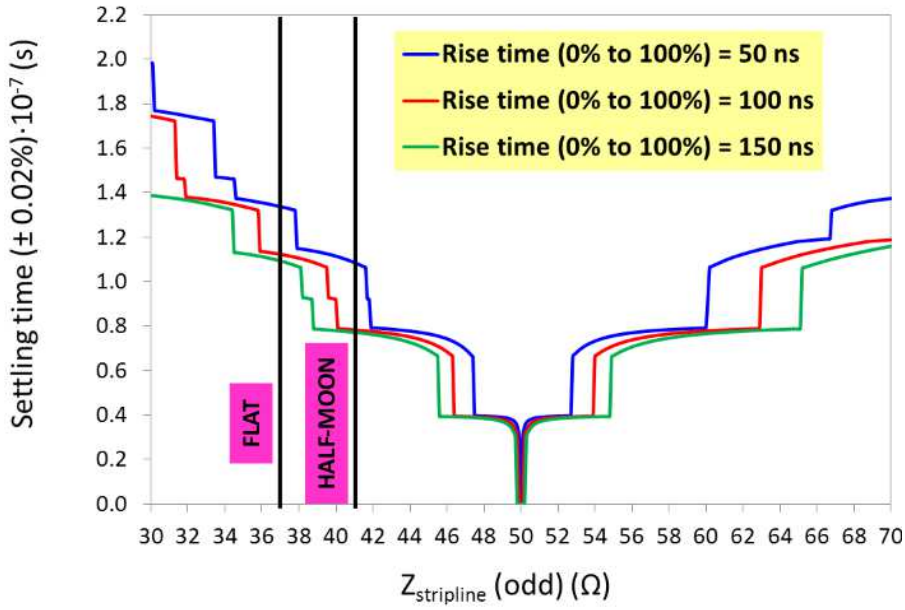

Figure 3.29: Settling time of the stripline voltage pulse as a function of stripline impedance for different 0% to 100% rise times of the output pulse of the inductive adder. The inductive adder, transmission line and terminating resistor impedances are 50 Ω [65].

78 ns will result when the odd mode characteristic impedance is 40.9 Ω, which is the case for the half-moon electrodes. Therefore, half-moon electrodes allow for a reduced settling time, which is beneficial for the design of the inductive adder.

Beam Coupling Impedance for Stripline Kickers

The stripline kickers for beam injection and extraction are expected to be one of the highest individual contributor to the impedance budget in CLIC DRs. Knowledge of the electromagnetic interactions, between the charged particle beam and the vacuum chamber, is necessary in order to avoid the instability phenomena that may otherwise occur in the the DRs.

The CST Particle Studio (PS) solver has been used to numerically calculate the beam coupling impedance of the striplines. CST PS is a 3D solver for the analysis, in time domain, of the charged particle dynamics in 3D electromagnetic fields. The simulation results for the longitudinal and transverse (horizontal) beam impedance, for both flat and half-moon electrodes shapes, have been compared with the analytical results from Eq. (3.34) and (3.41). For the proposed striplines of approximately 1.6 m length, the even mode characteristic impedance (Z_{even}) is 50 Ω, whereas the odd mode characteristic impedance (Z_{odd}) is 36.8 Ω and 40.9 Ω, for the flat and half-moon electrodes, respectively. The longitudinal and transverse geometric factors, $g_{\parallel}$ and $g_{\perp}$ have

been calculated with the 2D electrostatic solver Quickfield [66], driving the two electrodes with a positive-positive and positive-negative unit potential, respectively. For flat electrodes, $g_{\parallel} = 0.93$ and $g_{\perp} = 1.00$, whereas for half-moon electrodes, $g_{\parallel} = 0.85$ and $g_{\perp} = 1.00$.

The beam coupling impedance has been studied by using the same models as for the S_{11} parameter calculation, shown in Fig. 3.25. An ultrarelativistic beam with gaussian bunches of 50 mm length has been added to the model, and the same mesh definition as in CST MWS has been used, i.e. 25 lines per wavelength. A model without electrodes, only the beam pipe, has been first simulated in order to see the effect of the beam pipe geometry change over both the longitudinal and the transverse beam coupling impedance. Results for the longitudinal beam coupling impedance variation when taking into account the effect of the beam pipe are shown in Fig. 3.30, for flat and half-moon electrodes. The transverse beam coupling impedance is not significantly affected by the beam pipe geometry, since the geometry variation occurs in the longitudinal plane.

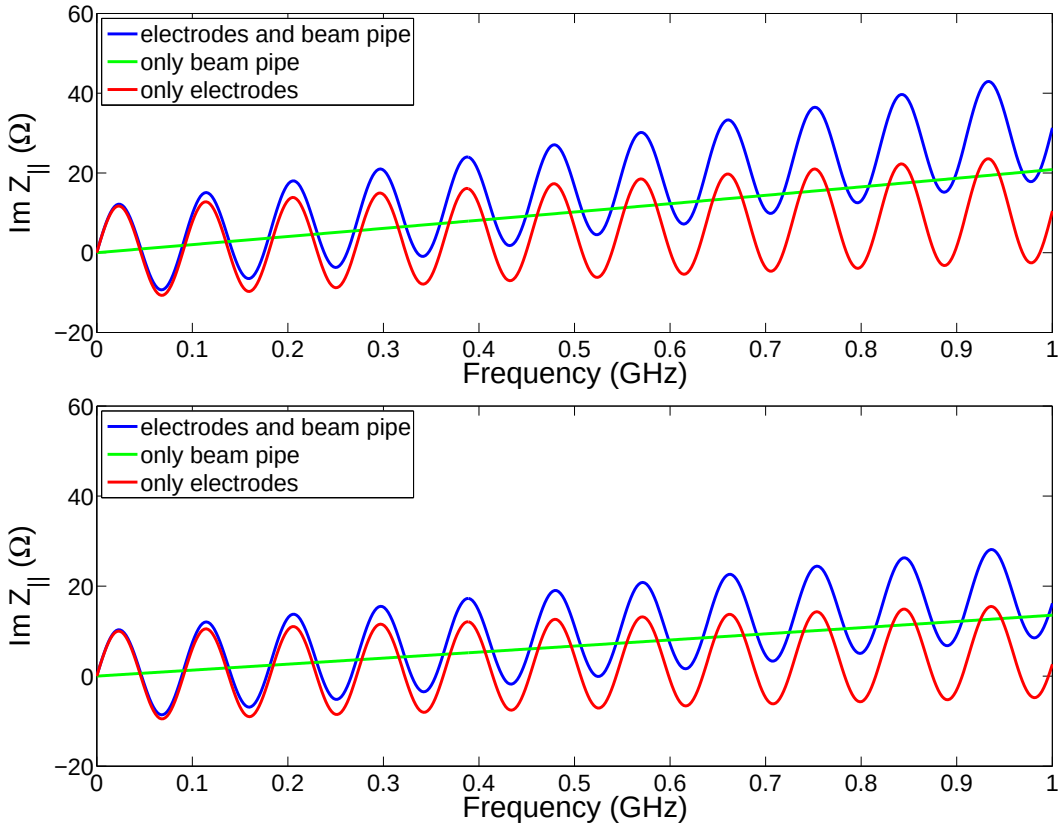

Figure 3.30: Effect of the beam pipe geometry change over the imaginary part of the longitudinal beam coupling impedance for flat electrodes (top) and half-moon electrodes (bottom).

The imaginary part of the longitudinal beam coupling impedance is affected by the

beam pipe geometry variation at frequencies above 200 MHz. For half-moon electrodes the effect is smaller, as it was expected from Fig. 3.27, where a good stability at high frequencies for the S_{11} parameter in the even operation mode is shown. The results shown in Fig. 3.30 must be substracted from the simulation results of the imaginary longitudinal beam coupling impedance. The comparison between the CST PS simulation results and the analytical equations for both flat and half-moon electrodes are shown in Fig. 3.31 for the longitudinal beam coupling impedance, and in Fig. 3.32 for the transverse (horizontal) beam coupling impedance.

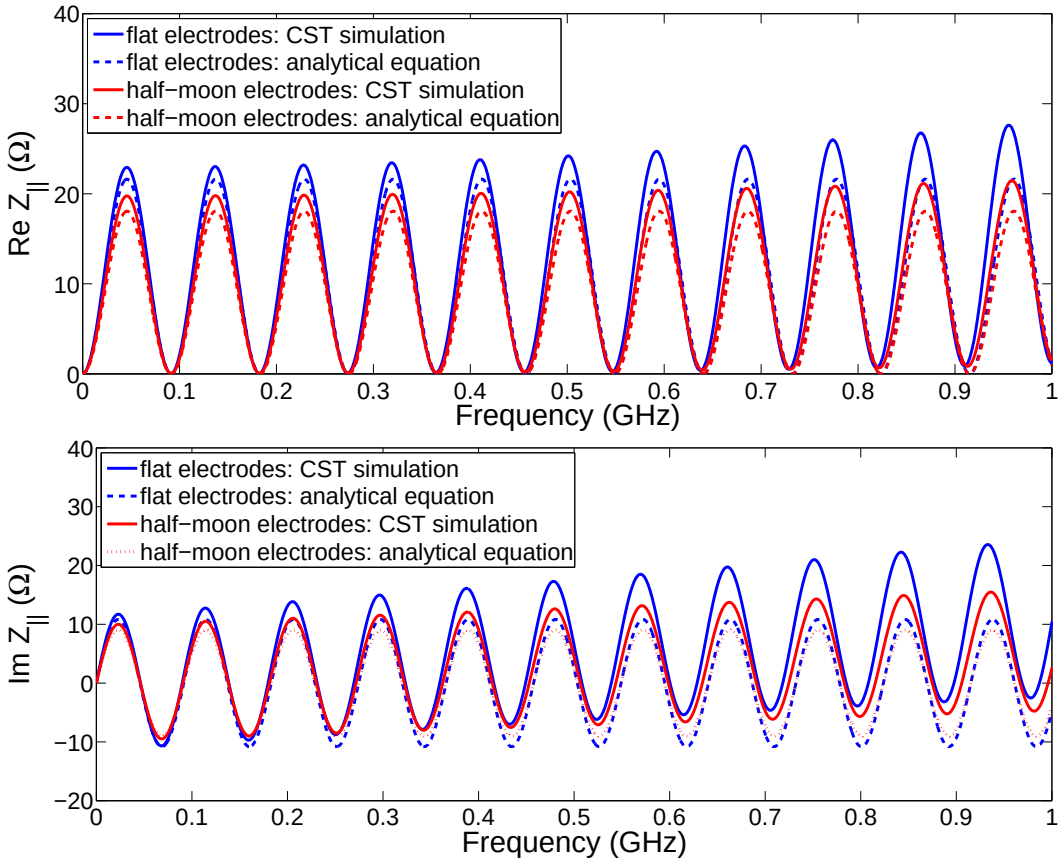

Figure 3.31: Real (top) and imaginary (bottom) part of the longitudinal beam coupling impedance calculated by Eq. (3.34) (dashed lines) compared with the results from the simulations (solid lines), for flat electrodes (blue) and half-moon electrodes (red).

From the longitudinal beam coupling impedance point of view, both the real and imaginary part agrees quite well with the analytical results from Eq. (3.34): the differences are due to the transitions, which are not taken into account in the analytical equation. Half-moon electrodes show a better behaviour than flat electrodes, due to the smaller longitudinal geometric factor for half-moon electrodes. To decrease $Z_{\|}$ at high frequencies, tapered electrodes are generally used, but for electrodes with a length of the order of cm. However, for striplines with a length of 1.6 m, the manufacturing of

the tapers is very complicated. In this sense, another advantage of the half-moon electrodes is that the growth of the longitudinal beam coupling impedance with frequency is very slow, compared with the growth for flat electrodes, making this electrode shape more suitable at high frequencies.

The horizontal transverse impedance can be calculated by using Eq. (3.41). This equation corresponds to the dipolar component of the horizontal beam coupling impedance [67]. The dipolar component of the horizontal impedance can be also numerically calculated with CST, by displacing the beam in the horizontal plane, while keeping the wake integration path at the center of the aperture. A comparison of the analytical results with the CST simulations of the dipolar horizontal impedance are shown in Fig. 3.32.

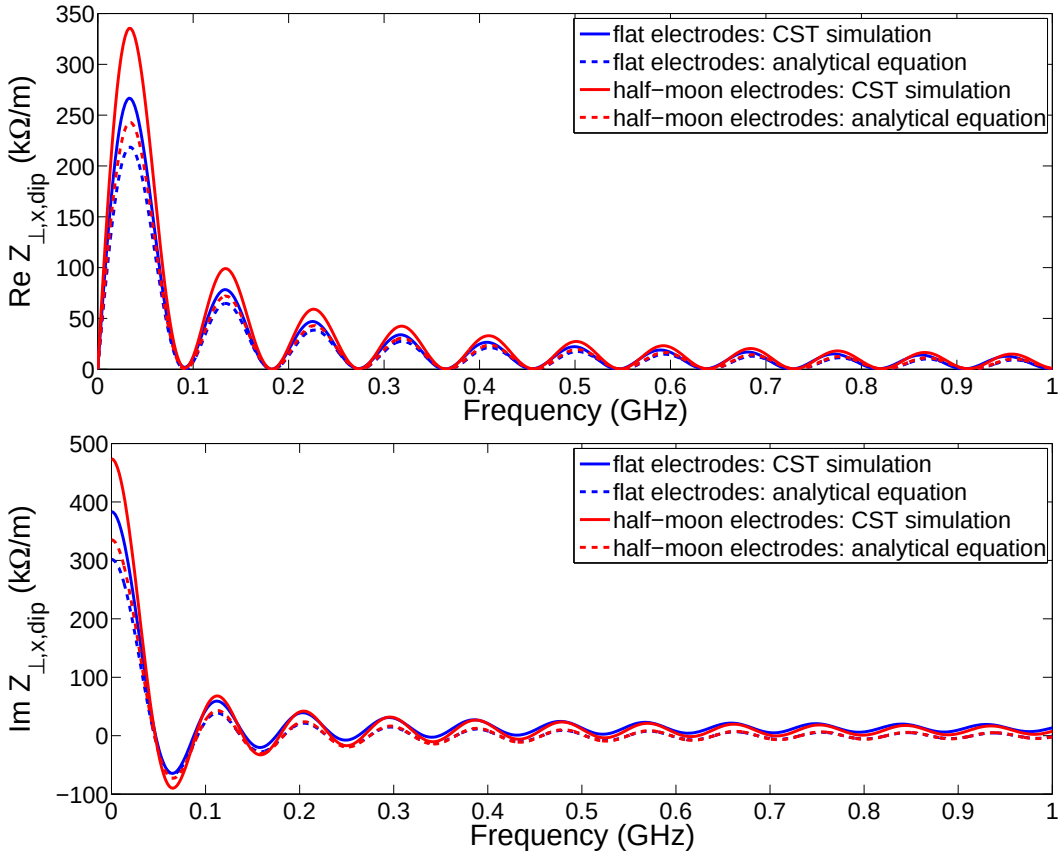

Figure 3.32: Real part (top) and imaginary part (bottom) of the dipolar horizontal beam coupling impedance calculated by Eq. (3.41) for flat electrodes (blue) and half-moon electrodes (red), compared with CST simulations.

The dipolar horizontal impedance is higher in the case of half-moon electrodes, for both analytical and numerical results, due to the fact that the odd mode characteristic impedance and the transverse geometric factor are higher in the case of half-moon electrodes. As in the longitudinal case, the difference between the simulations and the

analytical expressions are thought to be due to the transitions between the electrodes and the feedthroughs, which are not taken into account in the analytical expressions.

The dipolar component of the horizontal impedance is the main contribution to the total horizontal impedance for ultrarelativistic beams. Nevertheless, the quadrupolar horizontal impedance has been numerically calculated with CST, in order to have a better estimation of the total horizontal impedance, which is the sum of the dipolar and the quadrupolar components. To simulate the quadrupolar component of the horizontal impedance, the beam has been kept at the center of the striplines, whereas the wake integration path has been displaced in the horizontal plane. The total horizontal impedance has been calculated with CST as well, by displacing both the beam and the wake integration path in the horizontal plane, to see if it really corresponds to the sum of the dipolar and the quadrupolar components for the CLIC striplines. Results are shown in Fig. 3.33

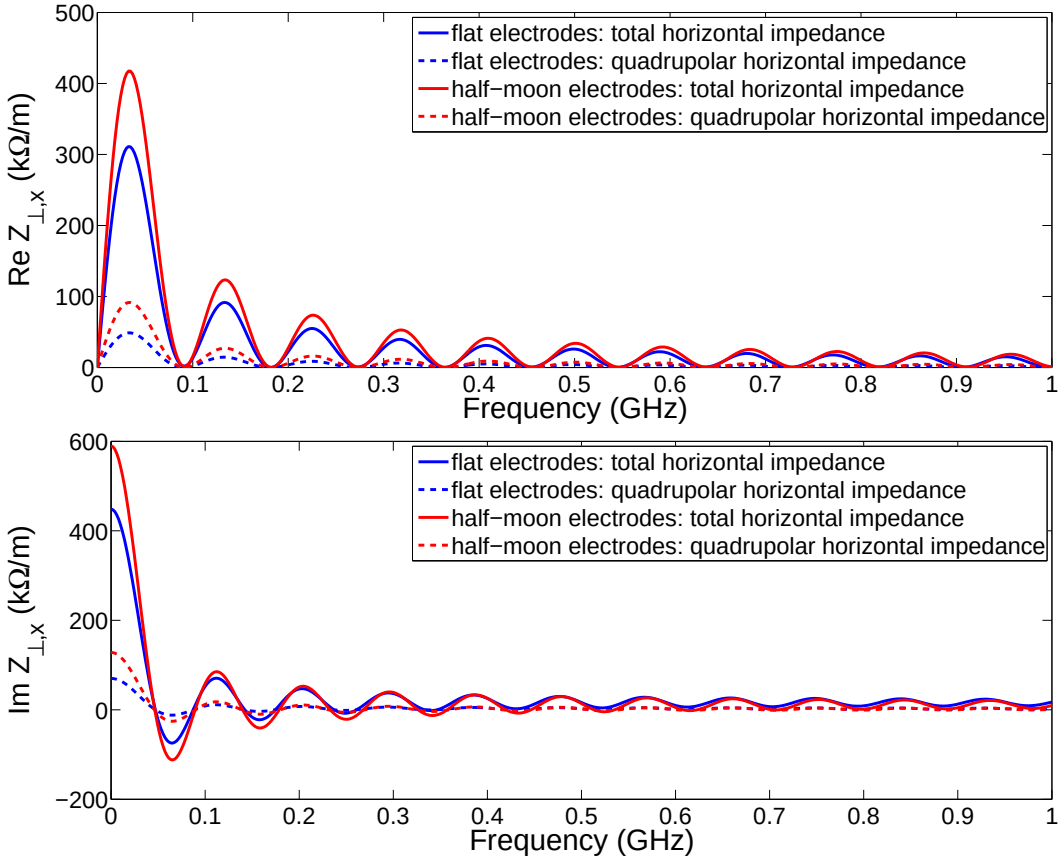

Figure 3.33: Real part (top) and imaginary part (bottom) of the quadrupolar (dashed lines) and total (solid lines) horizontal beam coupling impedance numerically calculated with CST for flat electrodes (blue) and half-moon electrodes (red).

Results show that the dipolar component of the horizontal impedance is much larger than the quadrupolar horizontal impedance, as was expected. The quadrupolar

horizontal impedance is also higher in the case of half-moon electrodes. Furthermore, it is confirmed that the total horizontal impedance corresponds to the sum of the dipolar and the quadrupolar components.

For CLIC DRs the most critical impedance will be the vertical one, because the average beta function in the horizontal plane is about one third of the average beta function in the vertical plane. Furthermore, the contribution of the wigglers to the vertical impedance is very high and takes an important part of the transverse impedance budget in the vertical plane [19]. The vertical impedance for horizontal striplines is expected to be zero [57, 58]. However, as it was seen in the case of the horizontal impedance, an effect of the transitions is expected: for that reason, the vertical impedance has been simulated by displacing the beam and the wake integration path in the vertical plane. Results are shown in Fig. 3.34 and Fig. 3.35, for the real part and the imaginary part of the vertical impedance, respectively. For both geometries, the dipolar and quadrupolar components of the vertical beam coupling impedance are the same, and equal to the quadrupolar component of the horizontal impedance. Taking into account that there are no electrodes in the vertical plane, this result may be due to the transition between the beam pipe of 20 mm diameter and the striplines beam pipe of 40.5 diameter, and the transition between the striplines beam pipe and the striplines aperture of 20 mm diameter, that would affect both the horizontal and the vertical beam coupling impedance [68]. Further studies of the contributions to the vertical impedance of the striplines must be done.

At very low frequencies, the longitudinal and the total transverse beam coupling impedance are inductive, i.e purely imaginary. Results are collected in Table 3.4.

	[Unit]	**Flat electrodes**	**Half-moon electrodes**
$Z_{\parallel}$/n	[Ω]	0.51	0.45
$Z_{\perp,x,dip}$	[kΩ/m]	383.4	473.9
$Z_{\perp,x,quad}$	[kΩ/m]	70.0	128.2
$Z_{\perp,x,tot}$	[kΩ/m]	448.5	589.8
$Z_{\perp,y,dip}$	[kΩ/m]	55.0	130.7
$Z_{\perp,y,quad}$	[kΩ/m]	73.6	136
$Z_{\perp,y,tot}$	[kΩ/m]	139.9	276.9

Table 3.4: Summary of the results for longitudinal and transverse beam coupling impedances for low frequencies.

Half-moon electrodes have a lower longitudinal beam coupling impedance, due to the smaller longitudinal geometric factor. The transverse impedance, both horizontal and vertical, are smaller in the case of the flat electrodes due to its smaller odd mode characteristic impedance. To have a longitudinal and transverse impedance below the impedance budget, a very small longitudinal and geometric factor would be required: this would turn out in a very low shunt impedance. Therefore, the possibility of increasing the impedance budget should be considered.

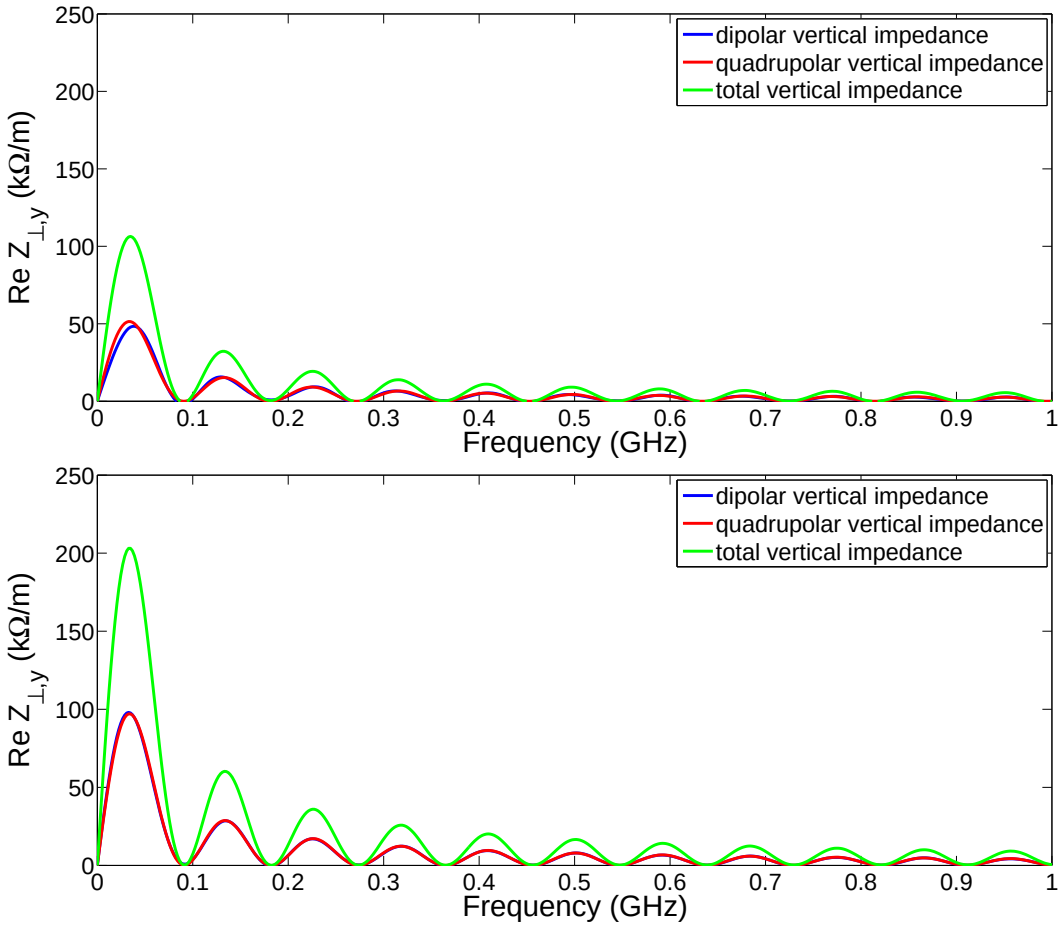

Figure 3.34: Real part of the vertical beam coupling impedance for flat electrodes (top) and half-moon electrodes (bottom.)

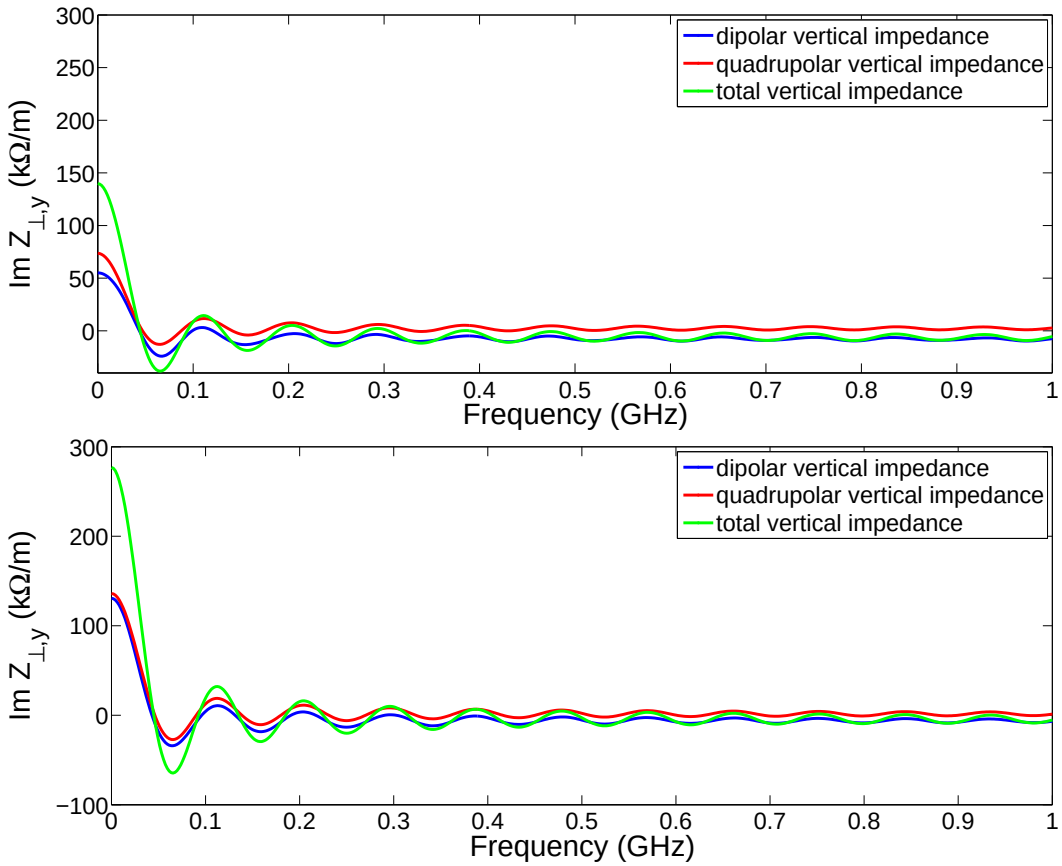

Figure 3.35: Imaginary part of the vertical beam coupling impedance for flat electrodes (top) and half-moon electrodes (bottom).

The relatively low frequency regime of the impedance studied in this section could be enough to address coupled bunch instabilities, which corresponds to a frequency up to 1 or 2 GHz. Knowledge of the beam coupling impedance (broadband impedance) at frequencies corresponding to the bunch length, of the order of hundreds of GHz, will be required in order to take into account single bunch instabilities –but this is outside the scope of this thesis.

3.4.3 Discussion and Choices of the Striplines Geometry

Studies of the cross-section of the striplines for the extraction kicker of the CLIC DRs have shown that for a 50 Ω even mode characteristic impedance of the striplines and the field homogeneity required, the half-moon electrode shape results in an odd mode characteristic impedance closer to 50 Ω than the flat electrodes: this results in a lower S_{11} parameter for the half-moon electrodes, as shown in Fig. 3.26 and Fig. 3.28, and a reduced settling time (Fig. 3.29), which is very important from the inductive adder point of view. In the even mode, the S_{11} parameter is lower for flat electrodes at

low frequencies; however, at high frequencies the half-moon electrodes shows a better behaviour (Fig. 3.27), due to the stability of the peaks amplitude. This will help to minimize resonances produced by the beam at high frequencies.

On the other hand, simulations of beam coupling impedance have shown that the longitudinal beam coupling impedance is lower for the half-moon electrode at low frequencies, as expected for the lower longitudinal geometric factor in this case, and keeps its value almost constant over the frequency range considered, whereas the longitudinal beam coupling impedance increases significantly with frequency for flat electrodes, as shown in Fig. 3.31. The flat electrode shape is better from the transverse beam coupling impedance point of view, as expected from the lower odd mode characteristic impedance. Only the vertical impedance achieved with flat electrodes is below the impedance budget, however this transverse impedance budget has been calculated taking into account the contribution to the beam coupling impedance of all the systems composing the DR: the transverse impedance budget for the extraction kicker is assumed to be 2% of the impedance allowance. Therefore, a relaxation in this impedance budget could be required.

Half-moon electrodes have another advantage from the manufacturing point of view: the moment of inertia is larger for half-moon electrodes, due to the increase of the thickness for this electrode shape. The uniformity of the electromagnetic field at the centre of the striplines aperture depends on the perfect parallelism between the two electrodes, and the resistance to possible twists increases with the moment of inertia. Furthermore, the smaller radius of the rounded edges in the case of the half-moon electrodes helps to increase this resistance.

A summary of all the parameters considered for the choice of the striplines for beam extraction from the CLIC DRs is shown in Table 3.5.

Parameter	**Flat electrodes**	**Half-moon electrodes**
Field homogeneity	+	+
S_{11} parameter	-	+
Longitudinal beam coupling impedance	-	+
Transverse beam coupling impedance	+	-
Manufacturing considerations	-	+

Table 3.5: Summary of all the paramters considered to compare flat and half-moon electrodes.

Overall, although with the two electrode shapes the excellent field homogeneity required is achieved, the half-moon electrodes have (1) lower odd mode S_{11} parameter, which helps to reduce the pulse settling time, (2) lower even mode S_{11} parameter at high frequencies, minimizing the resonances due to the beam, that mainly occur at high frequencies, (3) lower longitudinal beam coupling impedance, being significantly lower than flat electrodes at high frequencies, and (4) higher moment of inertia and, hence, higher resistance to possible twists during manufacturing. Only the transverse beam coupling impedance is larger in the case of flat electrodes. Therefore, after this

study, half-moon electrodes were considered as the best choice for the cross-section of the striplines for the extraction kicker of the CLIC DRs.

Most of these results for the design study presented in this chapter, as well as the study of the electrode supports and feedthroughs, that will be explained in Chapter 4, has been published in the Physical Review Special Topics -Accelerators and Beams (PRSTAB) [69].

3.5 High-Frequency Calculations for the Optimum Striplines

3.5.1 Analysis of Trapped Higher Order Modes

The stripline kicker has an impedance function consisting of a large number of resonant peaks, as it has been shown in Section 3.4.2. These are mainly due to trapped modes, i.e. resonances with frequencies below the lowest cut-off frequency of the beam pipe. Coupled-bunch instabilities depend mainly on narrow resonances at frequencies below or near the cut-off of the beam pipe. Above this frequency, the electromagnetic fields can propagate out of a structure and thus will not build up resonantly, unless they are reflected back by adjacent cross-section variations. However, resonances at higher frequencies may also appear. Single-bunch instabilities depend on the short range wakefields, corresponding to wide-band impedances which occur mostly at higher frequencies [55].

In CLIC DRs, for single bunch instabilities the frequency range of interest corresponds to hundreds of GHz (related with the bunch length: 1.6 mm for 1 GHz baseline), but nowadays these high frequencies are not affordable by running a simulation code such as CST PS in a single computer. For coupled bunch instabilities, the frequencies of interest are related with the striplines cut-off frequency. If considering the fundamental TEM mode of propagation in a coaxial line, which has no cut-off frequency, the electric and magnetic field lines in the transverse plane are perpendicular to the direction of energy propagation. Besides the TEM mode, a coaxial line can support various non-TEM modes, called Higher Order Modes (HOMs). Such modes are referred to as TE_{mn} and TM_{mn} modes. For a coaxial line, TE_{11} and TM_{01} are the two first HOMs above the fundamental TEM mode, and the cut-off frequencies of these modes are given by [45]:

$$f_c(TE_{11}) = \frac{c}{\pi(a+b)} \tag{3.48}$$

$$f_c(TM_{01}) = \frac{c}{2(a-b)} \tag{3.49}$$

where a is outer radius and b the inner radius of a coaxial line. In the case of the stripline kicker, the operation modes are two quasi-TEM modes (odd and even). When

approximating the striplines with a coaxial line of inner radius the striplines aperture, and outer radius the beam pipe radius, the first two HOMs, TE_{11} and TM_{01}, could be expected at 3.2 GHz and 15 GHz, respectively.

To calculate the HOMs of a resonant cavity, the Eigenmode Solver of CST MWS is widely used, which is dedicated to the simulation of closed resonant structures. The simulation results show up the resonant modes trapped in the structure, as well as the R/Q and the Q parameters of each resonant mode. R/Q is a geometrical factor which relates the voltage applied to a cavity with the stored energy inside the cavity, whereas the Q-factor depends on the material and informs about the magnitude of the interaction of the resonant mode with the beam. Several simulations must be done in different ranges of frequencies up to 3.2 GHz in order to find the first HOM corresponding to the TE_{11} mode. However, due to the dimensions of the stripline kicker (1.7 m), a very large number of cells is required, becoming a challenging analysis from the computer power requirements point of view. For that reason, the studies presented in this thesis are done up to 1 GHz. Nevertheless, it could be an important issue to take into account in future studies.

3.5.2 Electrodes Heating Study

Beam coupling impedance is a critical issue in many high intensity particle accelerators, not only because the longitudinal and transverse impedance may drive beam instabilities and cause undesired tune shifts, but the real part of the longitudinal impedance also gives rise to power dissipation in the component. For high intensities this may cause significant heating. The power lost can be calculated by means of numerical simulations.

The total power P_b lost by the beam due to the wakefields of N_b equally spaced bunches can be obtained by using the relation [70]:

$$P_b = I^2 \sum_{n=-\infty}^{\infty} ReZ_{\|}|S|^2 \tag{3.50}$$

where S is the single bunch spectrum, $ReZ_{\|}$ is the real part of the longitudinal component of the beam coupling impedance (both the geometrical and the resistive wall components), $I = N_b Q/T_0$ is the average beam current with Q the bunch charge, and $T_0 = 2\pi\omega_0$ is the revolution period.

A simplified expression of Eq. (3.50) can be obtained when N_b times the revolution frequency f_0 is much smaller than the inverse of the bunch duration $c/(\sqrt{2}\pi\sigma_z)$, where c is the speed of light. Under these conditions the multibunch spectrum can be approximated by the single bunch spectrum and, in absence of resonant modes, Eq. (3.50) becomes:

$$P_b = \frac{I^2 T_0}{N_b} k_l \tag{3.51}$$

where k_l is the loss factor. The longitudinal loss factor gives the energy lost by a beam and defines the power deposited in the beam pipe, and is given by:

$$k_l = \frac{1}{\pi}\int_0^{\infty} |S(\omega)|^2 ReZ_{\parallel}(\omega)d\omega \tag{3.52}$$

A Gdfidl [71] model of the striplines, without the electrode supports, has been studied in the ALBA synchrotron [72] in order to calculate the lost power by a beam of 3 GeV and a bunch length of 5 mm when passing through the aperture of the striplines [73]. Gdfidl is an electromagnetic field simulator, which computes electromagnetic fields in 3D-Structures using parallel or scalar computer systems, which makes easier to compute short bunch lengths, i.e. high frequencies. A power lost of 28.2 W was calculated for an average beam current of 0.2 A, and 80.6 W for an average beam current of 0.4 A. However, less than 1 W is expected to stay in the CLIC stripline, since the excited modes can escape easily through the feedthroughs [73].

The striplines operates in Ultra High Vacuum (UHV); for that reason, the heating dissipation is assumed to be done only by radiation, neglecting the heating dissipated by convection or conduction. From the equation of Stefan-Boltzmann, the net power loss by radiation is given by:

$$P = e\sigma\frac{A}{f}(T^4 - T_c^4) \tag{3.53}$$

where e is the emissivity of the material, σ is the Stefan-Boltzmann constant, A is the area of the electrode, f is the view factor, T is the temperature of the electrodes, and T_c is the temperature of the beam pipe walls. The view factor is defined as the fraction of radiation emitted by a surface that strikes directly another surface. If two concentric spheres are taken into account, all the radiation emitted by the smaller sphere arrives to the larger one. However, in the striplines case, the electrodes occupy an angle of 3.6 rad, instead of the 2π rad from a cylinder, therefore, the view factor has been calculated as $f = 3.6/2\pi = 0.57$. The most common material used in stripline kickers are aluminium, so taking the emissivity of the aluminium (roughly polished) to be around 0.18, an electrode area of 0,035 m^2, a temperature of the beam pipe of 293 K and 1 W of power loss, the temperature of the electrode can be calculated, which is 34 °C. Therefore, no dangerous heating of the electrodes is expected during the beam passing through the aperture of the striplines for ALBA beam parameters.

For the CLIC DRs, the bunch length is 1.8 mm or 1.6 mm, depending on the RF baseline. Taking into account the last results for a bunch length of 5 mm, and using Eq. (3.51), the power dissipated in the striplines for the CLIC DRs beam parameters can be estimated. The power dissipated for a 0.2 A beam current produced by 10 trains of 32 bunches each, and a revolution period of $T_0 = C/c = 0.9\mu s$, where C = 260 m is the ALBA storage ring circumference, is 28.2 W. For CLIC DRs, the average beam current is expected to be up to 0.17 A [19] with 1 train of 312 bunches, in the 1 GHz baseline, or 2 trains of 156 bunches, in the 2 GHz baseline. These values are very close to the calculated values for ALBA, the only difference is the revolution period, being

a factor 1.5 larger in the case of CLIC DRs, $T_0 = 1,4\mu s$, since the ring circumference is C = 427.5 m. Therefore, a total power dissipation of approximately 44 W has been calculated for the CLIC striplines. However, considering that the same fraction of power as in the ALBA case is dissipated via the feedthroughs, i.e. less than 1 W on the electrodes for a total dissipation of 28.2 W, the power contributing to the electrodes heating will be 1.5 W, which corresponds an electrode temperature of 41°C, and does not represent a problem from the vacuum point of view. The remaining 42.5 W would be dissipated in the terminators ($\approx$ 21 W per terminator).

Chapter 4

Components Study and Manufacturing Process of the Striplines Prototype

4.1 Introduction

The geometry chosen for the first stripline kicker prototype has been already obtained from analytical and numerical calculations, and consists of the optimized half-moon electrodes inside a cylindrical beam pipe of 20.25 mm inner radius, as it has been explained in Chapter 3. In order to characterize the stripline kicker performance, a 3D model of the striplines has been simulated by using CST, and the reflection parameter S_{11} as well as the longitudinal and transverse beam coupling impedance have been calculated, in all cases up to a frequency of 1 GHz. Nevertheless, the kicker operation can be strongly affected by some other components which has not been taken into account in this first study. In this chapter, a complete study of the striplines components that can also affect the reflection parameter and the longitudinal and transverse beam coupling impedance, i.e the electrode supports and the feedthroughs, will be presented. In addition, a summary of the manufacturing process of the first stripline kicker prototype, carried out by the Spanish company Trinos Vacuum Projects [43], will be reported.

4.2 Striplines Components Study

For a complete characterization of the striplines operation, a detailed study of the electrode supports and the feedthroughs must be done. Both components may create an impedance mismatch, which will increase the reflected power in the structure, as well as the beam coupling impedance. Electrode supports, which are commonly made up of a ceramic material, are required to keep the electrodes at the same position and parallel along their length. The electromagnetic behavior of the electrode

supports, which keeps the electrodes electrically insulated from the striplines beam pipe, has been studied by simulating the reflection coefficient over the full structure. The ceramic used for the electrode must feature good mechanical and dielectric properties at high frequencies, while keeping high vacuum compatibility. Furthermore, although commercial feedthroughs with a nominal characteristic impedance of 50 Ω will be used, an impedance mismatch will appear in the point where the feedthrough is connected to the electrode, and the effect of this impedance mismatch upon both the reflection parameter and the beam coupling impedance must be also taken into account.

4.2.1 Study and Optimization of Electrode Supports

The maximum total length specified for the stripline kicker for CLIC DRs is 1.7 m (Table 2.3). This length corresponds to the length of the striplines and the flanges: taking into account the flanges and the space required for the feedthrougs, the electrodes were finally considered to be 1.639 m long. Ideally, these electrodes must be perfectly aligned along their entire length. Cylindrical supports have been used in other stripline kickers with larger stripline beam pipe radius, such as the CTF3 extraction kicker where the inner radius of the stripline beam pipe was 40 mm [31]; however, in the CLIC DR design these supports will not be used, because it is not possible to achieve the required precision for the electrode alignment. In order to ensure the alignment a new solution has been proposed, which consists of fixing the electrodes outside the aperture by using equally-spaced ceramic rings made up of Macor [74]: this ceramic features suitable thermal and electrical properties, and can be manufactured in almost any shape with accurate dimensions. Ensuring the alignment of the striplines with the Macor rings before inserting the assembly into the beam pipe, has been the only way to ensure the excellent required field uniformity.

The number of Macor rings and their length has been selected by studying the mechanical requirements and the impedance mismatch introduced by the rings. This impedance mismatch introduced by the Macor rings results in power being reflected: the reflection parameter, in both odd and even modes, has been simulated using CST MS, as shown in Fig. 4.1, with ideal coaxial feedthroughs of 50 Ω characteristic impedance. As it was explained in Chapter 3, the 50 Ω characteristic impedance has been achieved by modeling a coaxial feedthrough of 1.8 mm inner radius and 4.1 mm outer radius. For these simulations, the Transient Solver with an hexahedral mesh of 25 lines per wavelength (approximately 200.000 mesh cells for the half-model) has been used. As it was explained in Chapter 3, only half of the model has been taken into account, by using a symmetry in the center plane between the two electrodes: an electric symmetry for the odd mode, and a magnetic symmetry for the even mode. In addition, the electrodes and the inner conductor of the feedthroughs are considered PEC, whereas the Macor rings have been defined with a relative dielectric permittivity of 5.67 [74].

A number of equally spaced Macor rings were considered in order to affix the

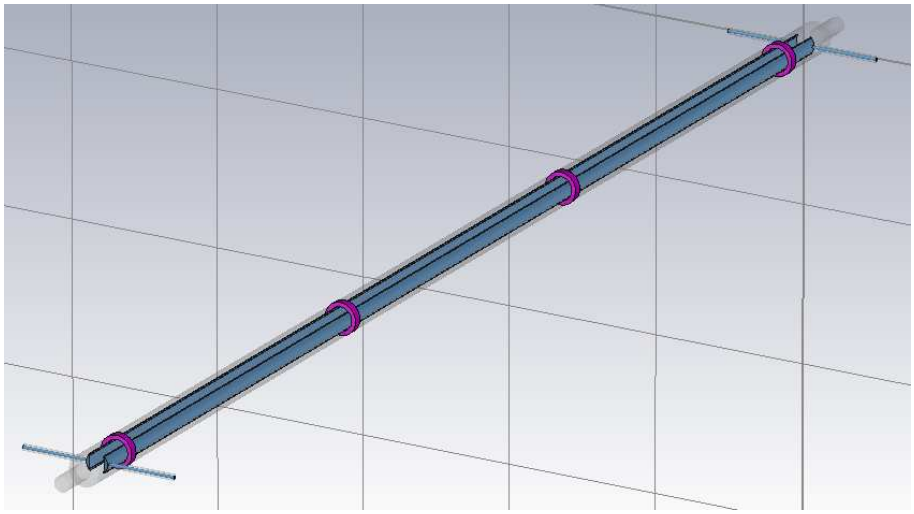

Figure 4.1: CST model used to simulate the striplines with four equally spaced Macor ring supports, and ideal 50 Ω feedthroughs.

electrodes to the striplines beam pipe, and the S_{11} parameter was studied for both odd and even modes, for three, four and five Macor rings. The results are shown in Fig. 4.2 for the odd mode (top) and the even mode (bottom).

For the odd mode (Fig. 4.2 (top)) the presence of the Macor rings increases the magnitude of the reflection parameter S_{11} of every second peak (for three rings), of every third peak (for four rings), and every fourth peak (for five rings), producing the frequency shift observed. The magnitude of the peaks is lower when decreasing the number of Macor rings. In the even mode, the maximum-minimum pattern found is the same as for the odd mode. Again, the lower the number of Macor rings, the lower the reflection magnitude. Therefore, from the electromagnetic point of view, the number of Macor rings should be as small as possible.

The length of the Macor ring considered up to now has been 8 mm. However, other lengths have been studied, in a range from 8 mm to 12 mm, in order to see the effect over the reflection parameter in both operation modes, for four Macor rings. As shown in Fig. 4.3, the magnitude of the S_{11} parameter increases when using longer Macor rings, for both operation modes.

With the results shown in Fig. 4.2 and Fig. 4.3, and after talking with the manufacturer company to take into account the mechanical requirements for keeping aligned the $\approx$ 2 m long electrodes with a thickness of $\approx$ 4 mm, the final choice for the electrode supports was four Macor rings, of 10 mm length each. For this geometry, the odd mode and even mode reflection parameteres are shown in Fig. 4.4. In the odd mode, the separation between the peaks corresponds to the distance, there and back, between the equally-spaced Macor rings ($\approx$510 mm). The frequency content of the driving pulse from the inductive adder will only extend up to approximately 10 MHz, when the considered pulse rise time is T_r = 100 ns. Thus, since the Macor rings mainly

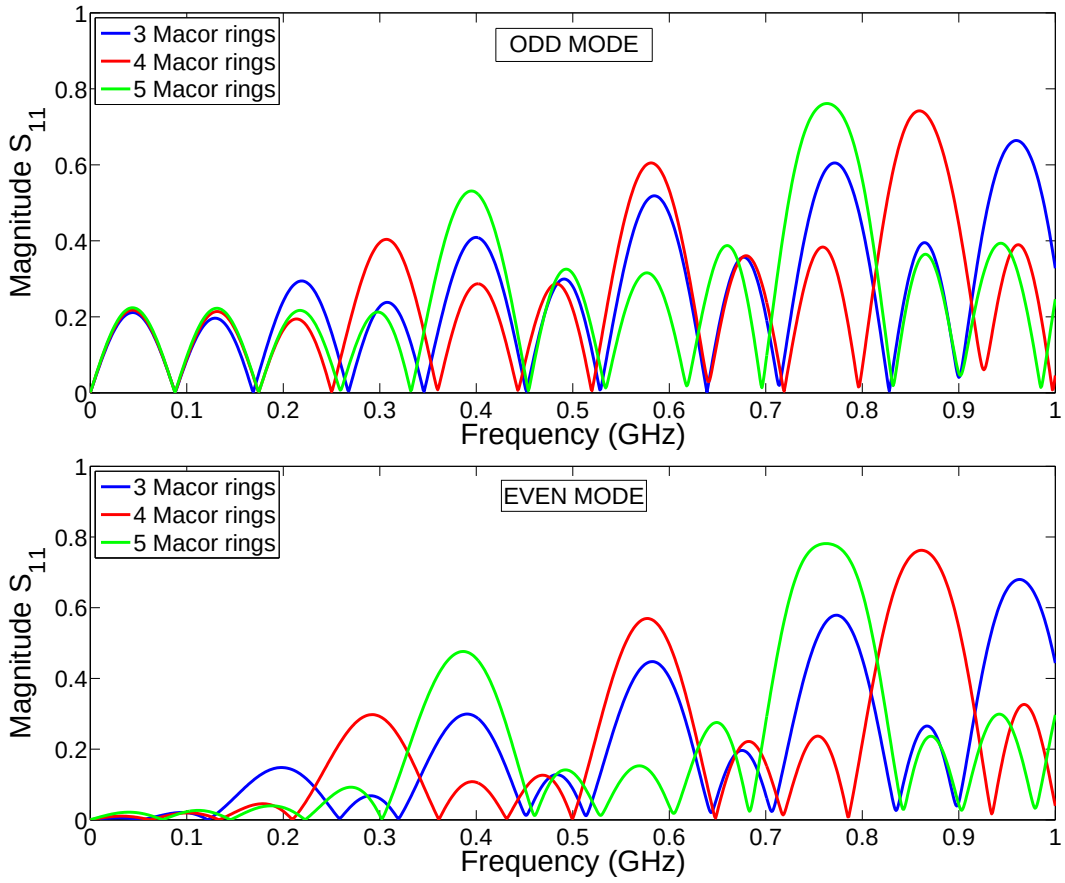

Figure 4.2: S_{11} parameter versus frequency for a different number of equally spaced Macor rings, for the odd mode (top) and the even mode (bottom).

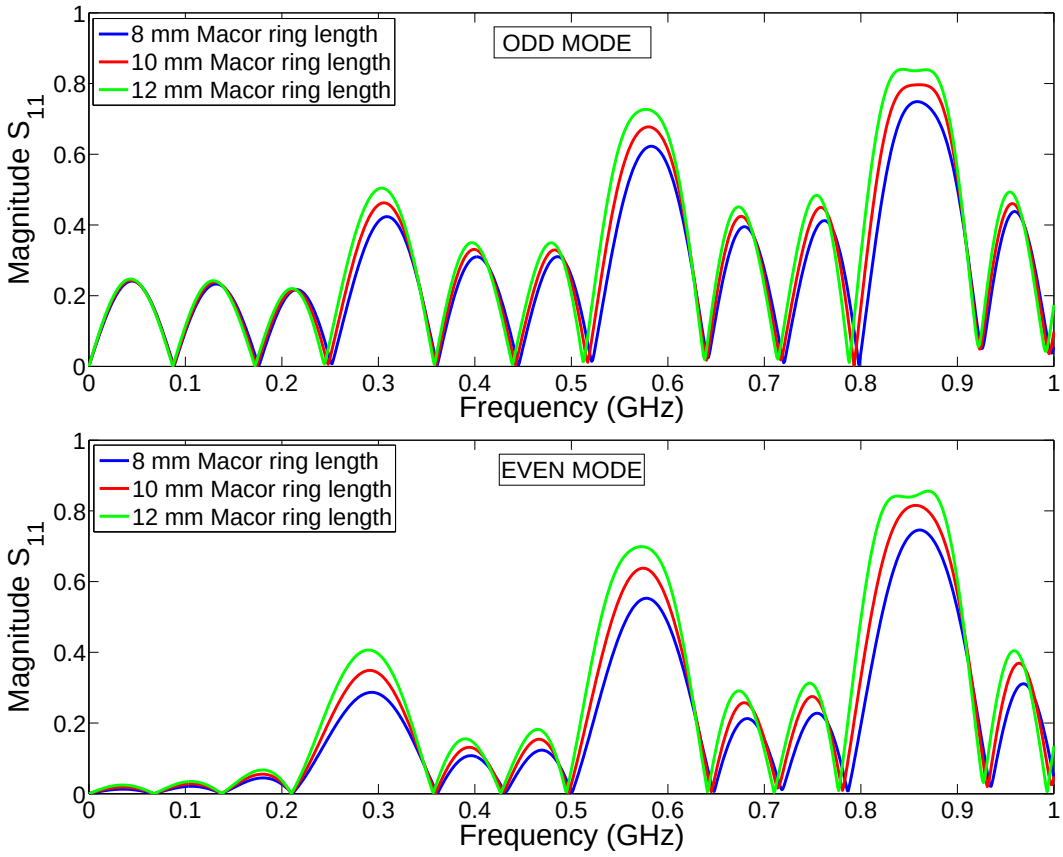

Figure 4.3: S_{11} parameter versus frequency for different lengths of equally spaced Macor rings, for the odd mode (top) and the even mode (bottom).

affect the S_{11} above ≈300 MHz, they are not expected to significantly influence the ripple of the driving pulse. However, the high resonances that appear in the even mode, also above ≈ 300 MHz, may increase the beam coupling impedance.

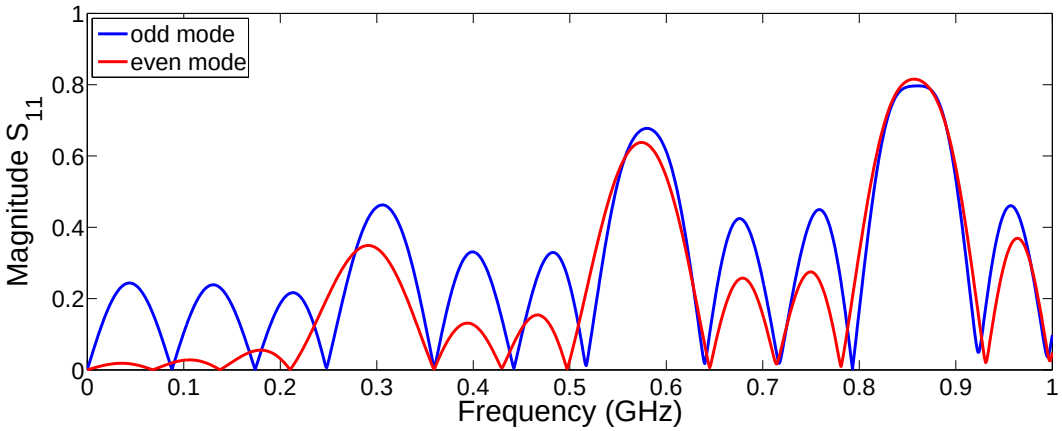

Figure 4.4: Magnitude of S_{11} predicted by CST MS, for striplines with four, equally spaced, 10 mm long Macor ring supports, in the odd mode (blue) and even mode (red).

To study the effect upon the beam coupling impedance, the Wakefield Solver of the CST PS has been used, with the same mesh settings as before (25 lines per wavelength) and a wakelength of 5 m. A relativistic particle beam of 50 mm bunch length, and with a transverse offset of 1 mm, has been defined. Results for longitudinal, horizontal and vertical beam coupling impedance are shown in Fig. 4.5 and Fig. 4.6. For horizontal impedance, the dipolar and the quadrupolar components are shown, and the total impedance is the sum of both components, as it was shown in Chapter 3.

The real part of the longitudinal beam coupling impedance is affected by the presence of the Macor rings, with a reduction of the impedance where the Macor rings are placed, whereas the transverse beam coupling impedance (Fig. 4.6) is not significantly affected because the Macor rings do not change the cross-section of the striplines (striplines beam pipe radius and aperture). The same effect has been observed in the vertical beam coupling impedance.

Finally, the presence of the Macor rings will also affect the uniformity of the electric field. HFSS simulations showed that the field inhomogeneity increases from ±0.008% to ±0.07% in the regions where the Macor is placed. Since the 4 rings are 10 mm long, the total length occupied by this ceramic is 40 mm, which corresponds to ≈2.5% of the total striplines length. Hence the field inhomogeneity over the 1 mm radius, integrated along the length of the striplines, is ±0.009%, which is within specification.

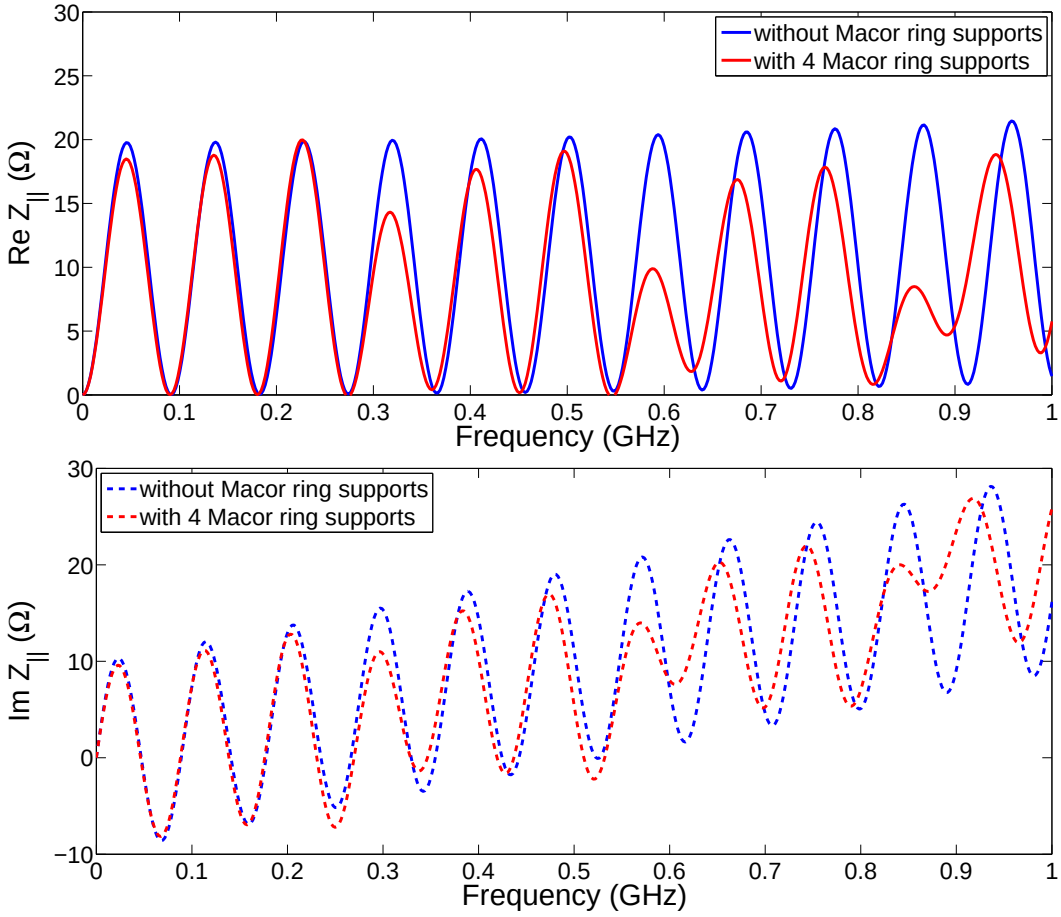

Figure 4.5: Real part (top) and imaginary part (bottom) of the longitudinal beam coupling impedance for striplines with four, equally spaced, Macor rings (red line) and without Macor rings (blue line).

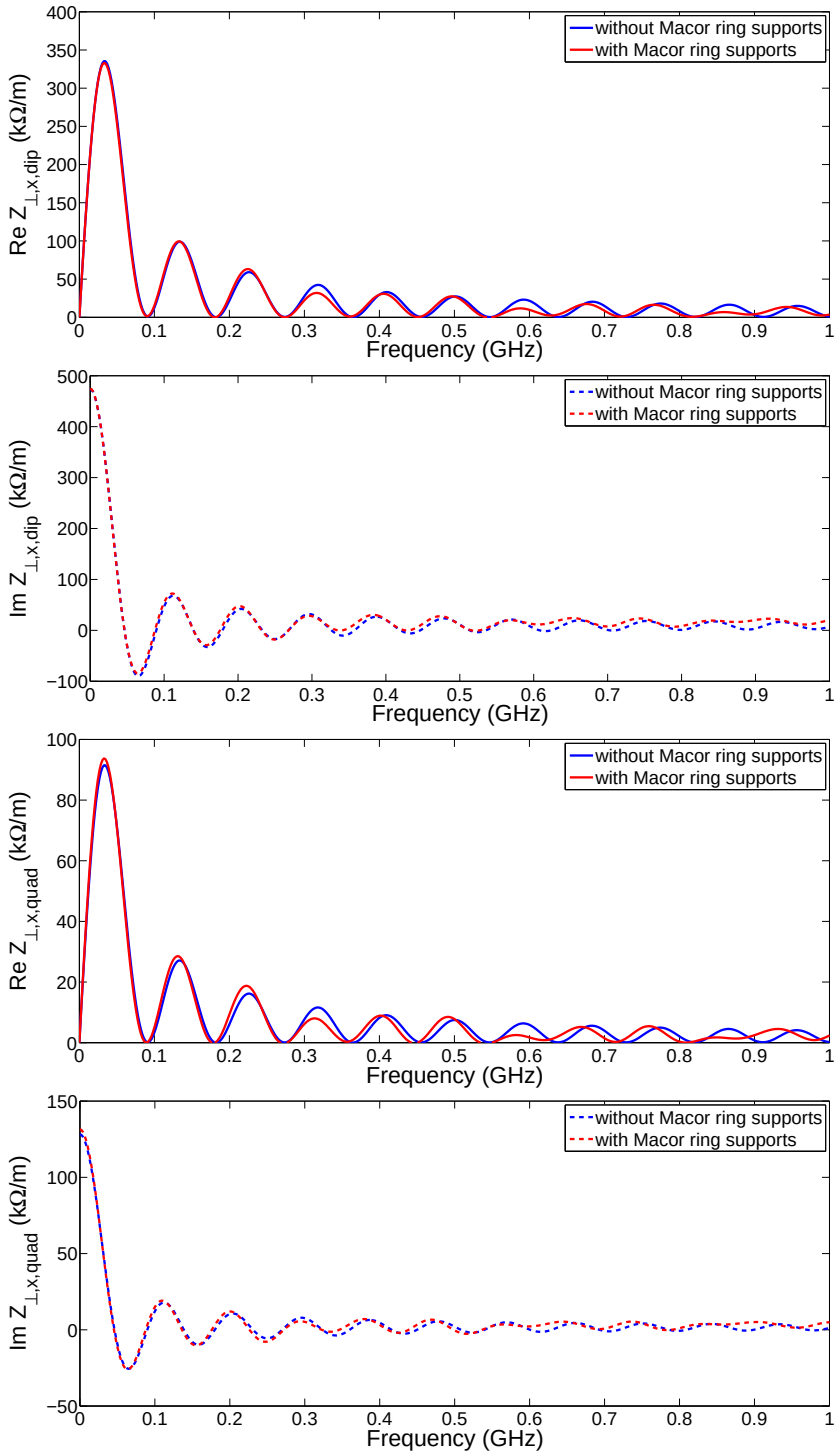

Figure 4.6: Real (solid lines) and imaginary (dashed lines) part of the dipolar (top) and quadrupolar (bottom) components of the horizontal beam coupling impedance for striplines with four, equally spaced, Macor rings(red line) and without Macor rings (blue line).

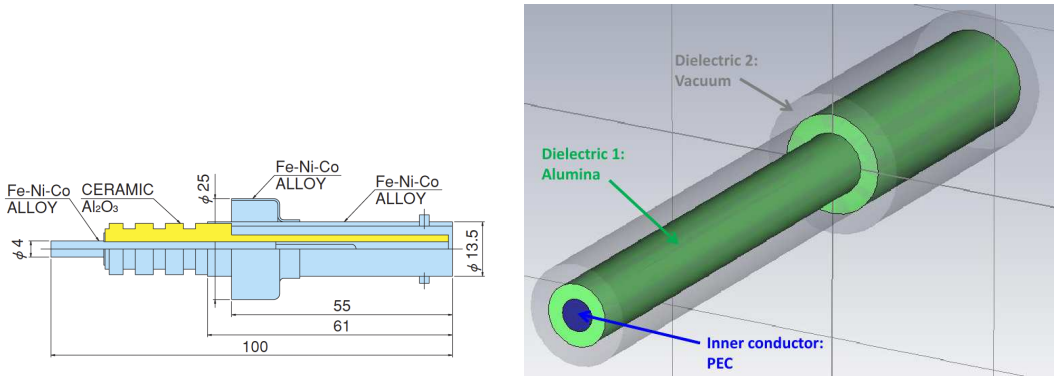

Figure 4.7: Schematic of one of the Kyocera feedthroughs [75] (left) and CST MWS model (right) used to connect the electrodes with the inductive adder and the loads.

4.2.2 Study and Optimization of Feedthroughs

A total of four feedthroughs will connect the stripline electrodes with the inductive adder and the two terminating resistors, as shown in Fig. 2.8. These feedthroughs should feature a constant characteristic impedance of 50 Ω.

For extracting the beam, the striplines will be driven with a voltage of ± 12.5 kV, therefore, when looking for commercial feedthroughs, the maximum allowed voltage as well as the vacuum specifications were taken into account. The 15kV-F-UHV (Ultra High Vacuum) feedthrough from Kyocera (Fig.4.7), can operate at DC with a maximum voltage of 15 kV, or at AC with a maximum frequency of 100 MHz, according to the manufacturer datasheet.

One of the most complex manufacturing issues is the design of the electrical contact between the feedthrough and the electrode. The current flowing through the electrodes heats them depending on the peak current of the pulse, the pulse duration, the repetition rate and the electrode resistivity. Therefore, a small linear expansion of the electrodes is always expected. This makes necessary the use of flexible contacts between the feedthrough and the electrode to avoid breaking the brazed ceramic inside the feedthrough due to excessive radial stress. In this case, the feedthrough pin should be connected via a flexible cable near to the end of the electrodes, which ensures the electrical contact, especially when baking out the striplines. The cable must be highly flexible to avoid possible breaking due to fatigue stress. It must also be as short as possible to maintain the characteristic impedance of the transition. To take into account the feedthrough and the connection, a new model with an approximation of the real feedthroughs has been simulated, as shown in Fig. 4.8, using Al_2O_3 (alumina) as a dielectric material with a relative dielectric permittivity of 9.4. The results were compared with the previous results for the ideal coaxial feedthroughs.

Figure 4.9 shows the S_{11} parameter for the odd mode (top) and the even (mode) with the simplified feedthroughs (blue line) and the real feedthroughs (red line). For this simulation, the mesh length has been increased up to 40 lines per wavelength

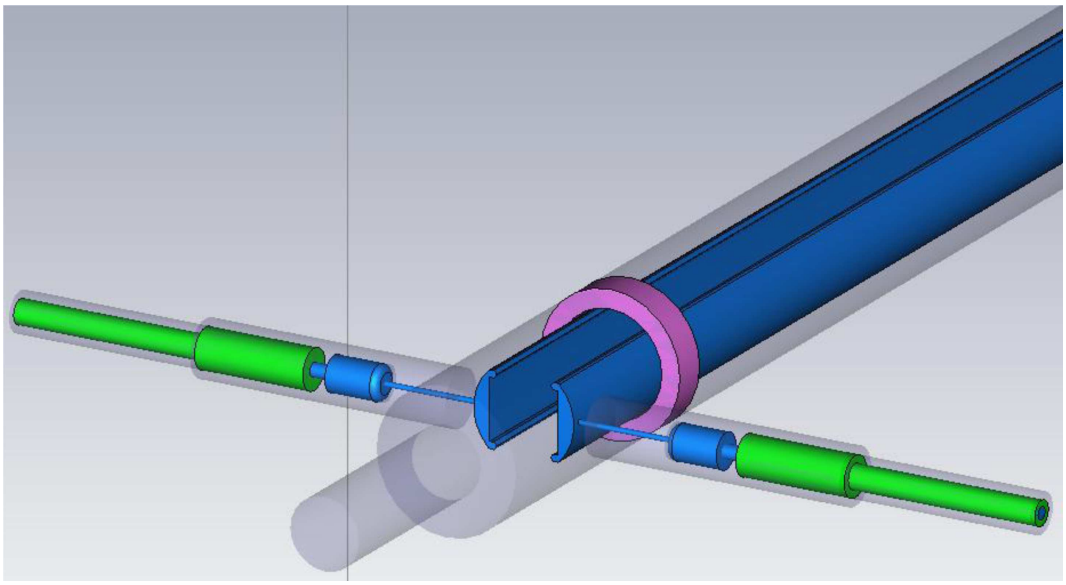

Figure 4.8: CST model used to study the effect of the commercial Kyocera feedthroughs over the S_{11} parameter and the beam coupling impedance.

(≈800.000 mesh cells for the half-model) due to the level of detail of the feedthrough. From ≈ 600 MHz, the Kyocera feedthroughs reflects all the power. However, these feedthroughs were the only commercial feedthroughs able to hold a voltage of 12.5 kV with 50 Ω characteristic impedance, although the impedance is only guaranteed for low frequencies. The effect of the Macor rings, increasing the magnitude of every third peak is not as clear as with the ideal coaxial feedthroughs in both operation modes, and from ≈ 800 MHz, the S_{11} parameter is the same in the two operation modes for the commercial feedthroughs. In the odd mode, the S_{11} parameter is lower for the commercial feedthroughs up to 300 MHz, probably due to a better connection between the electrode and the commercial feedthroughs, with more impact at low frequencies. In the even mode, however, the S_{11} parameter is always higher in the case of the commercial feedthroughs. In addition, a frequency shift is observed due to the change in the dielectric from only vacuum for both the ideal coaxial feedthrough and the transition to the electrode, to Al_2O_3 for the commercial coaxial feedthrough and back to vacuum for the transition: the different dielectric constant results in a change in the velocity of the pulse signal, and therefore a frequency shift.

Finally, the beam coupling impedance with the new model has been calculated using CST Particle Studio, and the results are shown in Fig. 4.10 and Fig. 4.11, for the longitudinal beam coupling impedance and the horizontal beam coupling impedance, respectively.

The longitudinal beam coupling impedance is the same for the two different feedthroughs considered up to ≈ 300 MHz, where the real part starts to be lower for the commercial feedthrough. However, the horizontal beam coupling impedance is not

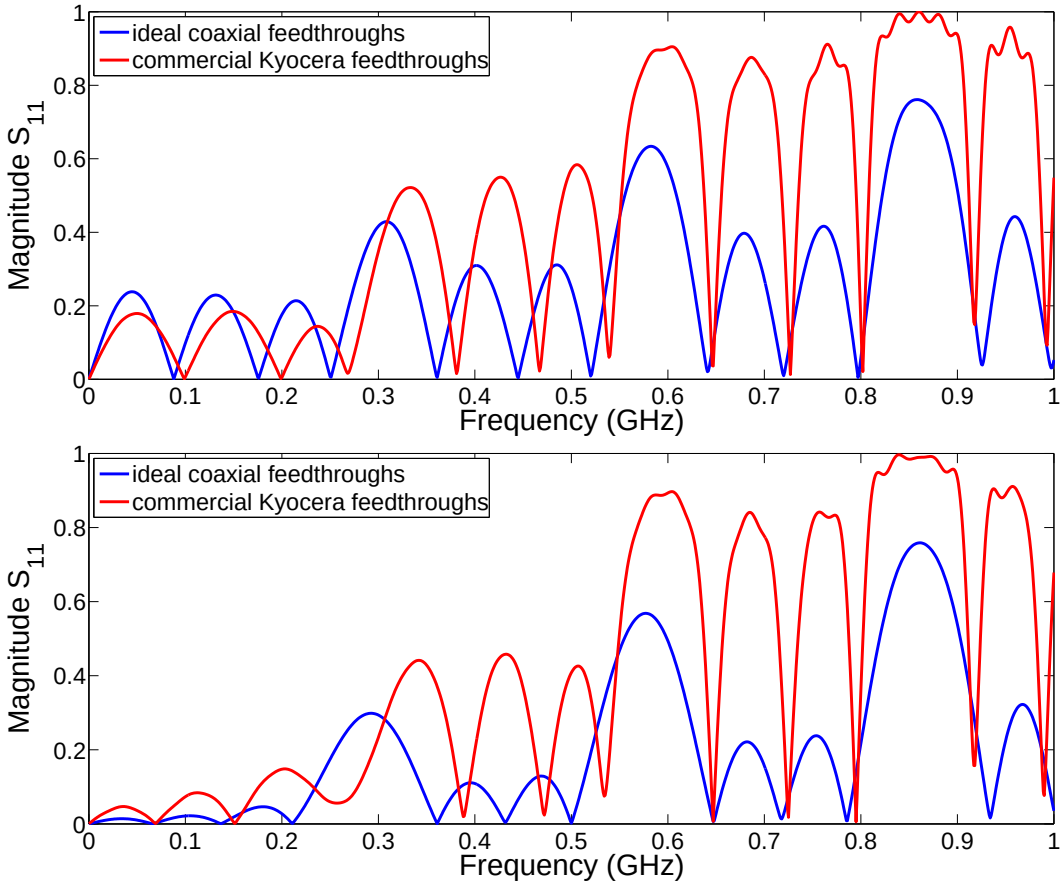

Figure 4.9: S_{11} for striplines with the ideal coaxial feedthroughs (blue line) and the commercial feedthroughs (red line), in the odd mode (top) and the even mode (bottom).

affected by the change of feedthroughs, and the same occurs with the vertical beam coupling impedance.

4.3 Manufacturing of the Striplines

The final design of the striplines first prototype for beam extraction from the CLIC DRs, shown in Fig. 4.12 is now completely defined. The electrode shapes, beam pipe diameter, electrode supports and feedthroughs characteristics have been obtained from analytical and numerical calculations and the drawings of the striplines were done under the guidelines of the design studies.

4.3.1 Material Choices

The electromagnetic calculations made during the design of the striplines and their components did not require to define the resistivity of materials in the simulations.

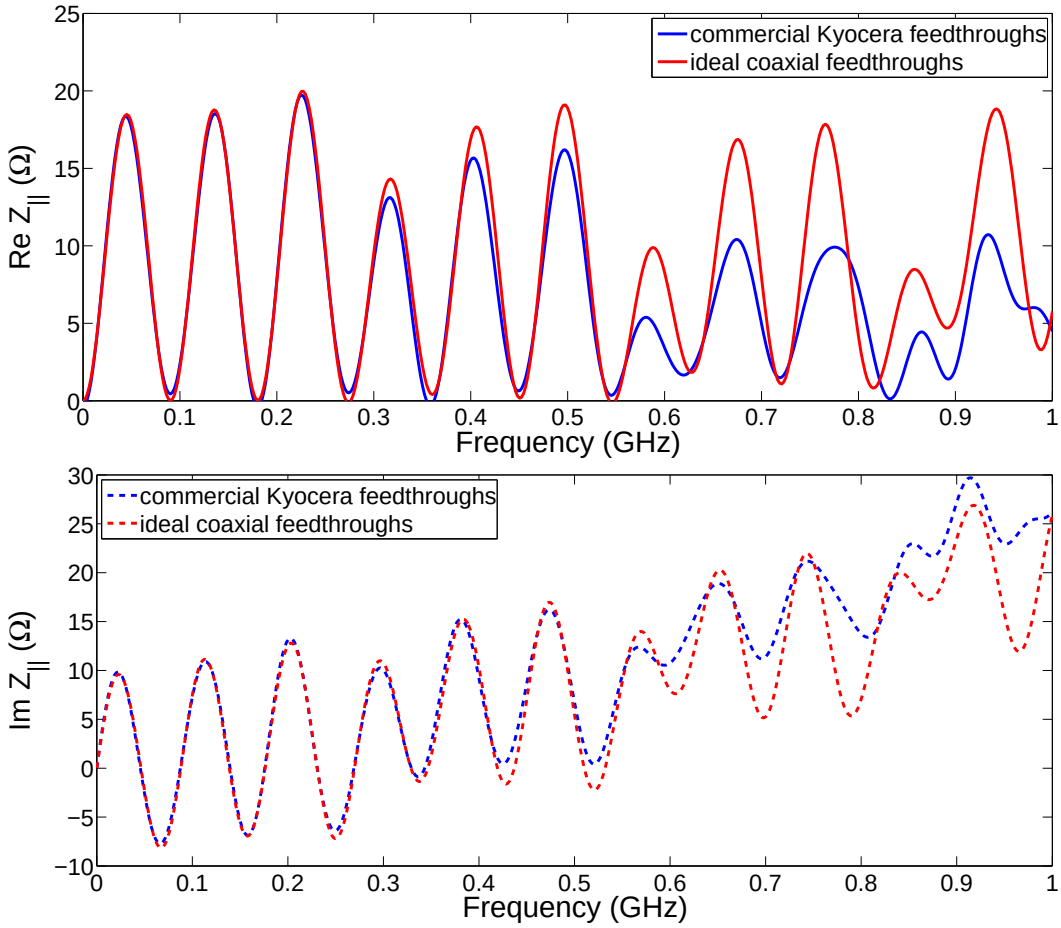

Figure 4.10: Real part (top) and imaginary part (bottom) of the longitudinal beam coupling impedance for striplines with the commercial feedthroughs (blue line) and the ideal feedthroughs (red line).

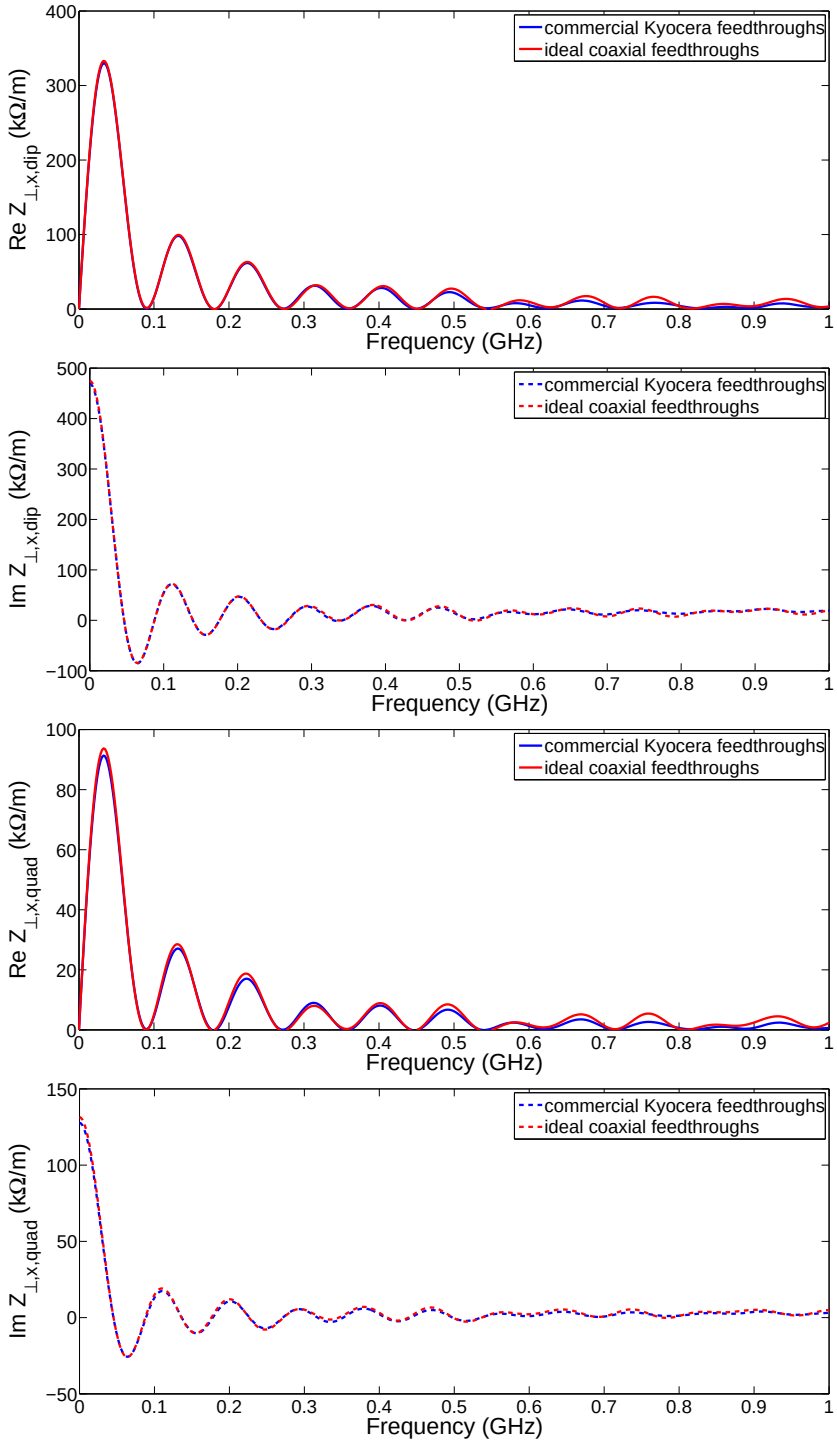

Figure 4.11: Real and imaginary part of the dipolar (top) and quadrupolar (bottom) components of the horizontal beam coupling impedance for striplines with the commercial feedthroughs (blue line) and with ideal coaxial feedthroughs (red line).

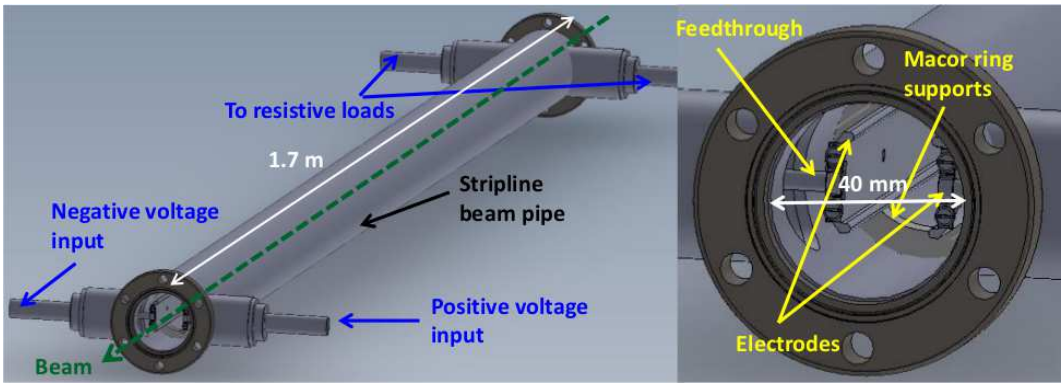

Figure 4.12: 3D view of the stripline kicker model showing the main components.

Stripline kickers operate as transmission lines; therefore, the resistive materials in the electromagnetic behaviour of the TEM transmission mode are a second order effect that can be neglected most of the times. However, the material selection is very important for the manufacturing of the stripline kicker because all the manufacturing procedures depend on it.

The beam pipe housing the stripline electrodes is a AISI-316L electropolished stainless steel tube of 1.7 m length. AISI-316L is a low carbon steel with an excellent corrosion resistance and high temperature strength. The electropolished stainless steel has a low roughness, which allows for (1) better operation for UHV applications, (2) lower current dissipation of the beam induced currents at high frequency, i.e., heating reduction, and (3) lower probability of RF breakdown. The internal diameter of the thin wall tube is 40.5 ± 0.2 mm.

Aluminium has been chosen for the electrodes: aluminium has a relatively large coefficient of thermal expansion (22×10^{-6} 1/K), however this material has been chosen because its machining is easy, and the priority was to achieve the tight tolerances required for field uniformity. The electrode supports will be manufactured using Macor, which is a machinable glass ceramic [74]. The feedthroughs are made up of a Fe-Ni-Co alloy, and use Al_2O_3 as a dielectric material [75]. All the chosen materials are compatible with ultra-high vacuum, of the order of 10^{-10} mbar.

4.3.2 Fabrication Tolerances

The effect of fabrication tolerances, upon field homogeneity over a 1 mm radius, has been studied using the 2D code Quickfield [66]. The considered geometric errors are the horizontal and vertical positions and the tilt angle of an electrode. All these parameters are mechanically defined by the tolerances of the electrode supports and the electrodes. The horizontal aperture of the Macor rings is 25.50 mm with a tolerance of +0/-0.10 mm, and the electrode thickness is 2.75 mm and has a tolerance of +0.05/-0.05 mm. In addition, the thickness of the ring, which is 14.40 mm, has a tolerance of

+0/+0.05 mm. Hence, a maximum error in the horizontal position of the electrodes of +0.20 mm is expected. The vertical position is defined by the diameter of the Macor ring in the vertical dimension, 40.30 mm with a tolerance of +0/-0.10 mm, as well as the thickness of the ring. This leads to a maximum error expected in the vertical position of the electrodes of 0.15 mm. Finally, a non-parallelism of the electrodes will occur if the two flat parts of the Macor ring are not parallel with each other. Each flat part of the ring could be tilted by 0.05 mm, which can result in a non-parallelism of one electrode with respect to the other one. In addition, the flat part of the electrode could also have a non-parallelism of 0.05 mm. Then, a maximum non-parallelism of 0.1 mm in the horizontal plane is expected. Since the electrode height is H = 20.6 mm, we have that the maximum tilt angle expected in one electrode is $tan\,\theta = 0.1/H$ which corresponds to 0.06°. If the assembly of electrodes is rotated inside the beam stripline radius, it will not afect the field inhomogeneity, but it will change the orientation of the electromagnetic field, producing an error in the deflection direction. These tolerances were accepted after talking with the manufacturer, taking into account the machining of the striplines components and the materials, which made possible to manufacture the striplines for a reasonable price.

Table 4.1 summarizes the field inhomogeneity results for three different types of manufacturing tolerances studied.

	Maximum error	**Field inhomogeneity**
None	0	± 0.008 %
Horizontal (H)	+0.2 mm	±0.012 %
Vertical (V)	-0.15 mm	±0.007 %
Tilt (T)	0.06°	±0.008 %
Combination (H+V+T)		±0.015 %

Table 4.1: Field inhomogeneity, over a 1 mm radius, for the maximum geometrical errors expected during manufacturing.

The maximum field inhomogeneity specified, for the CLIC extraction DR kicker, over a 1 mm radius, is ± 0.01%. As shown in Table 4.1, a manufacturing error in the horizontal position of an electrode may increase the field inhomogeneity beyond specification, whereas an error in the vertical position of an electrode or a tilt angle of 0.06° will not. The tolerance of the striplines beam pipe radius has not been taken into account since its effect over the field homogeneity is not very important: the effect of the beam pipe radius tolerance is one order of magnitude lower than the effect of the electrode tolerances. A combination of these three errors, however, would increase the field inhomogeneity to ± 0.015%, although it represents the worst case. In addition to these mechanical tolerances, another manufacturing tolerance that should be taken into account is the roughness of the beam pipe, which must be below 1.6 μm.

Nevertheless, the field inhomogeneity requirement was studied and relaxed: the kicker good field region could be reduced from 1 mm radius to 0.5 mm radius [76].

Assuming a linear variation of the field at the centre of the aperture, it would represent a field inhomogeneity of ±0.007 in the worst case, which is below the maximum value allowed.

4.3.3 Assembly of the Striplines and Components

The striplines and components assembly has been done in two stages. The electrode supports were configured to be able to assemble the electrodes outside the beam pipe, as shown in Fig. 4.13, which makes easier the process of component changes or replacement. The electrodes for the extraction stripline kicker from CLIC DRs have been made up of aluminium AL6083, machined in a numerical control machine (CNC).

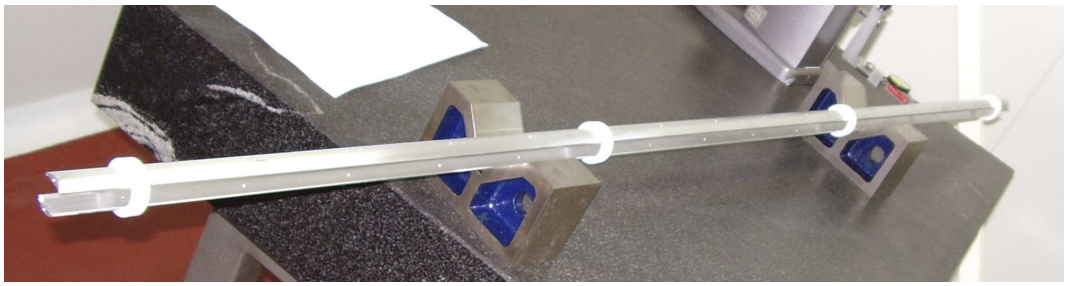

Figure 4.13: Picture of the electrodes assembled with the Macor rings, outside the beam pipe.

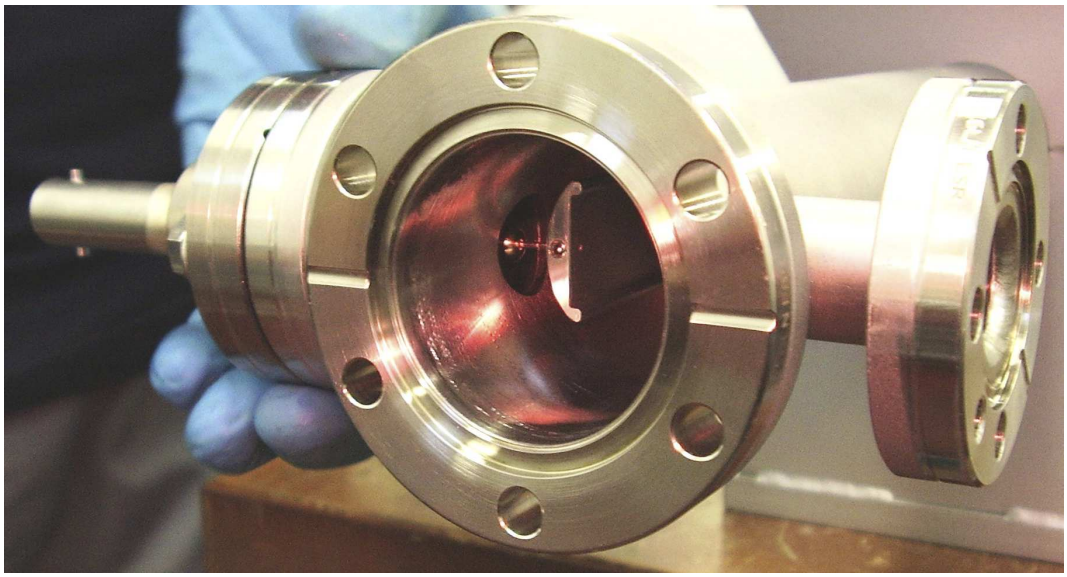

Figure 4.14: Picture of the electrodes, electrode connections and beam pipe flanges

Once the electrodes position, separation and parallelism was verified, the assembly was introduced into the beam pipe, using special tools in order to ensure the orientation and position of the electrodes inside the beam pipe with respect the fiducials: its angular position is guaranteed by a pin embedded in the striplines beam pipe wall from one of the ends of the electrodes. The other end of the electrodes is not fixed by a pin, which allows for a maximum elongation of 2 mm of the electrodes with respect the striplines beam pipe. This is important because, during the kicker operation, and assuming that the striplines beam pipe are at room temperature, the maximum temperature that the electrodes can hold due to this maximum allowed elongation is 72°C -the electrodes heating is produced by the induced currents from both the beam and the inductive adder pulses. This is compatible with the calculations made in Section 3.5.2. Furthermore, when baking out the striplines, the striplines beam pipe increase its temperature before the electrodes: in this case, the difference in the lengths achieved for the two materials would be given by the sum of the differential expansion coefficients and the differential temperature between them. For a difference of 1 mm in the lengths of the striplines beam pipe and the electrodes due to the differential temperature, and another 1 mm due to the differential expansion coefficient, the temperature gradient should be kept below 26°C. Therefore, a smooth baking out of 125°C with a slow heating rate is proposed, which will help to evaporate the water in the striplines beam pipe walls and will speed up the pumping time, in order to achieve a low enough pressure for the DR performance.

The commercial beam pipe used for this prototype has been a tube of stainless steel AISI316L, with an inner diameter of 40.5 mm radius. Flanges are required to connect the stripline beam pipe to the main beam pipe of an accelerator, and to connect the feedthroughs with the striplines beam pipe, in order to be able to change them easily if feedthroughs with a better impedance matching at high frequencies are found. The flanges used in this case, shown in Fig. 4.14 , are ConFlat (CF) flanges, which prevents leaks when working with ultra high vacuum devices. CF flanges must be welded to the striplines beam pipe, so they are made also of stainless steel. The welding method used has been the Tungsten Inert Gas (TIG) welding, which allows for stronger and high quality welds, since the weld area is protected from atmospheric contamination by an inert shielding gas. The feeedthroughs were connected to the electrodes by using screws, in order to facilitate the disassembly, as it is shown in Fig. 4.14. Then, the final assembly was tested in order to ensure the conformance with specifications. These tests, carried out by the manufacturer company, included the dimensional control and vacuum tests.

Chapter 5

Laboratory Characterization Tests of the Striplines First Prototype

5.1 Introduction

Measurements in the laboratory, without beam, have been made to characterize the electromagnetic response of the striplines, comparing the results of the measurements with the electromagnetic simulations developed in Chapter 3 and Chapter 4. The measurements carried out have been the following: (1) power reflection and transmission through the striplines, (2) longitudinal and transverse beam coupling impedance, and (3) RF breakdown tests. Laboratory measurements of the field homogeneity at the center of the striplines aperture has not been carried out, because a suitable technique to measure the specified field inhomogeneity in a radius of 1 mm has not been found. For this reason, the new electrode supports made up of ceramic rings are specially good: with them the field uniformity is ensured before inserting the electrodes assembly into the striplines beam pipe.

The reflection and transmission parameters depend on the characteristic impedance matching of the striplines with the power supply and the terminating loads, and must be characterized for two reasons: in the odd mode, the magnitude of the reflection parameter must be known at low frequencies (up to a few MHz) in order to be sure that the kick pulse will not be distorted when passing through the striplines. In the even mode, the magnitude of the reflection (or transmission) parameter must be taken into account since the beam coupling impedance depends directly on it. The longitudinal and transverse beam coupling impedance are limited by beam requirements in the DRs of CLIC [19], and their characterization is very important. The beam coupling impedance has been measured up to 1 GHz at the laboratory. Due to the small bunch length of $\approx$ 2 mm (Table 1.5) in the CLIC DRs, the high-frequency contribution of the beam coupling impedance goes up to hundreds of GHz: this is difficult to measure in laboratory, and only can be measured with beam in a test facility. The reflection and transmission parameters, as well as the beam coupling impedance measurements,

were done in the semi-clean room of the TE-ABT (Technology - Accelerator Beam Transfer) laboratory at CERN. Finally, breakdown tests have been carried out in a High Voltage (HV) test cage in the TE-ABT laboratory at CERN, in order to have an estimation of the Breakdown Rate (BDR) per hour expected at the high operating voltage of 12.5 kV. In this chapter, a description of these laboratory tests, including the methodology used, the test bench, and the results is reported.

5.2 Reflection Parameter Measurement

5.2.1 Methodology

The reflection parameter (S_{11}) is directly related with the impedance mismatch along the striplines and their components. The following sources of impedance mismatch, for the striplines, have been previously identified:

- during kicker operation (odd mode), the characteristic impedance of the electrodes is lower than 50 Ω;
- simulations have shown that the presence of electrode supports increases the reflections;
- the feedthroughs are coaxial outside of the beam pipe but the connection from each feedthrough to the electrode is not coaxial: hence the characteristic impedance of the connection between the electrode and feedthrough is not constant.

The impedance mismatch produced by the characteristic impedance of the striplines and by the Macor rings, has been well identified by CST simulations. However, due to the complexity of modelling the feedthroughs, the reflection parameter measurement will help to better understand the impedance mismatch introduced by the connection between the electrode and the feedthrough. In addition, for terminating the electrodes, Diconex resistors [77] should be used for the 50 Ω termination, which were the ones used in the initial HV tests on the prototype inductive adder [78], for powering the striplines. However, the Diconex terminating resistors are not ideal, their value is frequency dependent. In the CST simulations, by contrast, the electrodes were terminated with a constant characteristic impedance of 50 Ω. For that reason, in order to compare directly the results from the measurements with the simulations, the first test was done by terminating the electrodes with "high quality" (HQ) resistors from the calibration kit of the Network Analyzer (NA), with a "constant" 50 Ω characteristic impedance for all the frequencies. The S_{11} parameter was measured directly with the NA.

5.2.2 Test Setup

The test setup for measuring the S_{11} parameter is schematically shown in Fig. 5.1. The reflection parameter measurement has been carried out by using an Agilent

E5071C 2-port NA, which inputs an RF signal through the input port and reads the signal arriving at the output port. In order to characterize the two operation modes of the striplines, an hybrid splitter has been used, which splits the signal for operating in the even mode, and splits and de-phases 180° the RF signal for the odd mode.

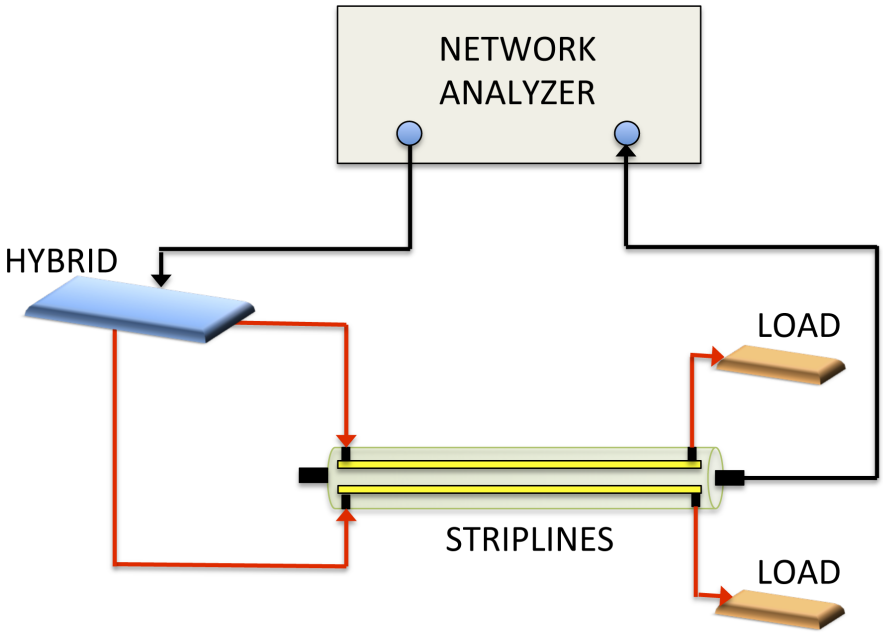

Figure 5.1: Block diagram of the test bench for S_{11} parameter measurements in both operation modes.

The calibration of the NA has been carried out with HQ 50 Ω resistors on the output of the hybrid. However, for carrying out the measurements, the outputs of the hybrid are connected to the stripline inputs with ≈ 1.4 m of HTC-50-7-2 coaxial cable, as shown in Fig. 5.2. Similarly the output of each stripline is connected to a terminating resistor via ≈ 1.4 m of HTC-50-7-2 coaxial cable. The presence of the HTC-50-7-2 coaxial cables, which are not present in the NA calibration, may influence the measurement results. Since each Diconex resistor has a Teledyne 521 series female connector, an HTC-50-7-2 HV coaxial cable, fitted with two Teledyne RG213-521 plugs, is used to interconnect a stripline electrode and a termination resistor. Each electrode is connected to one port of the hybrid, by using a cable with a N-type connector on one end and RG213-521 plug on the other end, the third port of the hybrid is connected to the NA and the fourth port is matched to 50 Ω. The NA was calibrated at the output of the hybrid.

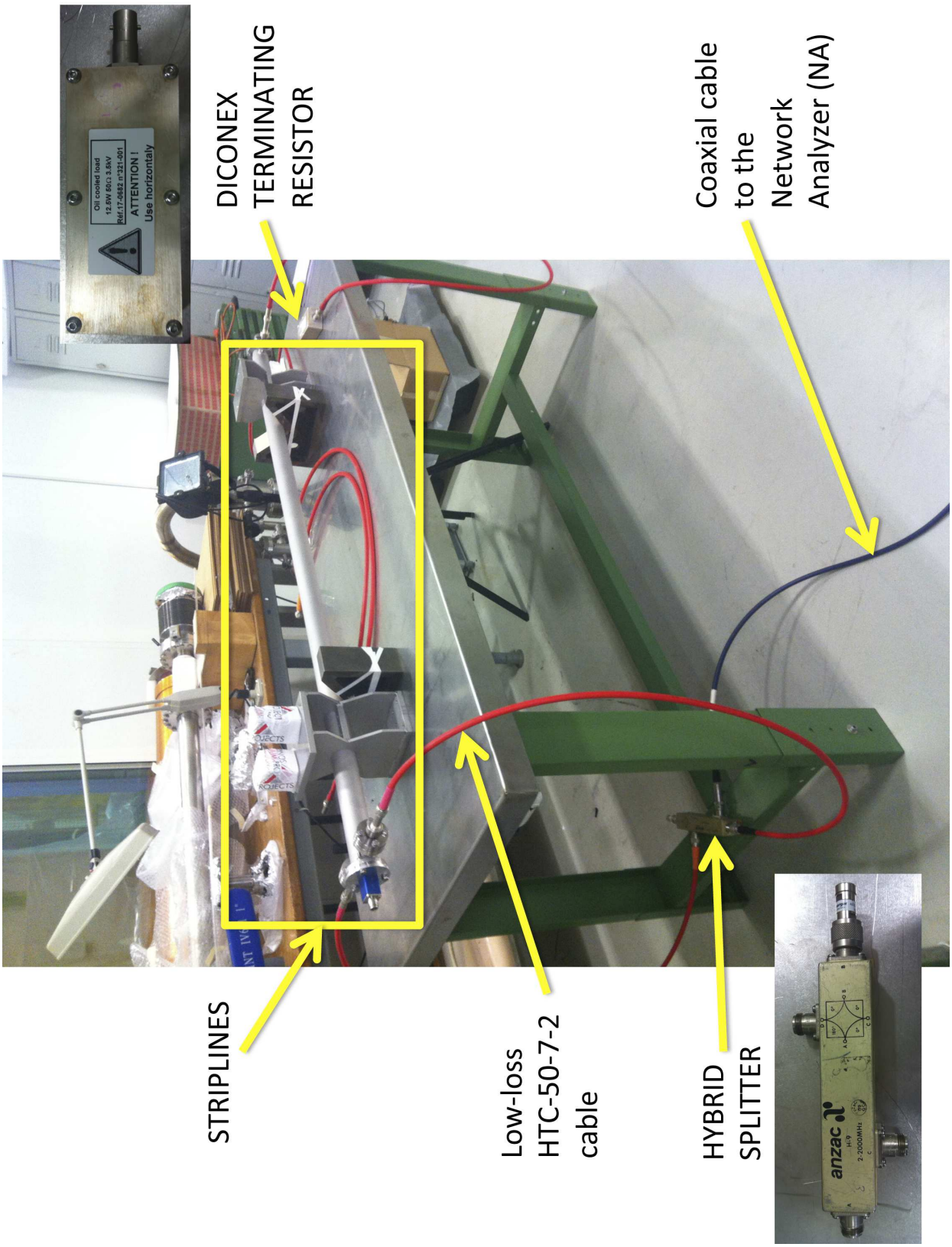

Figure 5.2: Test bench for S_{11} parameter measurements in both operation modes.

5.2.3 Results

When simulating the S_{11} parameter with CST, the terminating ports have a constant characteristic impedance of 50 Ω. Therefore, in order to compare directly measurements with CST simulations of the reflection parameter S_{11}, the first measurement was done by terminating the electrodes with the HQ resistors on the end of HTC-50-7-2 cable. Results comparing both simulations and measurements, which started at a frequency of 2 MHz, are shown in Fig. 5.3 and Fig. 5.4 for the odd and even mode, respectively.

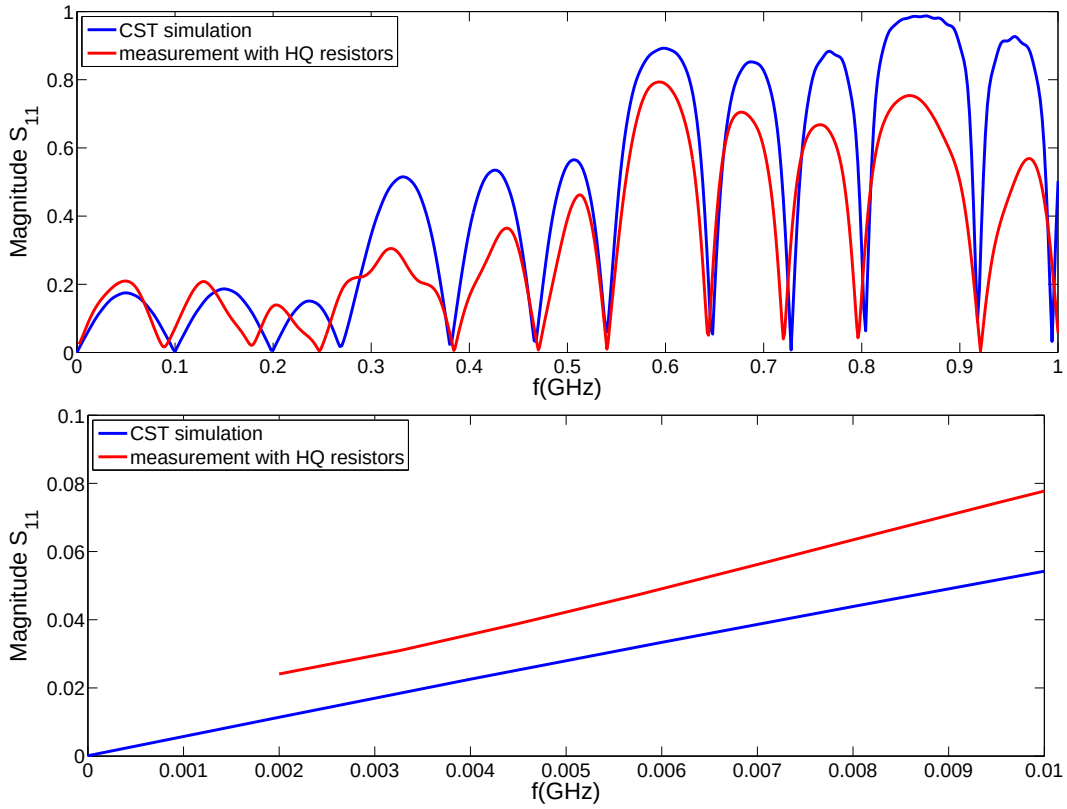

Figure 5.3: S_{11} parameter measured when driving the electrodes in the odd mode configuration, and the output is terminated with the HQ terminating resistors (red line), compared with CST simulations (blue line), for a frequency range up to 1 GHz (top) and up to 0.01 GHz (bottom). Measurements with the NA have started at a frequency of 2 MHz.

The reflections during odd mode operation of the striplines (kicker ON), shown in Fig. 5.3 (top), may increase the driving pulse ripple. However, significant content of the driving pulse from the inductive adder will extend up to ≈ 0.01 GHz, for a pulse rise time of 50 ns. The reflections in the odd mode for a frequencies up to 0.01 GHz is below 0.1 (Fig. 5.3, bottom) and, therefore, they are not expected to significantly influence the ripple of the pulsed field. It is worth mentioning that the

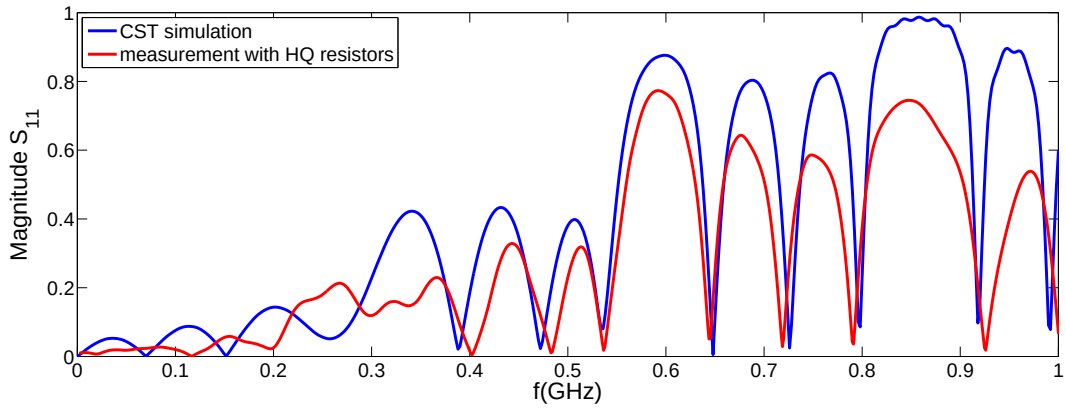

Figure 5.4: S_{11} parameter measured when driving the electrodes in the even mode configuration and the output is terminated with the HQ terminating resistors (red line), compared with CST simulations (blue line).

laboratory results for the frequency of the maxima and minima agrees quite well with the simulation results at high frequencies, whereas at low frequencies there is some disagreement, especially in the even mode.

For the even mode (kicker OFF), the simulated reflections shown in Fig. 5.4 above ≈ 0.3 GHz, are generally stronger than those measured. Reflections in the even mode configuration are lower than in the odd mode configuration, with greater difference at low frequencies: this is due to the fact that the striplines even mode characteristic impedance is better matched to 50 Ω than in the case for the odd mode characteristic impedance: in the odd mode the characteristic impedance of the striplines is ≈ 41 Ω, as shown in Chapter 3.

To evaluate the potential of the Diconex resistors for terminating the electrodes with 50 Ω when the striplines will be installed in an accelerator test facility, their characteristic impedance has been measured with the NA. The two Diconex resistors used, with references REF 17-0682 and REF 17-0683 have been compared to be sure that both resistors have the same frequency response. Figure 5.5 shows the measured impedance, real part (top) and imaginary part (bottom), of two Diconex terminating resistors as a function of frequency. Up to ≈ 0.1 GHz the impedance variation is ±5% of its nominal value (50 Ω). Again, the frequency content of the driving pulse extends to only ≈ 0.01 GHz, and it corresponds to a resistor impedance variation of ±0.2%. Therefore, the impedance of the Diconex resistor is expected to be acceptable for the inductive adder. However, the high resonance peaks that appears in Fig. 5.5 from about 0.2 GHz, will affect the reflection parameter in the even mode, and therefore, the beam coupling impedance. Fig. 5.6 shows a measurement of the S_{11} parameter when the remote end of each electrode is connected to a Diconex terminating resistor using the two cables with RG213-521 plugs on both ends, and the electrodes are driven in the even mode. For comparison the measurement of the S_{11} parameter when the remote end of the electrodes is connected to the HQ resistors (Fig. 5.4, red line) is also shown.

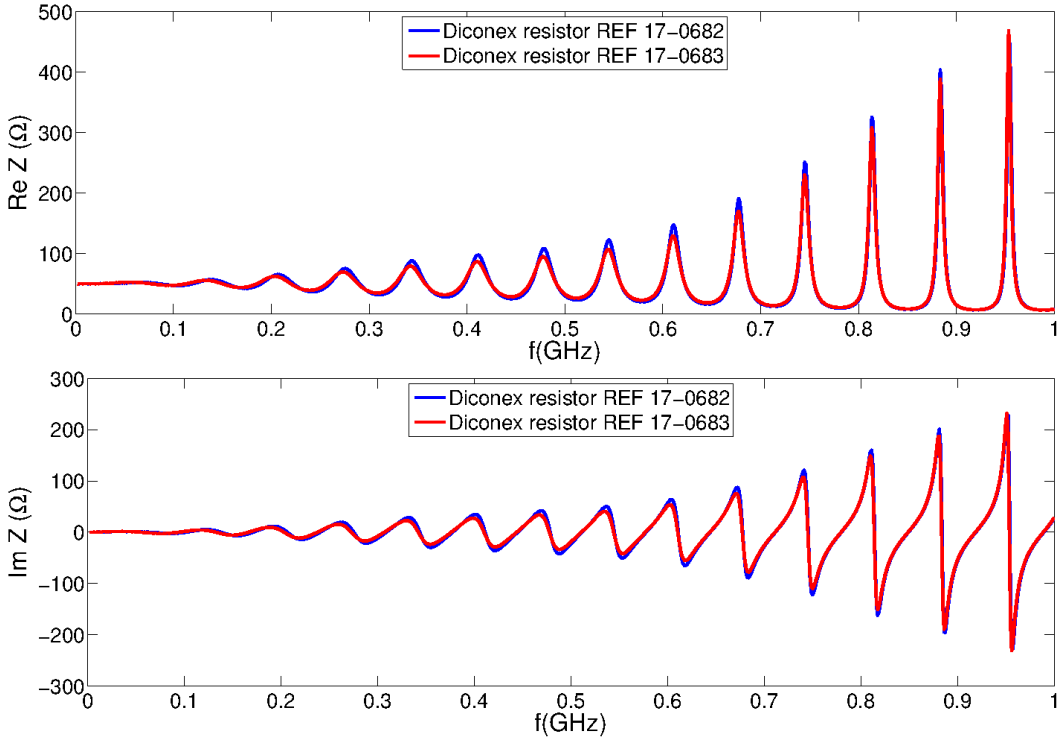

Figure 5.5: Real impedance (top) and imaginary impedance (bottom) calculated from the S_{11} parameters measured with the NA, for the two different Diconex terminating resistors.

The results show that there are more resonances, when the striplines are terminated with the Diconex resistors, at frequencies above $\approx$ 0.2 GHz, and they are therefore expected to influence the beam coupling impedance.

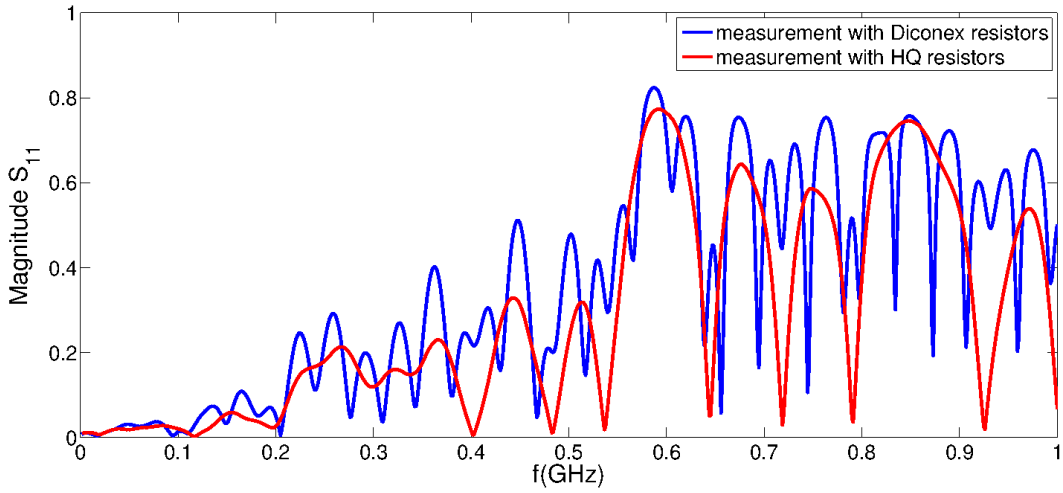

Figure 5.6: S_{11} parameter measured when driving the electrodes in the even mode configuration, and terminating both electrodes (i) with the Diconex resistors (blue line) and (ii) HQ resistors (red line).

5.3 Beam coupling impedance measurements

Beam coupling impedance is a critical issue in many high intensity particle accelerators. The problems are twofold: longitudinal and transverse impedance may drive instabilities and cause undesired tune shifts, while the real part of the longitudinal impedance also gives rise to power dissipation in the striplines. For high intensities this may cause significant heating.

Beam coupling impedance can be measured in the laboratory by using one (or two) wire(s) that represents the beam. The same Agilent NA has been used in order to measure the transmission parameter (S_{21}), and from this measurement, the longitudinal and transverse beam coupling impedance can be calculated. Wire measurements rely on the fact that the electromagnetic field distribution of an ultrarelativistic beam is very similar to that of a Transverse Electromagnetic (TEM) line. This TEM line is formed by the wire (or wires) with the ground plane of the electrode, with a characteristic impedance Z_{line} which is a function of the wire diameter and its distance away from the ground plane. The wire diameter should be as small as possible to get a high line impedance, which best reflects the fact that the beam acts as an ideal current source. For our measurements, a wire of 0.5 mm diameter has been used. The wire is made up of Cu/Ag_{20}, not enamelled, with a $\approx$ 2.1 μm thick coating of silver. This soft copper is

used with elements which are longer than approximately 1 m, where the effect of sag may play a significant role [79].

5.3.1 Longitudinal beam coupling impedance

For longitudinal beam coupling impedance measurements, a single wire is inserted into the stripline kicker and the signal transmission S_{21} is measured, from which the longitudinal impedance can be calculated. The most common techniques available for measuring the longitudinal beam coupling impedance are: (1) the single wire transmission, where a resisor is used to match the impedance of the device under test (DUT) to the system impedance, or (2) the resonant coaxial wire method, which may be a better approach for small losses, since very high sensitivity can be obtained. The single wire transmission method has been used in this case to measure the longitudinal beam coupling impedance of the striplines. The resonant method has not been used due to the limited frequency resolution that can be expected from the relatively short length of the striplines and beam pipe. The single wire transmission method will be explained in the following.

Methodology

The single wire method consists of inserting a wire between the striplines. A RF pulse from the NA goes through the wire, creating image currents on the electrodes. The transmission of these image currents through the electrodes is measured with the NA. The transmission parameter of this current will depend on the characteristic impedance of the TEM line formed by the striplines and the wire. To calculate this line impedance, an analytical equation for a TEM line formed by a wire between two parallel plates can be found in [79]:

$$Z_{line}(\Omega) = 60\, ln\left(1.27\,\frac{D}{d}\right) = 235.7\Omega \tag{5.1}$$

where D is the distance between the electrodes, i.e. the aperture, which is 20 mm, and d is the wire diameter, equal to 0.5 mm in this case.

In order to match the characteristic impedance of the TEM line to the NA circuit, a single series resistor can be added at both ends of the wire. In our case two low-inductance carbon resistors of $R_s = Z_{line} - Z_0 \approx 185\,\Omega$, has been connected at each end of the wires. Once the characteristic impedance of the TEM line is matched, the S_{21} parameter is measured with the NA, and from this result the following formula is used to calculate the longitudinal characteristic impedance [79]:

$$Z_{\|} = -2Z_{line} lnS_{21} \tag{5.2}$$

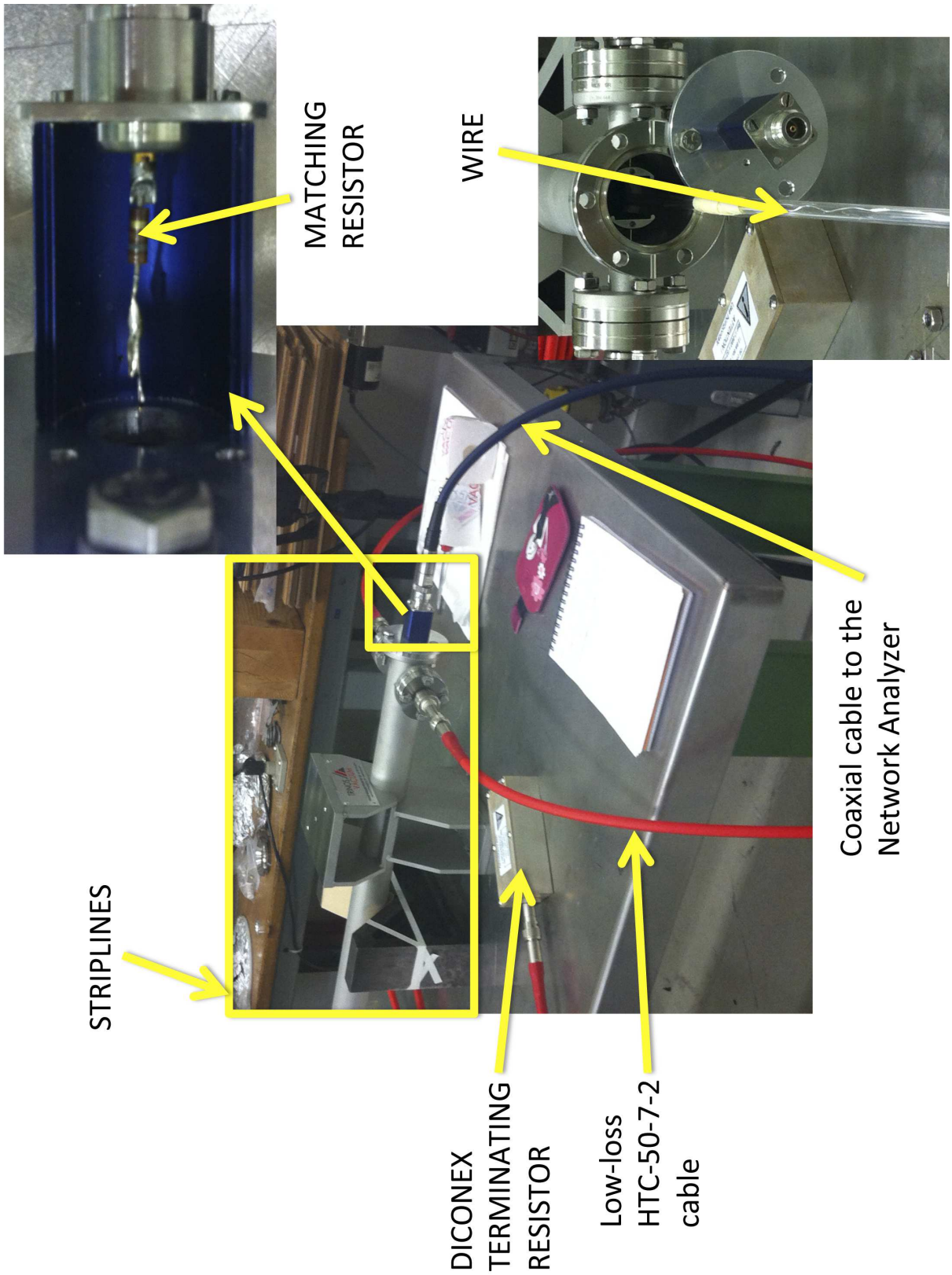

Figure 5.7: Single wire transmission test bench for longitudinal beam coupling impedance.

Test Setup

The setup for a single wire measurement is shown in Fig. 5.7. The two ends of the wire are soldered to the matching resistors and then connected to the NA. The input ports (upstream feedthroughs) are connected either to the HQ resistors or the Diconex terminating resistors by using the two HTC-50-7-2 coaxial cables with RG213-521 plugs on both ends, whereas the output ports (downstream feedthroughs) are matched to 50 Ω connecting them to the hybrid with the same coaxial cables.

The diagram of the test setup (Fig. 5.8) shows the different characteristic impedances of the system composed by the NA, the striplines, the wire, the matching resistors and the loads.

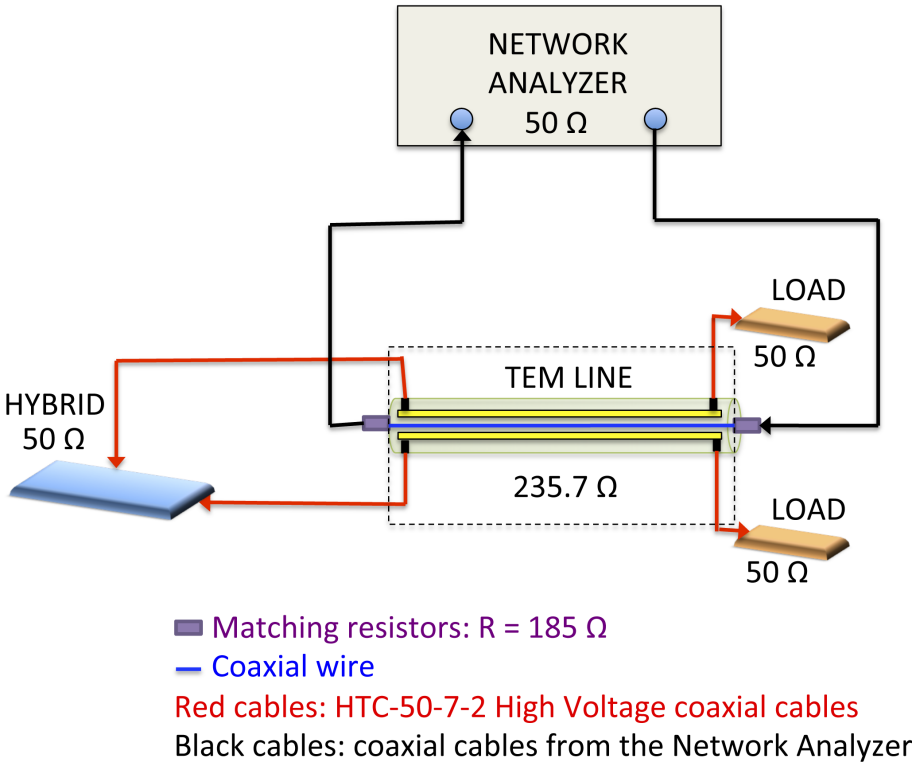

Figure 5.8: Block diagram of the test bench for longitudinal beam coupling impedance measurement with the single wire transmission method.

Results

From the measured S_{21} parameter, the longitudinal beam coupling impedance $Z_{\parallel}$ is calculated, when the remote end of the striplines is matched to 50 Ω by using the hybrid. Results for both measurements and CST simulations are shown in Fig. 5.9. There is a good agreement between the calculated and simulated longitudinal beam coupling impedance up to $\approx$ 0.25 GHz: at higher frequencies the simulations and

measurements are not in good agreement, probably because of the non-ideal properties of the matching resistors, cables and feedthroughs.

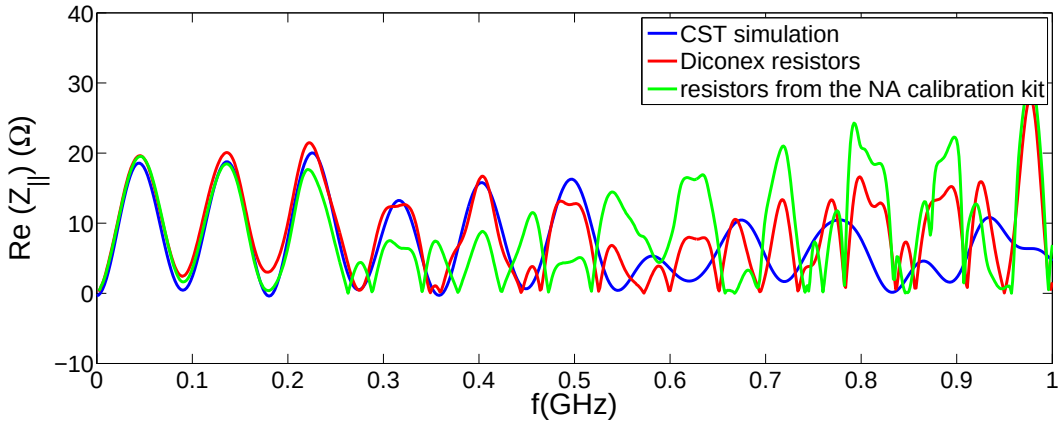

Figure 5.9: Calculated real component of $Z_{\parallel}$ from the S_{21} parameter measured when terminating the electrodes with the Diconex resistors (red line) or with the HQ resistors from the calibration kit of the NA (green line), compared with CST simulation (blue line).

The single wire measurement technique gives good frequency resolution, however any residual mismatch in the characteristic impedance between the measurement network and the device under test (DUT) results in reflections in the system. These reflections can be removed by an appropriate time domain gated measurement but there can be a large DC offset, caused by the loss of transmitted energy by the gating of the signal. The resistively matched measurements generally gives good results below a few hundred MHz but the residual mismatch in the system can cause large oscillations which mask the true impedance [80].

5.3.2 Transverse Beam Coupling Impedance Measurement

For transverse beam coupling impedance measurements, two techniques are commonly used: (1) the two wires method, or (2) the moving single wire method. The two wire method consists of inserting two wires in the stripline aperture, and driving the wires with opposite phase RF waves. With this method, the dipolar component of the transverse impedance is calculated. By contrast, in the moving single wire method only one wire is used, and the transverse beam coupling impedance is calculated from the longitudinal beam coupling impedance at different offsets of the wire from the centre of the striplines. With this method, the total transverse impedance (dipolar and quadrupolar components) is measured. The results of the two wire measurements will be compared with the simulation results for the dipolar beam coupling impedance.

Methodology.

The dipolar component of the transverse impedance of the striplines has been measured by producing a dipolar field with two wires, of 0.5 mm diameter each, driven with opposite phases by using two hybrids. To have a measurable effect, the wire spacing should be significantly smaller than the aperture, due to the fact that the dipolar field created only interacts with the fringe fields and, therefore, the effects are small: a wire spacing of about a third of the aperture appears to be a good compromise [79]. In our case, for an aperture of 20 mm a wire spacing of 7 mm has been chosen. In order to match the two wire line impedance to the impedance of the NA, the hybrids and the loads, a matching resistor at the ends of each wire has been used. To calculate the resistance value of each matching resistor, the following equation has been used:

$$R_s = Z_{line}/2 - Z_0 \tag{5.3}$$

where Z_{line} is the differential-mode line impedance and $Z_0 = 50\,\Omega$. The differential-mode line impedance for two wires with opposite polarity is given by:

$$Z_{line} = \frac{120}{\sqrt{\epsilon_r}}\text{acosh}\frac{\Delta}{d} \tag{5.4}$$

where ϵ_r is the relative permittivity of the medium between the wires ($\epsilon_r = 1$ for air and vacuum), d is the wire diameter and Δ is the wire spacing. In our case, using Eq. (5.3), the calculated value of Z_{line} is 399.7 Ω: low-inductance (carbon film) single series resistors of 160 Ω have been used for matching network. The transmission parameter S_{21} has been measured with the NA, and from this measurement the longitudinal impedance $Z_\parallel$ can be estimated by using the formula [79]:

$$Z_\parallel = -2Z_{line}\, ln(S_{21}) \tag{5.5}$$

Then the dipolar component of the transverse impedance has been found from the following equation:

$$Z_{\perp,dip} = \frac{cZ_\parallel}{2\pi f \Delta^2} \tag{5.6}$$

where c is the speed of light, and f is the frequency at which the S_{21} parameter is measured.

Test Setup.

The setup for measuring the dipolar transverse beam coupling impedance is shown in Fig. 5.10. The two edges of each wire are soldered to the matching resistors and then connected to the NA via two hybrids. The input ports (upstream feedthroughs) are connected either to the ideal resistors or the Diconex terminating resistors, whereas the output ports (downstream feedthroughs) are matched to 50 Ω.

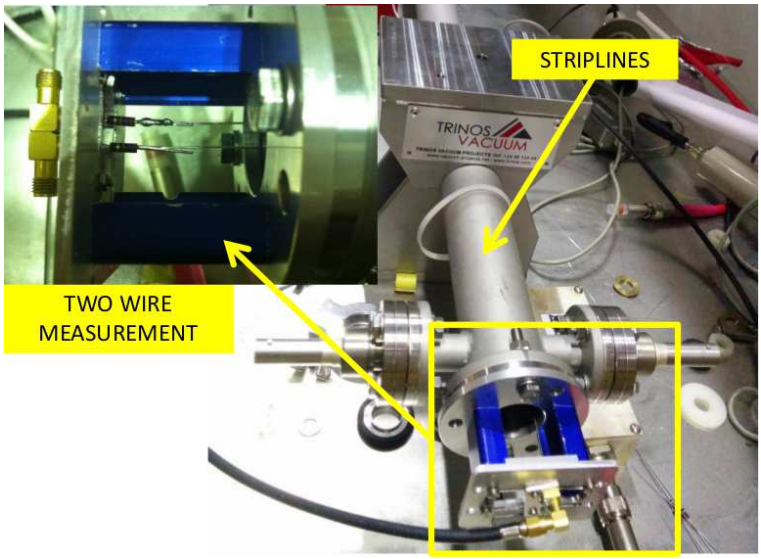

Figure 5.10: Two wire test bench for dipolar transverse beam coupling impedance.

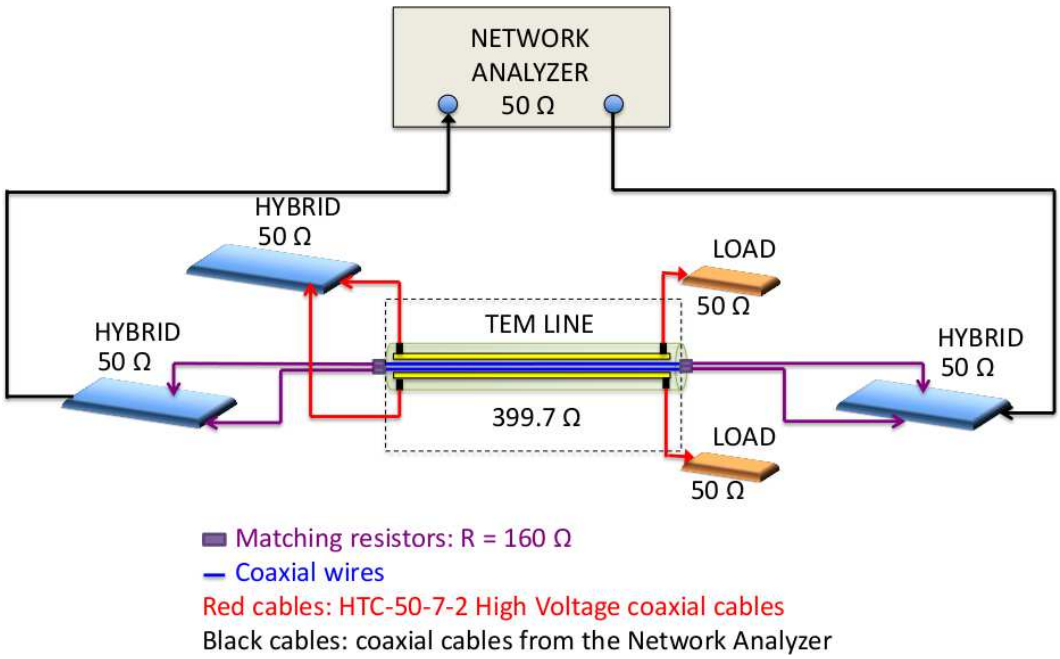

Figure 5.11: Block diagram of the test bench for the dipolar transverse beam coupling impedance measurement with the two wire method.

The diagram of the test setup (Fig. 5.11) shows the different characteristic impedances of the system composed by the NA, the striplines, the two wires, the matching resistors and the loads.

Results.

Results for the dipolar transverse impedance are shown in Fig. 5.12, for the horizontal and the vertical plane, when terminating the electrodes with the ideal 50 Ω resistors from the NA calibration kit, and with the Diconex terminating loads, with a frequency-dependent value [81].

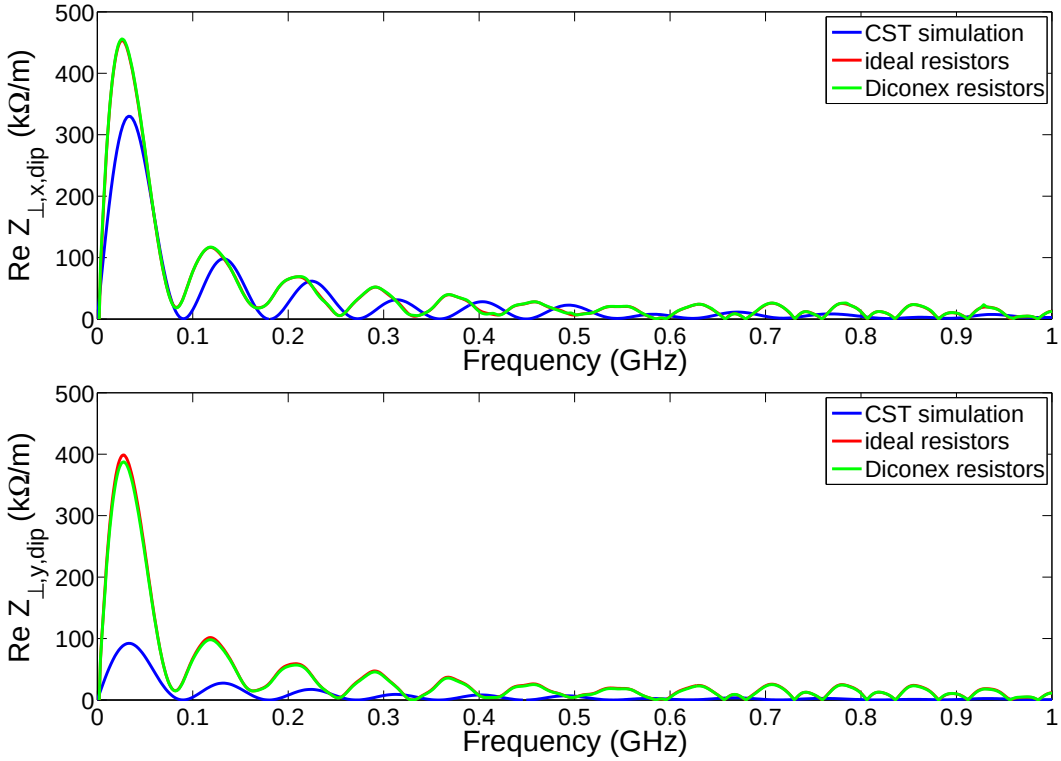

Figure 5.12: Dipolar horizontal (top) and vertical (bottom) impedance, when terminating the electrodes with the Diconex resistors (green line) or with the "ideal" resistors (red line), compared with the CST simulation (blue line).

For the real part of the horizontal dipolar impedance, a rough agreement has been found between the measurements and the CST simulation: the difference is thought to be due to the presence of the wire detuning the resonances, whereas the simulations are done without a wire. For the simulations also a perfect matching at the feedthroughs is assumed, and in reality the cables used to connect the feedthroughs to the terminating resistors may affect the measurement. In the case of the vertical dipolar impedance, the peak values are much higher for the measurements than for the simulations: the reasons for the discrepancies are under investigation. The results for the dipolar beam

coupling impedance measurements in the two planes are quite similar, and do not show significant differences when terminating the electrodes either with the "ideal" resistors or the Diconex terminations: the termination at the end of the cable seems not to matter. Further studies of the transverse beam coupling impedance will be done, in both planes, to better understand the results obtained. In addition, tests with a single wire will be done in order to measure the total transverse beam coupling impedance.

5.4 High Voltage Tests: DC Breakdown

5.4.1 Methodology

For beam extraction from the CLIC DRs, each stripline will be driven by a pulse of 12.5 kV voltage; for that reason, HV tests on the first prototype are necessary to verify if there are discharges, e.g. on vacuum feedthroughs or between the electrodes and the vacuum chamber, especially where the four Macor rings are placed [69]. First HV tests have been performed using two DC HV power supplies, which are low current with a relatively small output capacitance. The striplines were first pumped down to a final pressure of 4×10^{-8} mbar. For a beam pipe of 20.25 mm radius and a length of 1.7 m, generally it is difficult to achieve this value of vacuum; however, in this case, the electropolished stainless-steel of the tube, with low roughness, helped to arrive to this value in a relatively short period of time. The electrodes were powered in differential mode, and the voltage was increased in small steps and the breakdown events were counted using an oscilloscope for every voltage applied, for durations between 1 and 110 hours, and the breakdown rate (BDR) per hour was calculated.

5.4.2 Test Setup

The setup for HV DC breakdown measurements is shown in Fig. 5.13. The HV power supplies, with equal but opposite polarity DC voltage, were connected to the input feedthroughs by using the low-loss HTC-50-7-2 coaxial cables with RG213-521 plugs, whereas the output feedthroughs were connected to P6015 HV probes, as shown schematically in Fig. 5.14. The HV probes used are rated at 20 kV DC, and were connected to the oscilloscope in order to see directly the voltage drop due to a sparking event.

5.4.3 Test Results

The oscilloscope was set up to trigger when the voltage dropped significantly on either electrode (Fig. 5.15), and the number of triggers, or acquisitions, were considered to be the number of breakdowns. The breakdown events started at ± 7.0 kV. From this value, the voltage was increased in steps of up to 0.25 kV. The increase in the voltage in small steps is to allow conditioning: a high BDR may appear immediately

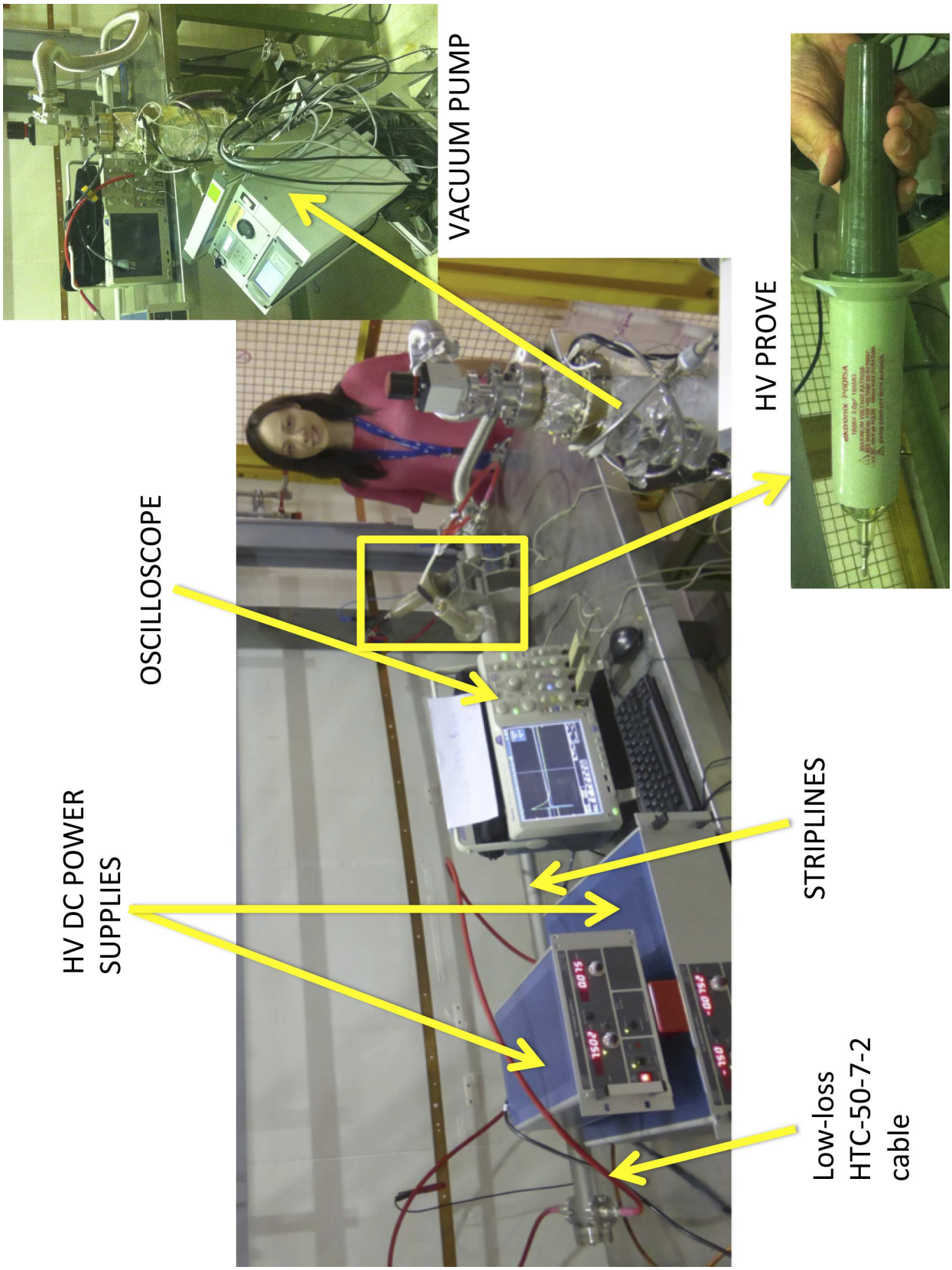

Figure 5.13: HV setup for breakdown measurements.

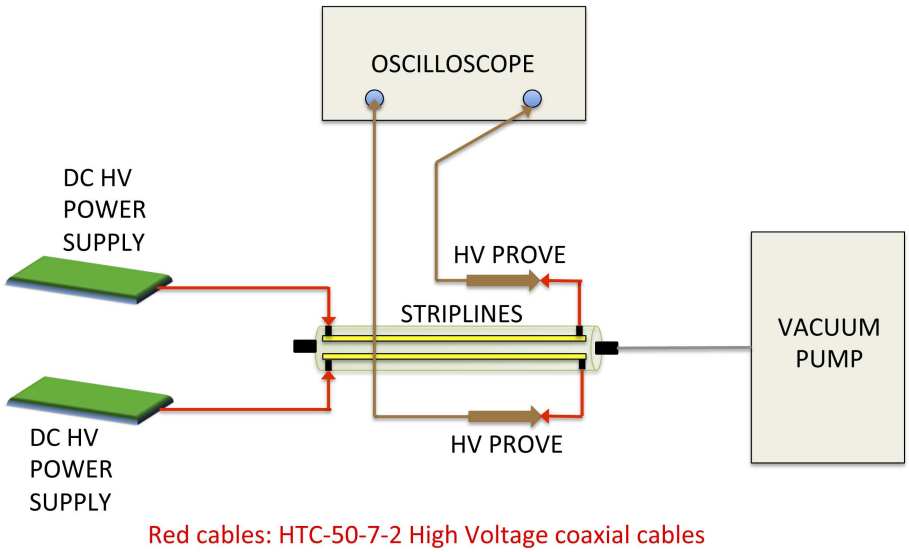

Figure 5.14: Block diagram of the test bench for HV DC breakdown rate measurement.

following an increase in the voltage, but it often reduces after several hours powering the electrodes at the same voltage.

Figure 5.16 shows the BDR per hour measured by the oscilloscope as a function of DC voltage of the electrodes. Occasionally, the voltage was reduced or a test was repeated at the same voltage, to determine whether conditioning occurred: the order of tests is shown in Fig. 5.16 by the numbers next to the rectangles. The striplines did not exhibit a BDR above 1.5 until 9.25 kV, where a maximum BDR per hour of 2.5 was found. It could be dangerous in the regions where the Macor ring is placed if the surface of the Macor is contaminated by metal from a spark. The maximum voltage achieved in the tests was ± 10.8 kV, because one of the power supplies failed. Nevertheless, a higher level of vacuum and pulsed HV tests are needed, since a significant difference in the BDR could be expected. Further DC tests and tests with the inductive adder are planned in the future. The tests, at each applied voltage, will be for a minimum duration of 8 hours in order to obtain a reasonable statistics.

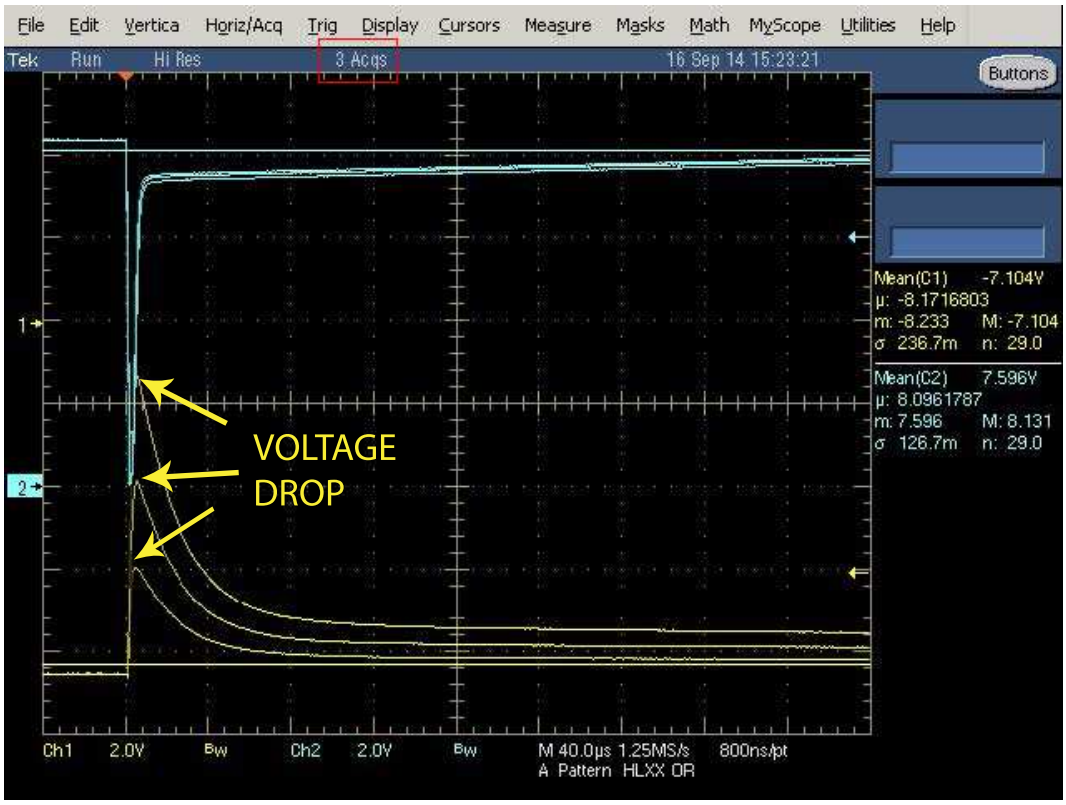

Figure 5.15: Oscilloscope set up for breakdown measurement.

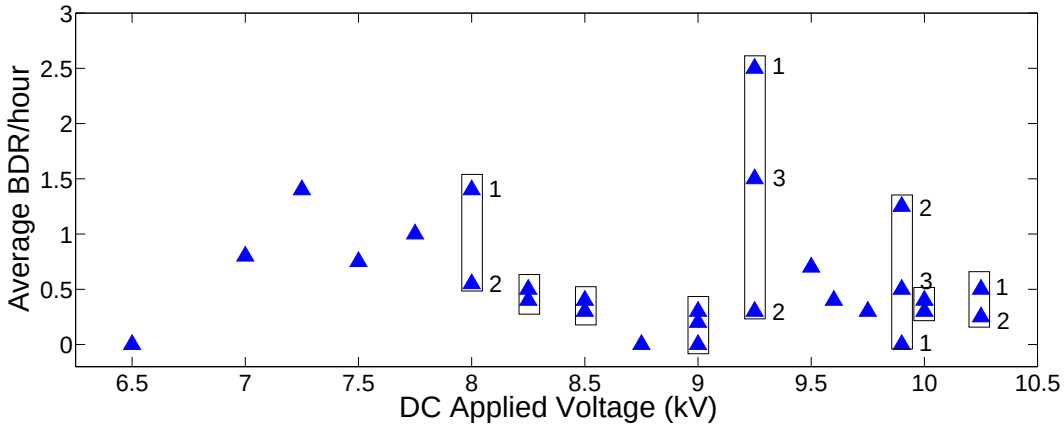

Figure 5.16: Breakdown rate for HV tests with a DC setup.

Chapter 6

Future Studies for a Next Generation Prototype of the Striplines

6.1 Introduction

A first prototype of the extraction kicker for the CLIC DRs striplines has been designed, constructed and measured in laboratory, although the methodology used by the author for the design of this kicker can be extended to the development of stripline kickers for any other low emittance rings. One important goal achieved with this first prototype has been the benchmarking of the analytical approximations and the simulations with measurements. However, some issues need to be further studied for a better performance of the striplines: 1) the characteristic impedance in the odd mode is not 50 Ω, which introduces an impedance mismatch that increase reflections and, therefore, the beam coupling impedance; 2) the high peaks appearing in the reflection parameter due to the Macor rings (Fig. 4.4) seems to respond to a constructive interference that could be avoided by changing the distance between Macor rings; 3) recently, the possibility of reducing the striplines aperture area where the field inhomogeneity must be ± 0.01%, from 1 mm radius to 0.5 mm, has been studied [76], which could help to reduce the coverage angle of the striplines and, therefore, reduce the beam coupling impedance, 4) electrode tapering, as is used in the injection kicker for DAPHNE [36], could be studied, although in our case there is not much space left between the electrode and the beam pipe wall, and 5) developments in analytical and numerical methods are required to study the beam coupling impedance. These options will be described in detail in the following sections.

Furthermore, new studies for the injection kicker for CLIC DRs, as well as the injection and extraction kickers at the PDRs could be studied in the future. Kickers for the PDRs and DRs injection do not need the high field homogeneity required for the extraction kicker from CLIC DRs (Table 2.3), and also the aperture could be larger, due to a larger beam emittance. These two specifications will help to design stripline kickers with lower beam coupling impedance.

6.2 New Ideas for Matching Characteristic Impedances

For the optimized half-moon electrode shape (Fig. 3.20, right), the odd mode characteristic impedance is 40.9 Ω. Since the inductive adder will be connected to the striplines with transmission lines of 50 Ω impedance, and each stripline will be terminated with Z_L = 50 Ω, there is an impedance mismatch for the odd mode at both the input and output of the striplines. Impedance mismatches increase the reflection parameter and the settling time (Fig. 3.29). Therefore, a new idea has been proposed to match the characteristic impedance for both the odd and even modes of excitation of the striplines.

The proposal for avoiding this impedance mismatch is to connect a matching resistor Z_m between the electrodes, on the load side of the striplines, as shown in Fig. 6.1. The matching resistor allows for a tuning of the odd mode characteristic impedance while the even mode characteristic impedance remains unchanged.

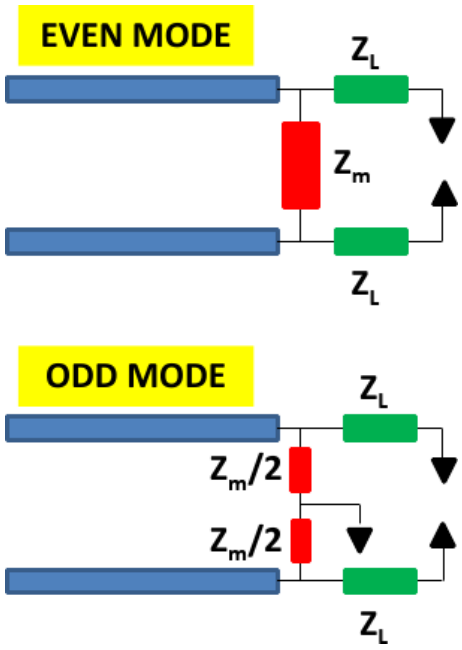

Figure 6.1: Schematic of the striplines with a resistor Z_m between the two electrodes, for matching the characteristic impedance of both even (top) and odd (bottom) modes.

When the kicker is not pulsed the voltages induced on the electrodes are only due to the beam (even mode, Fig. 6.1, top) and, therefore, the matching resistor does not affect the even mode signals. This is important because the even mode characteristic impedance is already matched to 50 Ω.

When the kicker is pulsed, the striplines are driven with opposite polarity voltages (odd mode, Fig. 6.1, bottom) and thus current flows into the matching resistor, which is seen by each pulse as a resistance of $Z_m/2$. The odd mode termination impedance is equal to:

$$(Z_L)_{odd} = \frac{(Z_L)_{even} Z_m}{2(Z_L)_{even} + Z_m}$$

This formula shows that for a terminating odd mode impedance $(Z_L)_{odd} = 40.9\ \Omega$ and a terminating even mode impedance $(Z_L)_{even} = Z_L = 50\ \Omega$ a matching resistor of $Z_m = 450\ \Omega$ is required. With this matching resistor, the terminations in the odd mode would have the same characteristic impedance as the striplines, and therefore, lower reflections should be expected.

The pulse settling time is also affected by the odd mode characteristic impedance (Fig. 3.29). Table 6.1 shows the calculated settling time with PSpice [64], to the ±0.02% level, as a function of pulse rise time and the value of the terminating resistor in the odd mode $(Z_L)_{odd}$. For the settling time simulations a single-way delay of 7 ns has been modelled for the striplines, and a total delay of 13 ns for the complete system, including the inductive adder and the coaxial cables has been also defined. For a pulse rise time of 100 ns, when the electrodes are terminated in $(Z_L)_{odd} = 50\ \Omega$ the settling time is 78 ns; this is reduced to 66 ns by including a matching resistor to decrease the odd mode termination impedance to $(Z_L)_{odd} = 40.9\ \Omega$.

	without matching resistor: $(Z_L)_{odd} = 50\ \Omega$	with matching resistor: $(Z_L)_{odd} = 40.9\ \Omega$
Pulse rise time	**Settling time**	
50 ns	109 ns	73 ns
100 ns	78 ns	66 ns
150 ns	77 ns	58 ns

Table 6.1: Settling time as a function of the pulse rise time and the terminating characteristic impedance in the odd mode $(Z_L)_{odd}$, for a stripline odd mode impedance of 40.9 Ω, when the electrodes are terminated at 50 Ω (without the matching resistor) and terminated with 40.9 Ω (with the matching resistor).

In the case of the striplines for CLIC DRs, by using the matching resistor method the settling time would be reduced from 78 ns to 66 ns. However, the presence of the matching resistor will increase the pulse current, which must be supplied by the inductive adder by approximately 20 % of the nominal current. Furthermore, the frequency range of interest, from the inductive adder point of view, goes up to 10 MHz. At this frequency, the S_{11} parameter is good enough and a matching resistor could not be really required. Nevertheless, the matching resistor could be an idea to take into account for faster striplines with a pulse rise time of the order of a few ns, where an impedance mismatching in the odd mode may significantly influence the pulse transmission through the striplines.

6.3 Electrode supports position optimization

One of the impedance mismatching sources of the striplines is the periodic discontinuities introduced by the ceramic electrode supports (Macor rings). Macor rings are uniformly spaced along the beam pipe (Fig. 4.1) and there is a significant periodic pattern caused by this uniform spacing, as shown in Fig. 4.4. The high resonances introduced by this periodic pattern could be reduced when the position of the Macor rings is changed. Therefore, a study of the effect of the spacings of the Macor rings on the S_{11} parameter could be done.

6.4 New Field Inhomogeneity Specification

The stability requirements of the DR extraction kicker and septa are determined by the maximum allowable trajectory jitter in the Ring to Main Linac (RTML) and specially the jitter at the betatron collimation region. Tracking simulations concluded that the maximum tolerable jitter after the DR extraction system is $\sigma_{jitter} \approx 0.1\,\sigma_x$, where σ_x is the horizontal beam size at extraction, although this can be relaxed to $\sigma_{jitter} \approx 0.4\,\sigma_x$ by installing feed forward (FF) systems in the RTML [76]. As part of the study, into the RTML-FF systems, the stability requirements for the extraction kicker and septa were investigated, and results shown that it is possible to reduce the good field region, where the field inhomogeneity must be below ± 0.01%, from 1 mm radius to 0.5 mm radius.

Reducing the good field region makes possible the lightening of the electrodes height, and hence, the coverage angle. This in turn will help to significantly reduce both the longitudinal and transverse beam coupling impedance (Eq. (3.34) and (3.41), respectively). Therefore, a new geometry with lower beam coupling impedance could be studied for a new prototype, taking into account this more relaxed requirement for field homogeneity.

6.5 Beam Coupling Impedance Studies

Further beam coupling impedance studies, at low and high frequencies, are required. At low frequencies, the longitudinal beam coupling impedance has been fully characterized, with a good agreement between the analytical expression, CST simulations and measurements in laboratory. This is not the case for the transverse beam coupling impedance: the equation for the transverse dipolar impedance present some differences with the CST simulation results, and the measurements are significantly different, specially in the vertical plane. Furthermore, no analytical expression for the quadrupolar component has been found in the literature: to calculate the total transverse impedance of the striplines, the quadrupolar component has to be determined. Therefore, further investigation of the transverse beam coupling impedance

is required, which will consist of: (1) analytical studies, (2) simulations with a new code, e.g. Gdfidl, in order to compare the results with the CST results, and (3) new laboratory measurements of both the dipolar and the total transverse (horizontal and vertical) beam coupling impedance.

On the other hand, the design of a new generation of accelerators, such as high-energy colliders, synchrotron light sources, storage rings, etc., is often based on the use of very short bunches. In this case, beam stability and energy loss are largely determined by the behavior of the impedance at high-frequencies. For that reason, analytical approximations as well as numerical methods to calculate the beam coupling impedance at high frequencies should be developed in the future [39].

At high frequencies, and from the analytical point of view, new developments are necessary in order to calculate the beam coupling impedance of striplines BPMs and kickers. Two aspects must be considered [57] when passing from the low-frequeny approximation for the beam coupling impedance to higher frequencies. The first aspect takes into account that, at low frequencies, an image of a point charge in the wall of the beam pipe is assumed to be also a point charge (charge of zero duration). However, this is only true if the particle is travelling at exactly the speed of light and the electromagnetic fields created by this particle are TEM waves. In reality, due to the finite velocity of the particles, the electromagnetic fields are not purely TEM and have a longitudinal spread, which reduces the wall current with more impact at high frequencies. The second aspect refers to the period of the image current, which at high frequencies can be a significant fraction of the transit time of the particle along the gap between the beam pipe and the electrode edge. When it occurs, the wall current amplitude is also reduced. In Eq. (3.34) and (3.41) the beam current and the wall currents are considered to be constant; this approximation can not be used at high frequencies, where the wall currents change with the frequency.

The main interest of simulating the striplines in time domain lies on the fact that the output of the simulation in terms of wake function may be directly used in particle tracking simulations to study the impact of these elements on the beam stability. In particular, wake functions in form of tables can be provided as an input into the HEADTAIL code [82], which is typically used for studying collective effects in beam dynamics [83]. Since the wake functions are needed, the source bunch used in CST simulations should be short enough to be consistent with the length of the bunch slices simulated in HEADTAIL. In the CLIC DRs case, the bunch length is ≈ 2 mm. This obviously limits the analysis to a maximum frequency of the order hundreds of GHz. Nowadays, the simulations of beam coupling impedance with CST at high frequencies are not valid, and this is true not only for the stripline kickers but whatever other accelerator device whose impedance needs to be characterized numerically [39].

6.6 Electrode Tapering Studies

Tapered electrodes have demonstrated in the past to be suitable for improving the power transmission and reduce the beam coupling impedance at high frequencies and therefore, the beam induced electrode heating [36]. For longitudinal and transverse calculations, Eq. (3.34) and (3.41) can still be used for tapered electrodes at low frequencies, multiplying by an additional term (last term in Eq. (6.1)) which takes into account a linear taper in the coverage angle [84]:

$$Z_{\parallel}(\omega) = \frac{Z_{even}}{2} g_{\parallel}^2 \left[sin^2\left(\frac{\omega L}{c}\right) + j sin\left(\frac{\omega L}{c}\right) cos\left(\frac{\omega L}{c}\right) \right] \left[\frac{\sin^2\left(\frac{\omega l}{c}\right)}{\left(\frac{\omega l}{c}\right)^2} \right] \tag{6.1}$$

$$Z_{\perp}(\omega) = Z_{odd} \left(\frac{g_{\perp}}{b}\right)^2 \frac{c}{\omega} \left[sin^2\left(\frac{\omega L}{c}\right) + j sin\left(\frac{\omega L}{c}\right) cos\left(\frac{\omega L}{c}\right) \right] \left[\frac{\sin^2\left(\frac{\omega l}{c}\right)}{\left(\frac{\omega l}{c}\right)^2} \right] \tag{6.2}$$

where Z_{even} is the even mode characteristic impedance, $g_{\parallel}$ is the longitudinal geometric factor, Z_{odd} is the odd mode characteristic impedance, $g_{\perp}$ is the transverse geometric factor, c is the speed of light, L is the electrodes length and l is the taper length. Results for longitudinal beam coupling impedance for both untapered and tapered striplines are shown in Fig. 6.2. For these calculations, tapers are considered to have a length of 10% and 20% of the electrodes length.

When tapering the electrodes, the longitudinal beam coupling impedance starts to reduce from $\approx$ 150 MHz, and becomes zero from $\approx$ 800 MHz when the tapers length is 10% of the electrode length. When the tapers length is 20% of the electrodes length, the longitudinal beam coupling impedance is zero from $\approx$ 400 MHz. This is the same for the real component and for the imaginary component of the longitudinal beam coupling impedance.

In the transverse plane, only the dipolar horizontal beam coupling impedance can be analytically calculated, as it was explained in Chapter 3. Results are shown in Fig. 6.3, for the real part and the imaginary part, respectively.

When considering the horizontal impedance, no significant difference occurs at low frequencies between tapered and untapered electrodes. However, as in the longitudinal case, from $\approx$ 800 MHz, the horizontal dipolar impedance goes to zero when the tapers have a length of 10% of the electrode length, whereas this frequency range reduces a factor 2 (from $\approx$ 400 MHz), when the taper length is multiplied by a factor 2 (20% of the electrode length).

For CLIC DRs, the electrodes of the extraction stripline kicker could be tapered if measurements with beam indicate that electrode heating is higher than expected (Section 3.5.2) and it is not possible to lower the beam coupling impedance at high frequencies. In such a case, numerical simulations would be required to confirm the

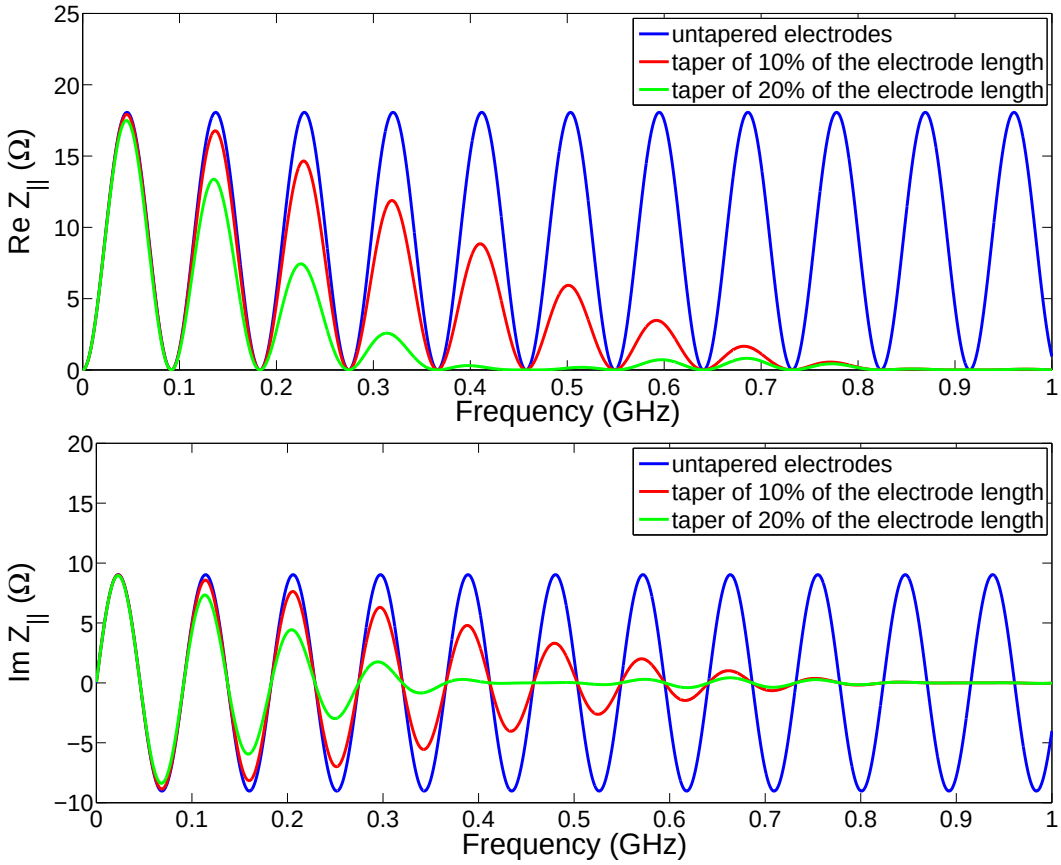

Figure 6.2: Analytic calculation of the real (top) and imaginary (bottom) component of the longitudinal beam coupling impedance for untapered electrodes (blue) and electrodes with a taper length of 10% (red) and 20% (green) of the total length.

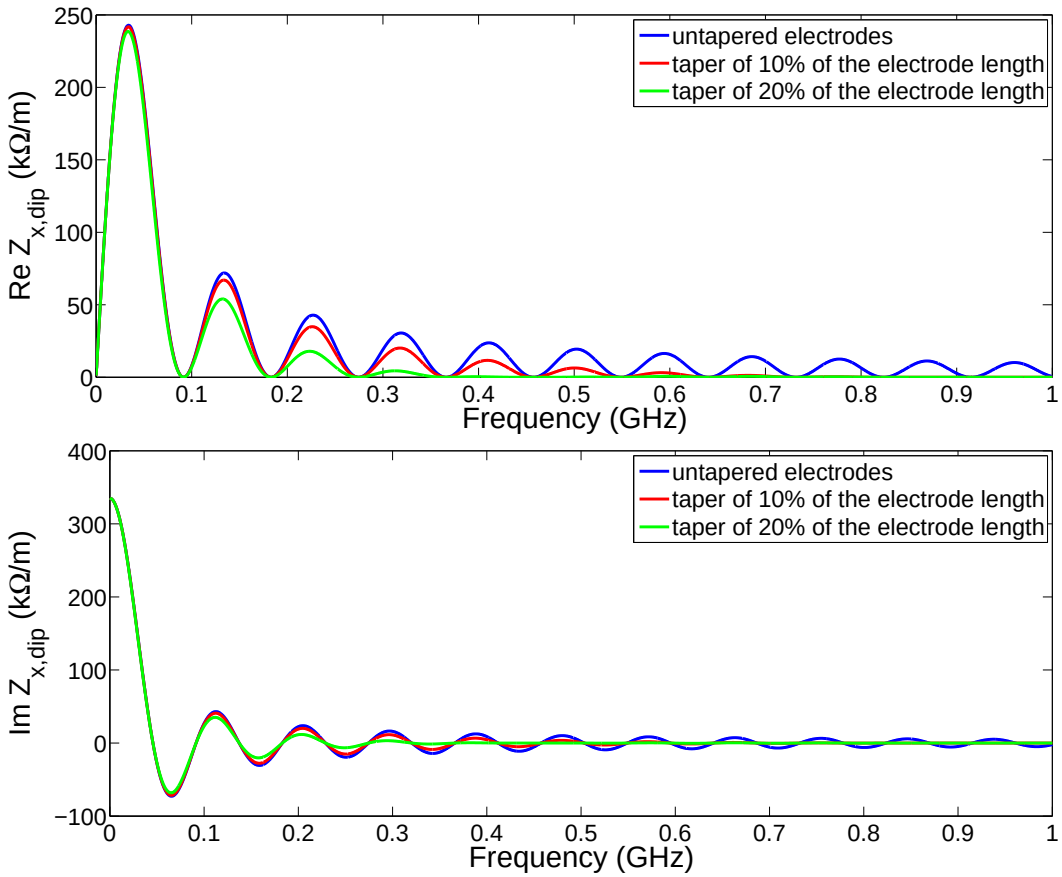

Figure 6.3: Real (top) and imaginary (bottom) part of the horizontal beam coupling impedance for untapered (blue) and electrodes with a taper length of 10% (red) and 20% (green) of the total length.

behaviour from the analytical equations. However, tapering the electrodes could not be suitable in our case, due to the fact that the distance between the electrodes and the beam pipe wall is only 6 mm, and there is no much space left for tapers. Furthermore, it is very difficult to manufacture tapered electrodes which are 1.6 m long.

Chapter 7

Conclusions

Damping Rings (DRs) for Future Linear Colliders (FLCs) have a significant role for achieving high luminosity at the Interaction Point (IP). To inject and extract the beam from the CLIC DRs without impact on the beam emittance, very stable injection and extraction systems are required: the kicker specifications for field uniformity and beam coupling impedance are unprecedented. This Thesis consists of the development of the extraction kicker for CLIC DRs, but the proposed methodology can be extended to stripline kickers for any other low emittance ring. The work done for the realization of this Thesis has contributed to the field of injection and extraction systems for circular accelerators, not only for DRs for FLCs, but also for new generation accelerator rings.

The Thesis project started from the specifications of the extraction kicker for CLIC DRs. From these requirements, the design study and the methodology proposed was done by the author. Furthermore, the author participated in the manufacturing of the striplines, and carried out the laboratory tests to characterize the striplines performance.

The design study of the stripline kicker for CLIC DRs has allowed to identify the two operation modes of a stripline kicker: odd and even modes, and to analyze the characteristic impedance of each mode by using the capacitances between the two electrodes and between one electrode and the beam pipe wall. It has allowed to evaluate the dependence of the striplines geometry with the characteristic impedance of these two modes of operation. Furthermore, the field homogeneity has been related with the geometry of the striplines. When starting the striplines design, the two most common electrodes shapes used in stripline kickers, flat and curved electrodes, were studied and compared. The results showed that only with flat electrodes was it possible to achieve the field homogeneity required, although the impedance mismatching was not good enough. Therefore, a new electrode shape has been proposed by the author, the half-moon electrode, which has better field homogeneity than curved electrodes and better impedance matching than flat electrodes. 2D calculations, including the calculation of the RF breakdown limit, were followed by 3D studies to calculate the power reflection through the striplines and the longitudinal and transverse beam coupling impedance

at low frequencies. This work allowed to understand the two operation modes of a stripline kicker and how they are related with the kicker performance: the power transmission and the transverse beam coupling impedance of the striplines must be linked with the impedance mismatch seen by the pulse in the odd mode, whereas the longitudinal beam coupling impedance is related with the impedance mismatch seen by the beam when entering the striplines in the even mode. For the beam coupling impedance study, the most common analytical equations are defined for striplines with an aperture equal to the beam pipe diameter: in this Thesis, more general expressions have been used, in order to define the longitudinal and transverse beam coupling impedance for any striplines geometry.

Besides the striplines geometry, the striplines components were studied and optimized. The electrode supports that are commonly used were not useful in the case of the striplines for CLIC, due to the small separation between the electrodes and the beam striplines. Therefore, a new idea was proposed by the manufacturer: a set of ceramic rings, made up of Macor, could keep the electrodes aligned and fixed inside the striplines beam pipe. The use of ceramic rings as electrode supports is a new idea that allows the field uniformity to be mechanically guaranteed. The optimization of the electrode supports and the commercial feedthroughs, considering the effect over the power reflection and the beam coupling impedance, was numerically done. The fabrication of the first striplines prototype was carried out by the Spanish company Trinos Vacuum Projects.

The results from the simulations during the design phase were compared with the results of the laboratory tests. The following measurements have been done: power reflection through the striplines, longitudinal and transverse beam coupling impedance and RF breakdown tests. The good agreement between data from measurements and simulations for the reflection parameter and the longitudinal beam coupling impedance, has served to give confidence in the models used in the simulations up to a frequency of 1 GHz: these models can be used in further studies of next generation prototypes. However, for higher frequencies, new analytical expressions and simulations should be developed.

The main characteristics achieved by the first stripline kicker prototype for the CLIC DRs described in this Thesis have been the following: 1) good characteristic impedance matching in the two operation modes, 2) excellent field homogeneity, 3) good power transmission through the striplines, 4) low risk of RF breakdowns, and 5) low risk of electrode heating. At low frequencies, the longitudinal beam coupling impedance achieved is very low, but still slightly above the limits. The transverse beam coupling impedance is very low in the vertical plane, but this is not the case in the horizontal plane. In this sense, the relaxation of the requirement for field homogeneity will help to make a new design with even lower beam coupling impedance.

Overall, a key contribution of this Thesis to the field of injection and extraction systems is the execution of a systematic study of the striplines performance, which has allowed to quickly relate the main specifications of a stripline kicker system for an accelerator with the striplines design. This could help in the design of striplines for

future accelerators with very tight tolerances, especially for low emittance rings.

This prototype is a first step in the future injection and extraction devices in DRs for FLCs. In this sense, measurements with beam in ALBA will be made, in the framework of CLIC collaboration, to fully characterize the striplines performance, by studying the longitudinal and transverse beam coupling impedance with beam.

Bibliography

[1] HL-LHC: High Luminosity Large Hadron Collider, www.hilumilhc.web.cern.ch.

[2] The International Linear Collider: Technical Design Report (TDR), www.linearcollider.org/ILC/Publications/Technical-Design-Report, 2013.

[3] The European Strategy for Particle Physics, CERN-Council-S/106, 2013.

[4] N. Walker, “Physics and Technology of Linear Collider Facilities: Introduction and Overview”, Notes for the US Particle Accelerator School (USPAS), 2003.

[5] H. Wiedemann, Particle Accelerator Physics, Springer Verlag (1993).

[6] The International Linear Collider: Reference Design Report (RDR), www.linearcollider.org/ILC/Publications/Reference-Design-Report, 2007.

[7] N. Walker, J. Carwardine, “Cryomodule String Test: TTF/FLASH 9 mA Experiment”, GDE AAP Review, 2009.

[8] LCLS webpage: http://lcls.slac.stanford.edu.

[9] ATF Accelerator Test Facility Study Report, JFY1996-1999, http://atfweb.kek.jp/atf/Reports/ATF99new.pdf.

[10] R. Dowd, M. Boland, G. LeBlanc, Y-R.E. Tan, “Achievement of Ultralow Emittance Coupling in the Australian Synchrotron Storage Ring”, Physical Review Special Topics -Accelerators and Beams 14, 012804, 2011.

[11] Paul Scherrer Institute webpage: http://www.psi.ch/sls.

[12] Brookhaven National Laboratory webpage: http://www.bnl.gov/world.

[13] ATF2 Proposal, Volumes 1&2, ATF2 Collaboration, 2005-2006, http://lcdev.kek.jp/ATF2/proposal.

[14] CesrTA webpage: https://wiki.classe.cornell.edu/ILC/CesrTA/WebHome.

[15] NLCTA website: https://portal.slac.stanford.edu/sites/ard-public/tfd/facilities/nlcta/Pages/Default.aspx

[16] S. Matsumoto, M. Akemoto, S. Fukuda, T. Higo, N. Kudoh, H. Matsushita, H. Nakajima, T. Shidara, K. Yokoyama, M. Yoshida, "Nextef: 100 MW X-Band Test Facility in KEK", Proceedings of the 11st European Particle Accelerator Conference, EPAC 2008.

[17] N. Catalán-Lasheras, A. Degiovanni, S. Doebert, W. Farabolini, J. Kovermann, G. McMonagle, S. Rey, I. Syratchev, L. Timeo, W. Wuensch, B. Woolley, J. Tagg, "Experience Operating an X-band High-Power Test Stand at CERN", Proceedings of the 5th International Particle Accelerator Conference, IPAC 2014.

[18] F. Peauger, A. Hamdi, S. Curt, S. Doebert, G. McMonagle, G. Rossat, K.M. Schirm, I. Syratchev, L. Timeo, S. Kuzikhov, A.A. Vikharev, A. Haase, D. Sprehn, A. Jensen, "A 12 GHz RF Power Source for the CLIC Study", SLAC-PUB-15144.

[19] CLIC Conceptual Design Report (CDR), Volume 1, www.project-clic-cdr.web.cern.ch/project-clic-cdr/CDR-Volume1.pdf, 2012.

[20] A. Wolski, "Damping Ring Design and Physics Issues", Lecture for the 4th International Accelerator School for Linear Colliders, 2009.

[21] G. Rumolo et al., "Collective Effects in the CLIC Damping Rings". Proceedings of the 11th European Particle Accelerator Conference, EPAC 2008.

[22] A. Wolski, J. Gao and S. Guiducci, "Configuration Studies and Recommendations for the ILC Damping Rings", ILC-NOTE-2009-051, 2006.

[23] E. Koukovini-Platia, G. Rumolo, "Review of the Transverse Impedance Budget for the CLIC Damping Rings", Proceedings of the 5th International Particle Accelerator Conference, IPAC 2014.

[24] F. Antoniou, M. Martini, Y. Papaphilippou, A. Vivoli, "Parameter scan for the CLIC Damping Rings under the influence of intrabeam scattering", Proceedings of the 1st International Particle Accelerator Conference, IPAC 2010.

[25] L. Mether, G. Rumolo, G. Iadarola, H. Bartosik, "Two-beam Instabilities in Low Emittance Rings", Low Emittance Rings Workshop, LOWεRING 2014.

[26] M.J. Barnes, J. Borburgh, B. Goddard and M. Hourican, "Injection and Extraction Magnets: Septa". Proceedings of CERN Accelerator School (CAS): Specialized Course on Magnets, 2009.

[27] M.J. Barnes, L. Ducimetiére, F. Towler, V. Senaj and L. Sermeus, "Injection and Extraction Magnets: Kicker Magnets". Proceedings of CERN Accelerator School (CAS): Specialized Course on Magnets, 2009.

[28] M.G. Minty, F. Zimmermann, “Measurement and Control of Charged Particle Beams”, Springer-Verlag, 2003.

[29] T. Naito, S. Araki, H. Hayano, K. Kubo, S. Kuroda, N. Terunuma, T. Okugi, J. Urakawa, “Multibunch beam extraction using the strip-line kicker at the KEK Accelerator Test Facility”, Physical Review Special Topics -Accelerators and Beams 14, 051002, 2011.

[30] B. Goddard, “Injection and Extraction”, Lecture of CERN Accelerator School (CAS), 2010.

[31] I. Rodríguez, “Calculation Methodology and Fabrication Procedures for Particle Accelerator Strip-line Kickers: Application to the CTF3 Combiner Ring Extraction Kicker and TL2 Tail Clippers”, PhD thesis, Universidad Politécnica de Madrid, 2009.

[32] KEK website: www.kek.jp.

[33] T. Adachi and T. Kawakubo,“Electrostatic Injection Kicker for the KEK Digital Accelerator”, Physical Review Special Topics - Accelerators and Beams, 16, 053501, 2013.

[34] T. Naito, H. Hayano, M. Kuriki, N. Terunuma, J. Urakawa, “Development of a 3 ns rise and fall time strip-line kicker for the International Linear Collider”, Nuclear Instruments and Methods in Physics Research A 571 (2007), pp 599-607.

[35] LNF DAΦNE website: http://www.lnf.infn.it/acceleratori.

[36] D. Alesini, S. Guiducci, F. Marcellini, P. Raimondi, “Design, test, and operation of new tapered stripline injection kickers for the e^+e^- collider DAΦNE”, Physical Review Special Topics - Accelerators and Beams, 13, 111002 (2010).

[37] F. Marcellini, D. Alesini, S. Guiducci, P. Raimondi, “Tests and operational experience with the DAΦNE stripline injection kicker, Proccedings of the Particle Accelerator Conference, PAC 2009.

[38] F. Marcellini et al., Coupling impedance of DAΦNE upgraded vacuum chamber, Proceedings of the European Particle Accelerator Conference, EPAC 2008.

[39] G. Rumolo, CERN, private communication.

[40] IFIC website: http://ific.uv.es (Accelerators Group: http://gap.ific.uv.es).

[41] CIEMAT website: http://www.ciemat.es (Accelerators Group:)

[42] CDTI website: https://www.cdti.es.

[43] Trinos Vacuum Projects S.L. website: http://www.vacuum-projects.net.

[44] Collaboration for Design and Engineering consultancy on Stripline Kicker. CDTI project between IFIC-CSIC and Trinos Vacuum Projects (IDC-20101074). Duration of the project: 09/2010-12/2012.

[45] D. M. Pozar. Microwave Engineering, 3rd Edition, 2004.

[46] J. Holma, M.J. Barnes, C. Belver-Aguilar, "Measurements on Prototype Inductive Adders with Ultra-flat-top Output Pulses for CLIC DR Kickers", Proceedings of the 5th International Particle Accelerator Conference, IPAC 2014.

[47] J. Holma, "Present Status of Inductive Adder Development for the CLIC DR Kicker Systems", CLIC Workhsop 2014, https://indico.cern.ch/event/275412/session/17/contribution/132/material/slides/1.pdf.

[48] W.R. Blood, MECL System Design Handbook, 4th edition, 2000.

[49] W.D. Kilpatrick, "Criterion for Vacuum Sparking Designed to Include Both RF and DC, The Review of Scientific Instruments, VCRL-2321, 1957.

[50] T. P. Wangler, "Principles of RF Linear Accelerators", John Wiley & Sons, Inc., 2008.

[51] S. Verdú Andrés, "High-Gradient Accelerating Structure Studies and their Application in Hadrontherapy", PhD thesis, Universidad de Valencia, 2012.

[52] M.J. Barnes, P. Adraktas, V. Baglin, G. Bregliozzi, F. Caspers, S. Calatroni, H. Day, L. Ducimetiére, M. Garlasch, V. Gomes Namora, J. M. Jimnez, N. Magnin, V. Mertens, E. Mtral, B. Salvant, M. Taborelli, J. Uythoven, W. Weterings, "Upgrade of the LHC Injection Kicker Magnets", Proceedings of the 4th International Particle Accelerator Conference, IPAC 2013.

[53] F. Caspers, RF engineering basic concepts: S-parameters, CAS Lectures, Denmark 2010.

[54] C. Zannini, "Electromagnetic Simulation of CERN Accelerator Components and Experimental Applications", PhD thesis (2013).

[55] B.W. Zotter, S.A. Kheifets, "Impedances and Wakes in High-Energy Particle Accelerators", World Scientific Publishing, 2000.

[56] A. Blednykh, W. Cheng, S. Krinsky, "Stripline Beam Impedance", Proceedings of Particle Accelerator Conference, PAC 2013, Pasadena, USA.

[57] K.Y. Ng, Impedances of Stripline Beam-Position Monitors (1987).

[58] D. A. Goldberg and G. R. Lambertson, “Dynamic Devices: A Primer on Pick-ups and Kickers”, LBNL Paper LBL-31664, 1991.

[59] R.E. Shafer, “Beam Position Monitoring”, American Institute of Physics (1992).

[60] A. W. Chao, M. Tigner, Handbook of Accelerator Physics and Engineering, 3rd Edition (2006).

[61] Ansys website: www.ansys.com.

[62] A. Krasnykh, “Analysis of Approaches for a Design of APS-U Fast Injection System”, Mini Kicker Workshop in ANL, 2013.

[63] CST Studio website: www.cst.com.

[64] Candence website: http://www.cadencepcb.com.

[65] M.J. Barnes, CERN, private communication.

[66] Quickfield website: www.quickfield.com

[67] B.R. Poole, G.J. Caporaso, Y.J. Chen, L.F. Wang, “Analysis and Modeling of a Stripline Beam Kicker and Septum, XIX International Linac Conference, Chicago, 1998.

[68] L. Palumbo, V.G. Vaccaro, M. Zobov, “Wake Fields and Impedance”, LNF-94/041 (1994).

[69] C. Belver-Aguilar, A. Faus-Golfe, F. Toral, M.J. Barnes, “Stripline Design for the Extraction Kicker of Compact Linear Collider Damping Rings”, Physical Review Special Topics - Accelerators and Beams, 17, 071003 (2014).

[70] S. Casalbuoni, M. Migliorati, A. Mostacci, L. Palumbo, B. Spataro, “Beam heat load due to geometrical and resistive wall impedance in COLDDIAG”, IOP publishing for SISSA MEDIALAB, 2012.

[71] GdFidl website: http://www.gdfidl.de.

[72] ALBA website: https://www.cells.es

[73] T. Gunzel, “Longitudinal impedance characterisation of the CLIC-stripline in view of its test in the ALBA storage ring”, Topical Workshop on Instabilities, Impedances and Collective Effects (TWIICE), 2014.

[74] http://www.corning.com

[75] Kyocera catalog: http://formulare.kyocera.de/download/Kyocera-Ultra-High-Vacuum-Products.pdf

[76] R. Apsimon, B. Balhan, M.J. Barnes, J. Borburgh, B. Goddard, Y. Papaphilippou, J. Uythoven, “Optics and protection of the injection and extraction regions of the CLIC damping rings”, Proceedings of the 4th International Particle Accelerator Conference, IPAC 2013.

[77] Diconex website: www.diconex.fr

[78] J. Holma and M.J. Barnes, “The Prototype Inductive Adder with Droop Compensation for the CLIC Kicker Systems”, accepted to be published in Trans. Plasma Sci (2014).

[79] T. Kroyer, F. Caspers, E. Gaxiola, “Longitudinal and Transverse Wire Measurements for the Evaluation of Impedance Reduction Measures on the MKE Extraction Kickers”, AB-Note-2007-028.

[80] H. Day, M.J. Barnes, F. Caspers, E. Metral and B. Salvant, “Beam Coupling Impedance of the New Beam Screen of the LHC Injection Kicker Magnets”, IPAC’14, Dresden.

[81] C. Belver-Aguilar, A. Faus-Golfe, F. Toral, M. J. Barnes, H. A. Day, “Measurements and Laboratory Tests on a Prototype Stripline Kicker for the CLIC Damping Ring”, Proceedings of IPAC 2014.

[82] HEADTAIL code.

[83] E. Koukovini, CERN, private communication.

[84] S. Smith, SLAC, private communication.

Aknowledgements

I would like to express my gratitude to IFIC for letting me participate in the research of future linear colliders. Many thanks to my supervisors, Dr. Ángeles Faus-Golfe, for give me the opportunity to start up this research in the amazing field of accelerator physics, and for her constant guide and priceless support, and Dr. Fernando Toral, for his good advices and patience, always helping me in spite of the distance.

Special thanks to Dr. Mike Barnes for his guide during my stays at CERN and his constant support. Also I am very grateful to Dr. Hugo Day, for his help in all the laboratory tests of the striplines.

I must acknowledge the participation of our industry partner, Trinos Vacuum Projects for their great collaboration during the design phase, and for manufacturing the striplines.

Thanks to all my IFIC colleagues, in particular to the ones that compose or composed the Group of Accelerator Physics: Alfonso Benot, César Blanch, Dr. Javier Alabau, Dr. Javier Resta, Jorge Giner, Dr. Juanjo García and Núria Fuster. Many thanks Núria for all our discussions about everything, both professional and personal.

I am very grateful to the Accelerators Technology group at CIEMAT, for helping me at the beginning of this adventure. Many thanks also to the Accelerator Beam Transfer group at CERN, for the technical support during the laboratory tests, and for so many funny discussions in the coffee breaks.

Un agradecimiento muy especial a mi família, tanto la de sangre como la política, y especialmente a mis padres, por estar siempre ahí y darme todo su apoyo. No hay palabras para expresar mi agradecimiento a Jordi por su ayuda y su apoyo incondicional durante esta aventura.